CHARLES UNIVERSITY IN PRAGUE

FACULTY OF MATHEMATICS AND PHYSICS

DOCTORAL THESIS

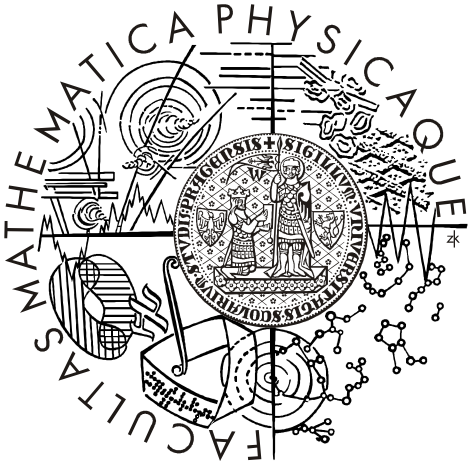

Jozef Varju

STUDY OF H_3^+ RECOMBINATION IN SELECTED QUANTUM STATES

DEPARTMENT OF SURFACE AND PLASMA SCIENCE

Supervisor: Prof. RNDr. Juraj Glosík, DrSc.

Study program: Physics
Specialization: 4f2 – Physics of Plasmas and Ionized Media

Prague 2011

„After a year's research, one realizes that it could have been done in a week.“
Sir William Henry Bragg

I would like to express my utmost gratitude to my supervisor prof. Juraj Glosík for his support, counseling and all the opportunities he presented to me during my doctoral studies.

I’d like to thank Prof. Andreas Wolf for the opportunity to stay and work at the Max Planck Institute for Nuclear Physics which allowed me to gain hands on experience with techniques and technology I would have never been able to obtain otherwise.

The people I hade a chance to work together with, whether in Heidelberg or Prague, created a cheerful work atmosphere that made the time fly by and I take a lot of wonderful memories with me from the time spent with them. I especially thank all my coworkers for all the knowledge and experience they helped me to gain. Without them this work would hardly be possible.

I have to express a great deal of gratitude to my wife for her patience and support during all those years.

I thank also the Czech State for financial support through the Ministry of Education, Youth and Sports, the research plan MSM 0021620834 financed by the Ministry of Education of the Czech Republic and was partly supported by GACR (202/07/0495, 205/09/1183, 202/09/0642, 202/08/H057) and by GAUK 124707

I declare that I carried out this doctoral thesis independently, and only with the cited sources, literature and other professional sources.

I understand that my work relates to the rights and obligations under the Act No. 121/2000 Coll., the Copyright Act, as amended, in particular the fact that the Charles University in Prague has the right to conclude a license agreement on the use of this work as a school work pursuant to Section 60 paragraph 1 of the Copyright Act.

In…..... date..... signature

Název práce: Studium rekombinace H_3^+ ve vybranych kvantových stavech
Autor: Jozef Varju
Katedra / Ústav: Katedry fyziky povrchů a plazmatu
Vedoucí doktorské práce: Prof. RNDr. Juraj Glosík, DrSc.,
Katedry fyziky povrchů a plazmatu

Abstrakt:

V tejto práci su prezentované merania effektívnej rýchlostnej konšntanty rekombinacie v H_3^+ dominovanej plazme a ovladanej rekombináciou pri 77 K a 145 K. Populácia para-H_3^+ v študovanej plazme bola menená použitím H_2 s obohatenou populaciou para stavov ako reaktantu popri normálnom H_2. Časovo rozlíšená CRDS v blízkej infračervenej oblasti bola použita na in-situ meranie vývoja hustoty dvoch najnižších rotačných stavov H_3^+. Merania pri rôzných pomeroch para ku orto H_3^+, pri inač identických podmienkach, umožnili extrapolovanie effektivnej rýchlostnej konštanty rekombinácie čistého para-H_3^+ a orto-H_3^+. S nameraných závislosti na hustote nosného plynu boli učené hodnoty rýchlostnej konštanty rekombinácie binárneho a ternárneho kanálu pre para-H_3^+ a ortho-H_3^+.

Klíčová slova: rekombinace, spektroskopie, H_3^+, para H_2

Title: Study of H_3^+ recombination in selected quantum states
Author: Jozef Varju
Department : Department of Surface and Plasma Science
Supervisor of the doctoral thesis: Prof. RNDr. Juraj Glosík, DrSc.,
Department of Surface and Plasma Science

Abstract:

In this work measurement of the effective recombination rate coefficient of H_3^+ dominated and recombination governed afterglow plasma at 77 K and 145 K are presented. Population of para-H_3^+ in the studied plasma has been varied by using para enriched H_2 as a precursor along with normal H_2. Time resolved NIR-CRDS was used to in-situ measure the number density evolution of the two lowest rotational states of H_3^+. Measurements at different para to ortho H_3^+ ratios, at otherwise identical conditions, allowed for extrapolation of the effective recombination rate coefficient of pure para-H_3^+ and ortho-H_3^+. From measured dependences on the buffer gas densities the values of the recombination rate coefficients for the binary and ternary channel are determined of para-H_3^+ and ortho-H_3^+.

Keywords: recombination, spectroscopy, H_3^+, para H_2

Contents

1 Introduction

This thesis summarizes most of the author's work from his doctoral studies at the Charles University in Prague. The main topic is the experimental study of state sensitive dissociative recombination of H_3^+.

Recombination of the simplest polyatomic ion H_3^+ has been extensively studied for over 50 years both theoretically and experimentally. Still much effort is dedicated to this ion and processes it is involved in. Until now storage ring experiments were used as the standard experimental reference for further studies but lately several problems with these experiments have been discovered, e.g. high internal temperature and questionable nuclear spin distribution of the studied ions. Therefore recently several researchers expressed a need for state selective experimental data for testing the predicted values obtained in theoretical studies. The interest is focused mainly on data at cryogenic temperatures that are relevant to astrophysical environments. The main subject of this thesis is the state sensitive study of the dissociative recombination of H_3^+ at cryogenic temperatures in He/Ar/H_2 afterglow plasma. As the main diagnostic tool a near infrared cavity ring-down absorption spectrometer was used. This work effectively extends the spectroscopic measurements of H_3^+ recombination performed in the group of prof. Glosík. Besides the significant results on state sensitive recombination also an expansion on used experimental conditions is achieved, when compared to previous work using CRDS.

1.1 Goals

The main goal of the presented work was to obtain state dependent recombination rate coefficients of the H_3^+ ion at various cryogenic temperatures. To obtain not only the effective recombination rate coefficients observed in standard afterglow experiments but more importantly to obtain the derived rate coefficients of the binary and ternary recombination channels. These can be compared to theoretical predictions and can be used in astrophysical modeling directly.

Particular goals include:

- To obtain data relevant for gaining more insight into thermodynamic equilibrium of H_3^+ states at various conditions
- Measuring dependences of the recombination rate coefficients on buffer gas density.
- Measure the above mentioned dependences for H_3^+ populations with different internal states populations.

- Build and test an apparatus for production of H_2 with an enriched population of molecules with para nuclear spin.
- Changes in the used apparatus required in order for the presented goals to be achievable, mainly on the cooling part of the apparatus.
- To obtain the values of the binary and ternary recombination rate coefficient of pure para- H_3^+ and ortho- H_3^+ at various temperatures.

1.2 Thesis overview

The thesis is divided as follows:

Chapter 2

A short introduction about the history and importance of the H_3^+ ion and into the problems found in the study of its recombination is presented. Historical overview of experimental studies shows the amount of work that was put into studying the recombination of this ion. Also a simplified description of the various recombination processes invoked to explain the observed rate coefficient is given. The quantum properties and common quantum state labeling nomenclature of H_3^+ is presented. The problematic bimolecular reaction of H_3^+ with H_2, with its peculiar state to state (spin dependent) rate coefficients and branching ratios, is shortly mentioned. Although this reaction is the corner stone for creating the needed experimental conditions the precise knowledge of it is not necessary for achieving the main goal of the presented work and therefore is presented only informatively. The main point is to show why Hydrogen with an enriched population of para symmetry states was used in the actual experiments.

Chapter 3

Absorption spectroscopy is the basic diagnostic tool used for the study presented in this thesis. Basic formals and principles of absorption spectroscopy needed for the quantitave analysis are given in this chapter. Also the basic concepts of cavity ring down spectroscopy are presented and description of the particular modification that was used in the experiment (continuous wave-Cavity Ring-Down Spectroscopy) is given.

Chapter 4

In this chapter the experimental apparatus is described. The optical part, vacuum and gas handling, plasma generation together with data acquisition and data processing is described. The description of the para enriched Hydrogen generator setup follows next. This chapter is complemented by appendix A that describes the tuning procedure of the optical setup with some practical hints and peculiarities of the used experimental setup that are not found elsewhere in literature in one place.

The experimental apparatus was upgraded and to put the changes into context the description is therefore more thorough.

Chapter 5

In this chapter the actual results obtained in the experiments are summarized. Experiments were performed at various buffer gas pressures, at a wide range of reactant concentrations and at different temperatures. The results obtained at various experimental conditions are discussed. The final state dependent recombination rate coefficients are presented here and are compared to values obtained with other experimental apparatuses and theoretical predictions.

In the following text some non SI units are used. This is mostly due to following conventions usually used in spectroscopy and to allow a straightforward comparison with other published results.

2 The H_3^+ ion

2.1 History of H_3^+

Since the discovery of the protonated hydrogen (H_3^+) in 1911 by *J.J. Thomson* [1][2] in one of the first mass spectrometric studies (see **Figure 2.1**), this simplest polyatomic molecular ion has received lots of attention. Although Thomson immediately recognized that the then unknown signal could be H_3^+, he was skeptical and kept on using the designation X_3^+. However the rest of the scientific community was not so skeptical. In 1916 *Dempster* showed [3] that H_3^+ is the dominant ion in Hydrogen plasmas. The main formation channel of H_3^+ is the ion molecule reaction

$$H_2^+ + H_2 \rightarrow H_3^+ + H\,. \tag{2.1}$$

It was first formulated in the work of *Hogness and Lunn* in 1925 [4]. This reaction is highly exothermic (1,7 eV) and lacks an activation barrier [5] and is quite fast with a rate constant of $k_{(300\ K)} = 2\times10^{-9}$ cm^3s^{-1} [6]. The structure of H_3^+ was for a long time an open question. In 1935 *Coulson* and coworkers [7] predicted that H_3^+ has the structure of an equilateral triangle with a bond length of 0.85 Å which is very close to presently used value of 0.87 Å. Some scientists did not accept these predictions at that time, but after the appearance of computers, *Coulsons* predictions were confirmed [8] and the triangular shape of H_3^+ was accepted. Experimental confirmation of the structure had to wait until 1978 for the work of *Gaillard et al.* [9]

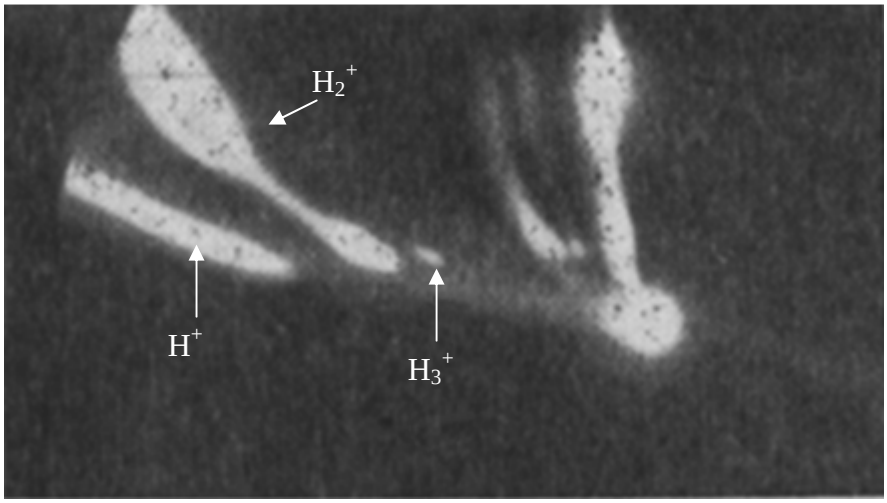

Figure 2.1 Picture of the photographic plate from the first observation of H_3^+ (from *Thomson 1912*[2])

The most common element in interstellar space is hydrogen, with more than 92% off all nuclei in the universe. Majority of the remaining 8% belongs to He, which is not chemically active. Since H_3^+ is so easily crated in hydrogen rich environments through the reaction (2.1), *Martin et al.* proposed that protonated hydrogen should be present in space [10]. He argued that in interstellar space H_2 is continuously bombarded by high-energy cosmic rays γ that can knock out an electron and ionize the molecule

$$H_2 \xrightarrow{\gamma} H_2^+ + e^- . \tag{2.2}$$

This is quickly followed by reaction (2.1) creating H_3^+. In 1973, using gas-phase chemistry models *Herbst and Klemper*[11], and independently *Watson*[12], recognized the importance of H_3^+. Because H_3^+ has a lower proton affinity (4,4 eV) than almost all other atoms and molecules present in interstellar space it acts as an effective proton donor via the proton transfer reaction

$$H_3^+ + X \rightarrow XH^+ + H_2 , \tag{2.3}$$

where (*X)* is an atom or molecule with higher proton affinity than H_2. This way a complex and broad network of ion molecule reactions (see **Figure 2.3**) can be initiated leading to a surprisingly rich and complex chemistry of various space objects [13][14][15].

Figure 2.2 The aurroral emission from H_3^+ on Jupiter taken in the 3.9 μm region. IR picture of the polar regions is superimposed over a visible picture. The infrared image was taken by NASA IRTF satellite. Reprinted from *Miller et al.* 2000 [20]

For a direct observation of H_3^+in interstellar space its spectrum had to be known and observed in laboratory first. But theoretical calculations quickly showed that H_3^+ has no bound electronically excited states and its ground state does not have any dipole moment, therefore the spectrum of H_3^+ does not contain any usable transitions in the ultra-violet or visible region. Only available option for its detection

was the infrared ro-vibrational spectrum. First spectroscopic laboratory observation of H_3^+ was reported by *Oka* in 1980[16] who used multi-path laser absorption spectroscopy.

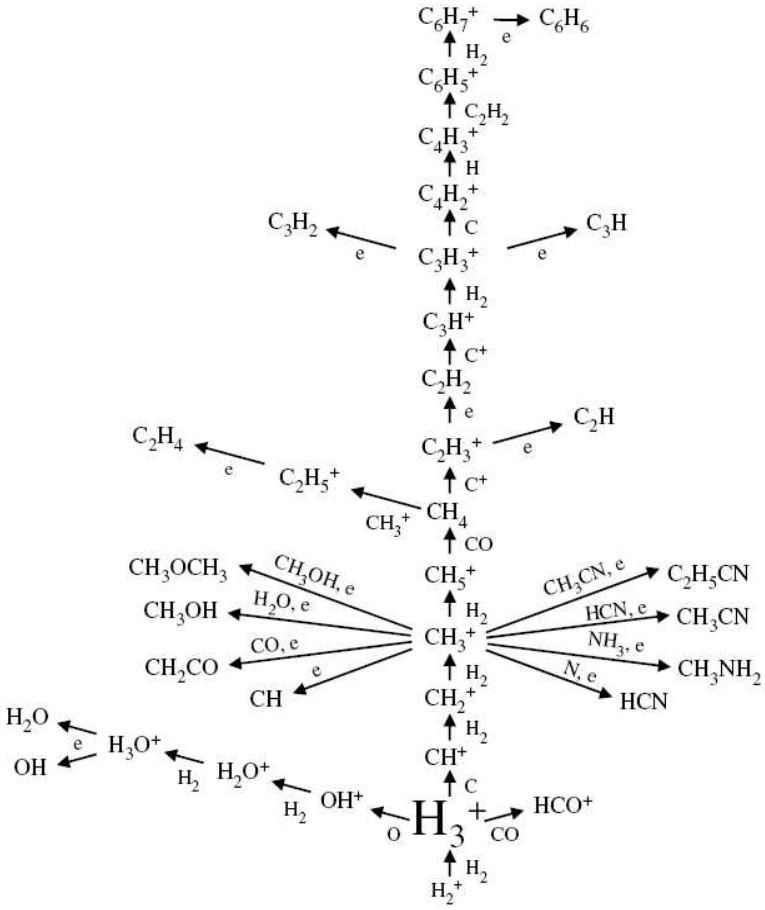

Figure 2.3 Schematic representation of an ion molecule reaction chemistry network in interstellar space initiated by the H_3^+ ion, reprinted from [13].

First detection of H_3^+ beyond Earths atmosphere was in emissions from the auroras on Jupiter [17] (see **Figure 2.2**). Soon discoveries on other gas giants of our solar system followed, Uranus [18] and Saturn [19]. This gave astronomers new insights into the inner workings of ionospheres of these gas giants. Today it is well accepted that H_3^+ plays an important role in the chemistry of these environments [20].

Geballe and *Oka* accomplished the detection of H_3^+ in dense ($n \sim 10^3$-10^5 cm^{-3}) interstellar molecular clouds in 1996 [21]. They observed the star-forming regions GL 2136 and W33E, where a hot proto-star was used as source of infrared radiation and absorption was observed in the molecular cloud obscuring the object. The discovery of H_3^+ absorption lines in diffuse interstellar medium ($n \sim 10^1$-10^3 cm^{-3}) followed in 1998 by *McCall et al.* [22].

α [10^{-7} cm^3 s^{-1}]	Method	Comment	Reference
2.3	SA		*Leu et al.*, 1973 [23]
2.5	inc. beam		*Peart et al*., 1974 [24]
2.1	merged beam		*Auerbach et al*., 1977 [25]
1.5	ion trap		*Mathur et al*., 1978 [26]
2.1	merged beam		*McGowan et al*., 1978 [27]
≤ 0.2	FALP		*Adams et al*., 1984 [28]
1.5	SA		*Mac Donald et al.*, 1984 [29]
0.2	merged beam	v = 0	*Hus et al.*, 1988 [30]
≤ 0.0001	FALP	estimation	*Adams et al.*, 1989 [31]
1.8	IR spectr..	v = 0	*Amano et al.*, 1990 [32]
1.5		v ≤ 2	
1.1	FALP-MS	v = 0	*Canosa et al*., 1991 [33]
1.5		300 K, v ≤ 2	
0.1 – 0.2	FALP	v = 0	*Smith et al*., 1993 [34],[35]
1.15	Storage ring		*Sundström et al*., 1994*; Larsson et al*., 1995 [36],[37]
< 2	IR laser. spec.		*Fehér et al*., 1994 [38]
1.2	merged beam		*Yousif et al.*, 1995 [39]
1.4 - 2	FALP		*Gougousi et al*., 1995 [40]
0.78	FALP-MS		*Laubé et al*., 1998 [41]
0.7	Storage ring		*Tanabe et al*., 1999 [42]
0.7	CRYRING		*Schneider et al*., 1999 [43]
0.4 - 1.4	AISA	$[H_2]$ depend.	*Kudrna et al*., 2000; *Glosik et al.*, 2000 [44],[45]
1	ASTRID		*Jensen et al.*, 2001[46]
0.03 – 1.4	AISA	$[H_2]$ dep.	*Plasil et al*., 2002 [47]
0.68	CRYRING	Cold ion source	*McCall et al*., 2003 [48]
1.6	SA, CRDS		*Macko et al*., 2004 [49]
0.1 to 1.4	AISA-VT	$[H_2]$ dep	*Glosík et al*., 2005 [50]
0.7	TSR	Cold ion source	*Kreckel et al*., 2005 [51]
0.7	misc. Afterglow	He dependence	*Glosik et al.*, 2008 [52]
0.7	TSR	Para enriched H_3^+	*Petrignani et al.*,2009 [53]
0.7	Cryring	Para enriched H_3^+	*Tom et al.*, 2009 [54]
0.7	TSR	Para enriched H_3^+	*Kreckel et al.*, 2010 [55]
1	SA,CRDS	77 K, Para enriched H_3^+	*Varju et al*., 2011 [56]

Table 2.1 Chronologically ordered experimental values of the H_3^+ recombination rate coefficient obtained with various techniques.

The observed column densities of H_3^+ in diffuse interstellar medium were considerably higher then expected from chemical model calculations. This discrepancy has been extensively debated and the proposed solution, now generally accepted, was to increase the cosmic-ray ionization rate by an order of magnitude (*Indriolo et al.* [57]).

Another parameter of the used chemical-models that could resolve the discrepancy and was also invoked during the debate was the dissociative recombination rate constant of H_3^+. But due to the convincing experimental evidence [42][43] it was ruled out and even used to put constraints on the cosmic-ray ionization rate. This clearly demonstrates the far-reaching implications and importance of experimental laboratory data on species with astrophysical relevance.

2.2 Review of H_3^+ Dissociative Recombination studies

The study of dissociative recombination of the H_3^+ ion is an ongoing effort already for over 60 years. For a very long time it was marked by strong disagreement between various experimental techniques and also with theory. By now many reviews have been written about this endeavor [58][59] therefore only a short overview with the major steps is presented here. The reader is advised to look into these reviews for detailed summaries.

The first experiment with unambiguous identification of the recombining ion as H_3^+ was by *Leu, Biondy* and *Johnsen* in 1973 [23] in a Stationary Afterglow experiment using a mass spectrometer (see **Table 2.1** for the value). In the following decade the experimentally observed values were in agreement with the value obtained by *Leu et al.* In 1984 however *Adams* and *Smith* [28] came to value an order of magnitude lower, using a novel technique the *Flowing Afterglow Langmuire Probe* (FALP). This spurred further theoretical work and soon *Michels* and *Hobs* [60] showed that the potential energy surface of the vibrational ground state of H_3^+ is not intersected by an appropriate repulsive potential curve that could lead to dissociation, thus excluding the fast direct mechanism (see below for details) and supporting the low rate coefficients of *Adams et al*. They also proposed that higher vibrational states ($v \geq 3$) could recombine much faster due to the possibility of suitable curve crossings. This elegantly explained the discrepancy and in the following experiments not only the species but also internal excitation of recombining ions was considered in the interpretation of experimental results. In 1990 *Amano* [32] observed H_3^+ in a stationary afterglow and using infrared spectroscopy came to rate coefficients one order of magnitude higher than *Adams* both for the ground and higher vibrational states. In 1993 were the measurements of *Adams* and *Smith* repeated by *Smith* and *Španěl* [34][35] yielding the same low rate coefficients as nine years before.

Beam experiments on this topic started with the single pas merged beam technique in 1988 by *Hus et al.* [30] and gave low values of the rate coefficient.

Later experiments by *Yousif et al.* [39] did not confirm those low values. Single pas merged beam techniques were naturally expended into storage ring experiments, where studied ions are circulating in a storage device for a considerable time (tens of seconds) allowing the vibrationaly-excited ions to spontaneously emit radiation and relax to the ground state. The first storage ring experiments with H_3^+ were performed in Stockholm on the CRYRING apparatus in 1993 [36][37]. The measured cross sections were recalculated to a thermal rate coefficient $\alpha(300\ K) = 1.15\times10^{-7}\ cm^3\ s^{-1}$ that was in agreement with previous single pas merged beam experiment of *Yousisf et al.* Concerns about the vibrational population distribution lead to further experiments with better control of H_3^+ internal excitation, yielding a thermal recombination rate coefficient $\alpha(300\ K) = 0.7\times10^{-7}\ cm^3\ s^{-1}$ [42][43].

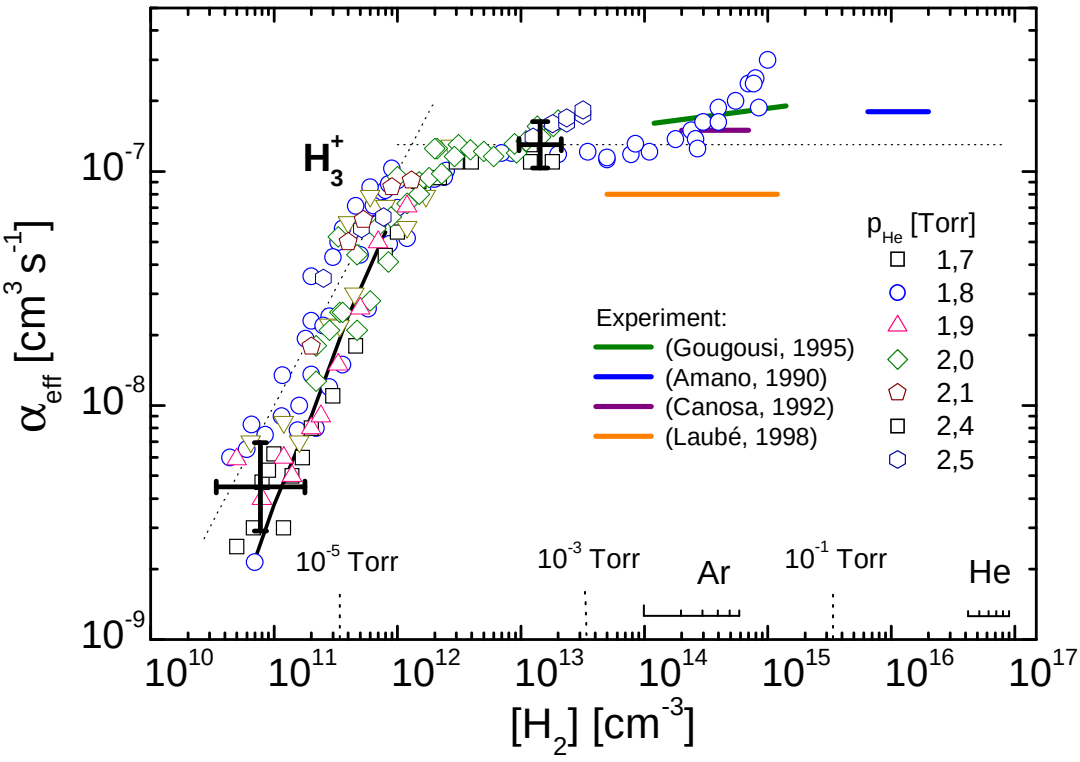

Figure 2.4 The effective recombination rate coefficient of H_3^+ measured usign the AISA apparatus. Reprinted from [61]

Further improvement in storage ring experiments was achieved by the utilization of cold-ion sources. The CRYRING facility used a supersonic expansion source [48] and the TSR in Heidelberg used a cryogenic 22-pole radio-frequency trap [51]. Both experiments gave a thermal recombination rate coefficient of $\alpha(300\ K) = 0.7\times10^{-7}\ cm^3\ s^{-1}$. In 2008 and 2009 storage ring experiments have been also performed with H_3^+ ions with specific nuclear spin at both facilities. Para-H_3^+ ions were injected into the storage ring and an increase in recombination rate coefficients

was observed [53][54]. Latest results from the TSR indicate that although the vibrational levels were relaxed to the ground state the transverse kinetic temperature of the recombining ions was still several hundred Kelvin, despite electron cooling techniques, in both storage ring facilities [55]. In all spin selected storage ring experiments the composition characterization of the recombining ions has been performed prior to the injection into the storage ring and no in situ information on the spin state was available.

As for plasmatic experiments, the group of *prof. Glosik* showed that the effective recombination rate coefficient observed in plasmatic experiments depends strongly and nonlinearly on H_2 number density (see **Figure 2.4**). Both stationary (*Advanced integration Stationary Afterglow* - AISA) and flowing afterglow (*Flowing Afterglow Langmuire Probe* - FALP) techniques were used [61][62][63] combined with Langmuire probe and Mass spectrometer diagnostics. At first look these results suggest that the limit for $[H_2]\rightarrow 0$ should be taken as the value for the recombination rate coefficient in interstellar space, i.e. a value lower than 3×10^{-9} cm^3 s^{-1}. After closer inspection one finds that at low H_2 number densities, the internal excitation of H_3^+ is unknown, with no good assumptions about it available either. To verify the internal excitation and other parameters of the recombining ions experiments utilizing CRD spectroscopy were performed [64][65][66]. Unfortunately the low H_2 region could not be probed due to low H_3^+ number densities generated in the experiment (see Chapter 5) so the interpretation of those results remains still open. Rise of the rate coefficient in the high H_2 density region ($H_2>10^{14}$ cm^{-3}) was attributed to the formation of H_5^+, a very fast recombining ion ($\alpha = 2{,}5\times10^{-6}$ cm^3 s^{-1}) [67]. The experiments also clearly demonstrated that in multi-collision environments, such as plasmatic experiments, the observed deionization process of H_3^+ is not a pure binary process. In 2008 the discovery of the ternary helium assisted recombination channel brought the past and present afterglow experiments, with He as buffer gas, into agreement with storage ring experiments and theoretical predictions [52] (attached publication II). The only experiments not yet reconciled are plasma experiments in pure H_2 [32]. Today the main goal of experimental investigations is the verification of the state specific recombination rate coefficients, which is the goal of this work also.

2.3 Mechanism of Dissociative Recombination

The process of Dissociate recombination is the most important process for the destruction of molecular ions in many environments, with rate coefficients commonly reaching values of 10^{-7} cm^3 s^{-1} [68]. Among others, dissociative recombination of O_2^+ was proposed as a solution to the 557.7 nm emissions in *aurora borealis* of earth's ionosphere. It is the main destruction process for the H_3^+ molecular ion. Many theoretical mechanisms have been proposed to explain this process. Short overview of some of them follows.

2.3.1 Direct recombination model

In the direct process proposed by *Bates* in 1950 [69] the incoming electron excites an electron of the molecular ion AB^+ and then is captured into a repulsive state (at a rate k^*) of the doubly excited neutral molecule AB^{**}. The capture proceeds through a Franck-Condon type transition. The neutral fragments start to move apart but until they cross the stabilization point the excited complex can still auto ionize (with frequency ν_a). The kinetic energy of the electron is transmitted into the kinetic energy of fragments not by a collision but by the rearrangement of the whole electron cloud. The doubly excited neutral molecule then dissociates with frequency ν_s. The process is illustrated in **Figure 2.5** and can be written up as

$$e^- + AB^+(v_i) \underset{\nu_a}{\overset{k^*}{\leftrightarrow}} (AB^{**})_r \xrightarrow{\nu_s} A^* + B\,. \tag{2.4}$$

This mechanism is fast and many molecular ions recombine this way. But for this process to be available a suitable arrangement of potential energy surfaces (PES) must be present to allow for the needed Franck-Condon type transition. As was already mentioned H_3^+ lacks such favorably positioned PES.

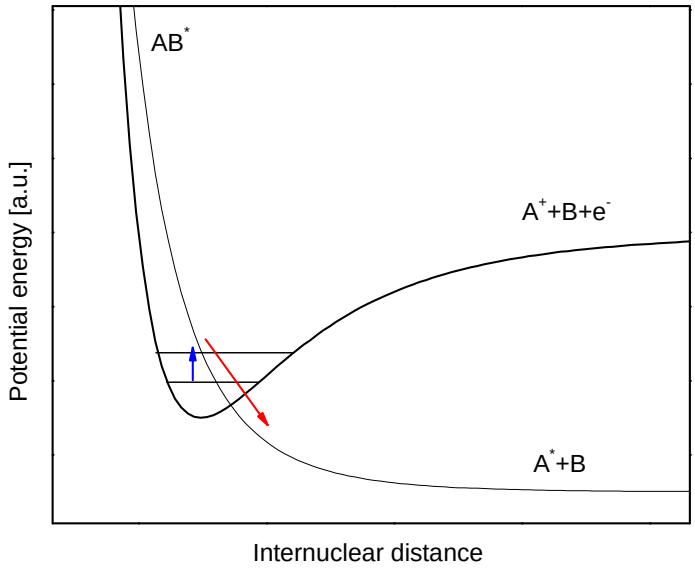

Figure 2.5 Schematic representation of the PES for the direct recombination process.

2.3.2 Indirect recombination model

For molecular ions lacking the appropriate PES crossings, *Bardsley* has invoked the so-called indirect process in 1968 [70]. In contrast to the direct process, the incoming electrons energy is used to vibrationally excite the molecular ion AB^+ and the electron is then captured onto a attractive-bound Rydberg orbital of the vibrationaly-excited molecule $AB^*(n,v)$, if available. The molecule further proceeds

through the repulsive state AB^* and dissociates as in the direct mechanism. The indirect mechanism is responsible for characteristic Lorentz shaped resonances in the recombination cross-section dependence on energy. The process is illustrated in **Figure 2.6** and can be written up as

$$e^- + AB^+(v) \leftrightarrow \left[AB^*(n,v)\right]_a \leftrightarrow \left(AB^*\right)_r \rightarrow A^* + B\,. \tag{2.5}$$

In most molecular ions both the direct and indirect processes occur simultaneously with the direct setting the magnitude of the recombination and the indirect causing resonance structures in the cross-sections energy dependence. In the absence of appropriate PES crossings only the indirect process leads to dissociation and slow recombination rate coefficients are observed.

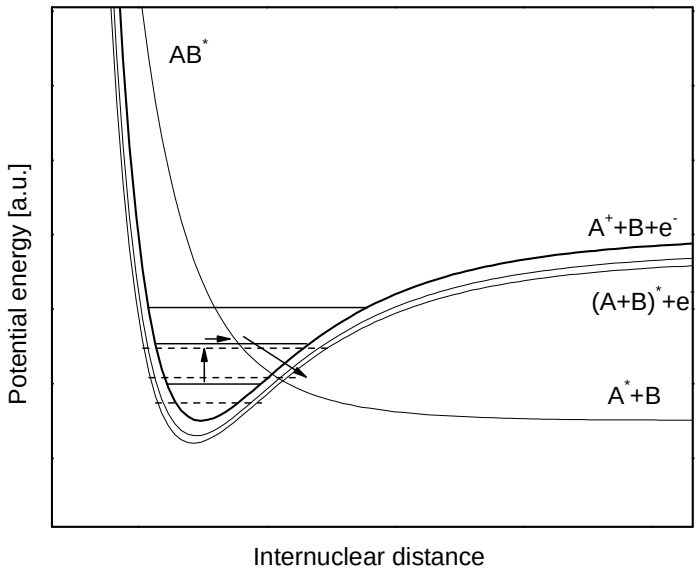

Figure 2.6 Schematic representation of the indirect recombination process

2.3.3 Multistep indirect model

Although H_3^+ lacks suitable PES crossings to recombine through the direct recombination process the high experimentally measured recombination rate coefficient therefore suggest still another recombination process besides the two already mentioned. For some molecular ions *Bates et al*. presented the so called multistep [71] indirect model of recombination. It is basically a chain of multiple indirect process steps. The incoming electron first excites the molecule to the first vibrational state and is captured in a high Rydberg orbital. Afterwards more energy is transferred to the vibration of the nucleus from the decreasing quantum number of

the electron Rydberg orbital. The process repeats until a vibrational level with suitable curve crossing is reached from which the ion can dissociate. Although the multistep process was a step in the right direction by stepping outside the Born-Openheimer approximation it still resulted in low theoretical recombination rate coefficients 1×10^{-9} cm^3s^{-1} at low temperatures [72]. The breakthrough came with the work of *Kokoouline* and *Green* who performed for the first time a full 3D calculation of the nuclear dynamics. They showed that the non-Bron-Openheimer symmetry breaking Jahn-Teller effect was responsible for the fast recombination of H_3^+ [73][74]. The resulting thermal rate coefficient dependence on ambient temperature is shown in **Figure 2.7**. This theoretical work shows remarkable agreement with storage ring experiments in reproducing some of the finer features of observed recombination cross section dependence on particle energy[75][76].

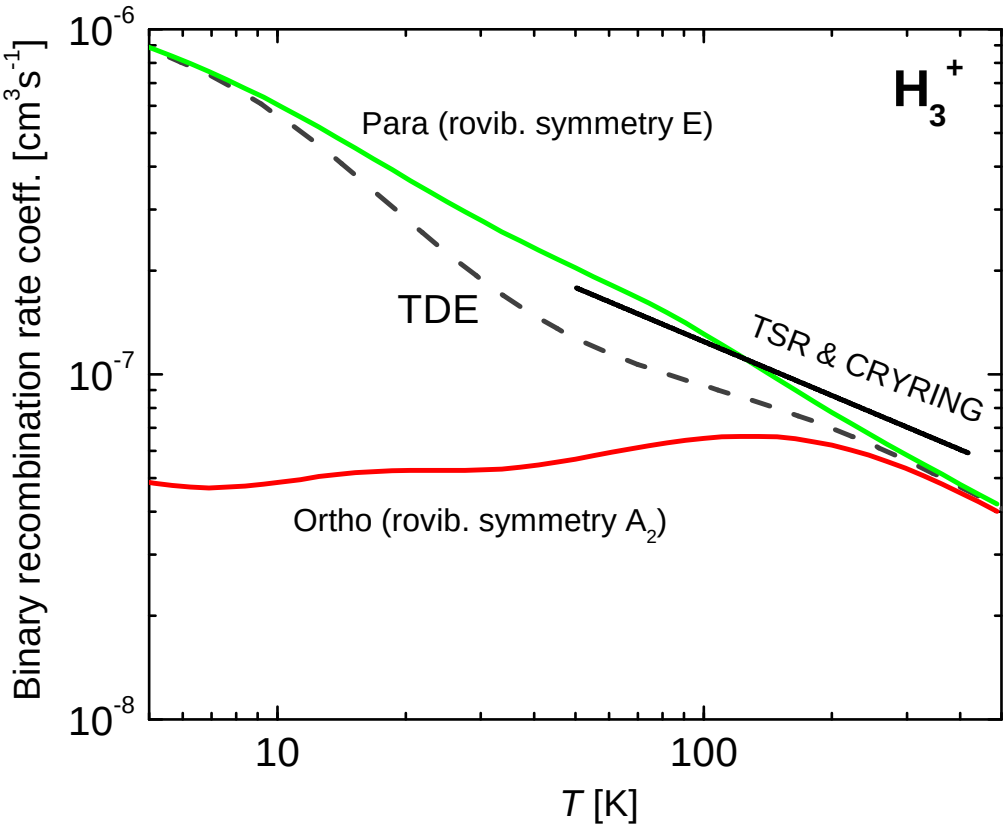

Figure 2.7 Theoretical predictions of the recombination rate coefficient of H_3^+ according to Pagani[76]. A Very good agreement with experimental data from storage ring experiments with normal para/ortho H_3^+ distribution.

2.4 The Ternary recombination channel

Although the theoretical predictions and storage ring experiments came to an agreement on the thermal recombination rate coefficient of H_3^+ after the publication of *Koukooline* et al. [74] in 2003 the plasmatic experiments remained still

out of line. To make matters more interesting the different plasma experiments were in contradiction not only with storage ring experiments but also with each other. The breakthrough came with the discovery of the ternary helium-assisted recombination channel [52] (reprinted as Attached publication II). This process is different from the "classical" ternary recombination channel proposed by *Bates and Khare* [*77*]. The classical ternary model relies on the simultaneous collision of three particles and is most effective at high pressures (> 1 atm.). Although buffer gas pressure dependence of the H_3^+ recombination rate was discussed, it has never been looked after because at the usually used pressures no noticeable effect was suspected when the classical theory was considered. The classical theory predicted a ternary coefficient of 10^{-27}cm^{6}s^{-1} that would contribute only at the level of 10^{-9} cm^{3}s^{-1} to the resulting rate coefficient. Also, the nonlinear dependence on H_2 number density varies the effective recombination rate coefficient by almost three orders of magnitude (**Figure 2.4**), which obscures the pressure dependence. Since all the details of this dependence on H_2 are still not fully understood, it was difficult to choose a region where one should look for buffer gas pressure dependences. For a detailed discussion about selecting the appropriate H_2 number density see attached publication III. Experimental data suggests that the dependence of the recombination rate coefficient on buffer gas density is linear (see Figure 2 in Attached publication II) so we can write:

$$\alpha_{eff} = \alpha_{bin} + K_{\mathrm{He}}[\mathrm{He}]. \tag{2.6}$$

It is important to stress again that this process is different than the one proposed originally by Bates. This process relies on a completely different mechanism and is therefore two orders of magnitude more effective. The mechanism proposed for this "new" ternary channel in simplified form is as follows. In electron scattering so called rotational auto-ionization resonances of the neutral $H_3^{\#}$ molecule are formed. The cross-sections for creation of such resonances depend strongly on the collisional energy and reflect the structure of available Rydberg states of the neutral H_3 molecule. Normally their contribution to the $H_3^+ + e^-$ recombination rate is low since almost always such resonances auto-ionize back to the free electron and H_3^+ ion. Theoretical calculations show (see Attached publication II and III) that the lifetime of such resonances can be over 100 ps (see **Figure 2.8**). If during the time before this resonant state auto-ionizes it undergoes a collision with a buffer gas atom (Helium) the collision can lead to a change of the electronic state of the outermost electron or of the rotational state of the H_3^+ ion. This can make auto-ionization energetically impossible or at least less probable. The formula for the rate coefficient of such a process can be written as:

$$K_{\mathrm{He}} = k^l \Delta t \alpha^*, \tag{2.7}$$

where k^l is the rate of collisions between He and $H_3^\#$ that lead to the eventual dissociation of $H_3^\#$, Δt - the time the electron spends close to the ion compared to a pure Coulomb collision (delay time), α is the rate coefficient for the formation of $H_3^\#$. The temperature dependence of the ternary rate coefficient after thermal averaging over a Maxwell-Boltzman distribution is shown in **Figure 2.9** (solid lines). Experimental data points are also included. Although this calculation leaves ample space for improvement (i.e. k^l dependence on energy), it readily demonstrates the magnitude of such a process. Similar ternary dependence has been observed also for D_3^+(see Attached publication IV).

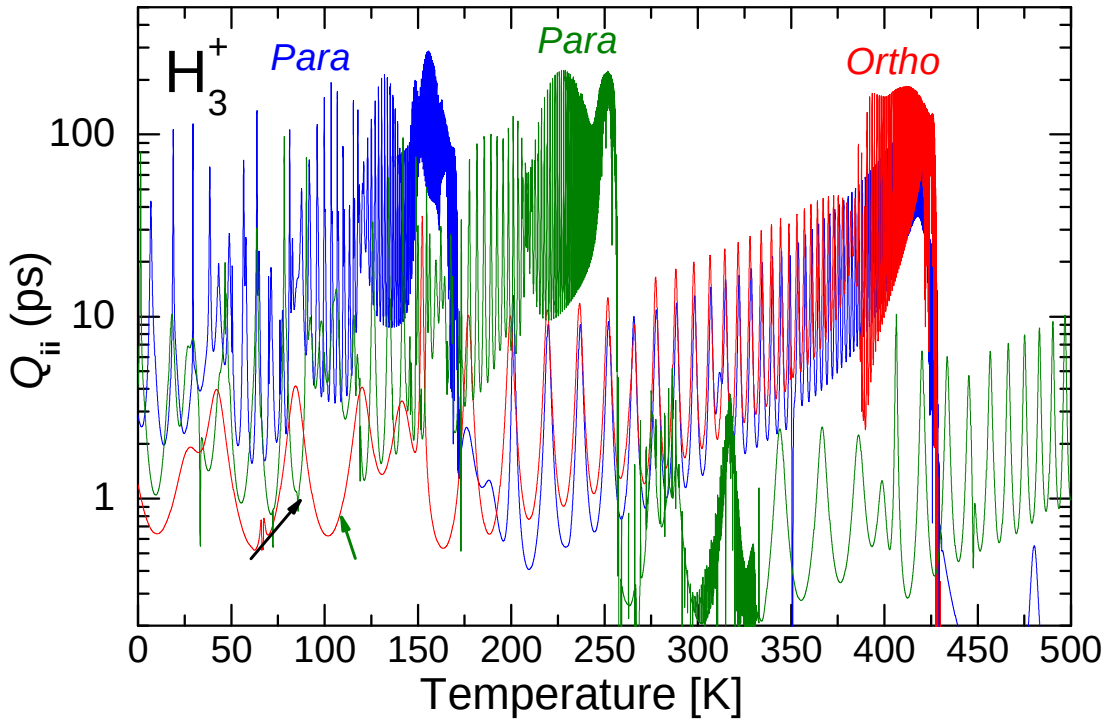

Figure 2.8 Lifetimes of rotational auto-ionizing resonances in picoseconds as a function of collision energy expressed as temperature equivalent. For details of the calculation see Attached publication III. It is evident that many resonances have a significantly long lifetime.

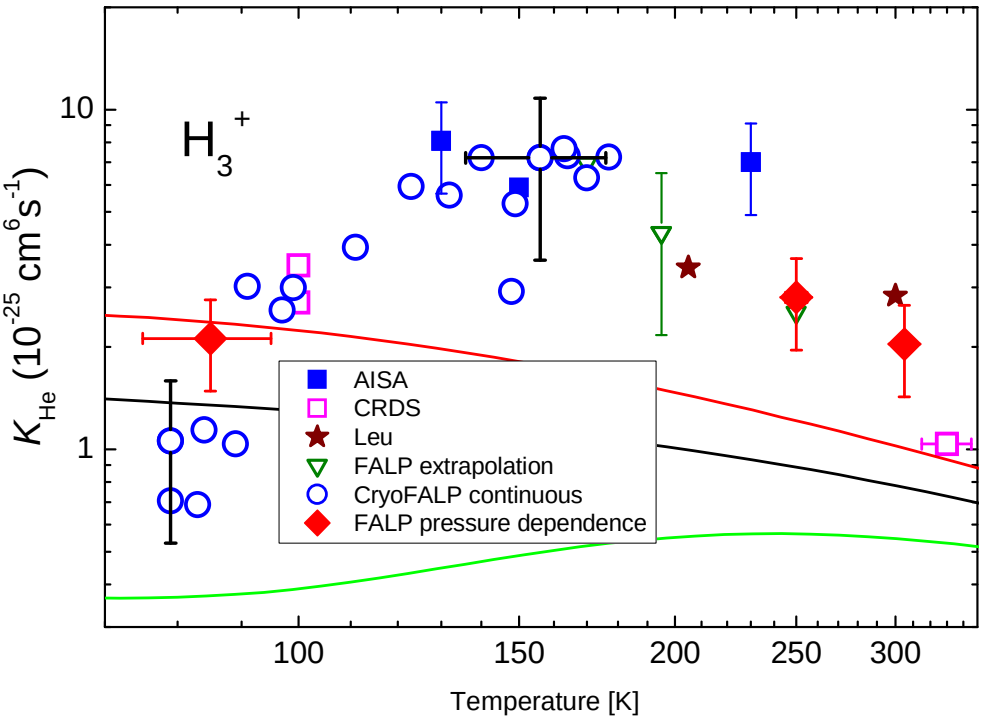

Figure 2.9 Thermally averaged theoretical ternary recombination rate coefficient compared to experimental values obtained with different apparatuses and diagnostic techniques.

2.5 H_3^+ quantum numbers

A short overview of the quantum numbers used to describe H_3^+ will be presented in the following paragraphs together with an overview of the notation of H_3^+ transitions. The H_3^+ ion in its ground state has the form of an equilateral triangle with an average bond length of 0.85 Å. It belongs therefore to the point group C_{3v}. The total angular momentum (F) and the parity (±) are the only rigorous quantum numbers for any molecule. This is a consequence of isotropy and inversion symmetry of free space. In the case of H_3^+ the total angular momentum is given by the vector sum of the spin angular momentum I and the angular momentum of the nuclei movement J. The interaction of the nuclear motion with nuclear spin is rather weak so for H_3^+ both J and I can be considered good quantum numbers along with parity (±). As H_3^+ contains three protons each with a spin of ½ the nuclear spin angular momentum I can have two values. States with $I = 1/2$ are commonly referred to as *para* and states with $I = 3/2$ as *ortho*. Ortho states have the A2 symmetry and para states the E symmetry.

In addition to these good quantum numbers also a set of approximate quantum numbers describing the vibrational motion is commonly used at low energies to better describe the behavior of H_3^+. The number of vibrational quanta in the symmetric "breathing" mode is labeled v_1. This mode does not induce any dipole

moment and is therefore infrared inactive. The v_2 vibrational mode is doubly degenerated and has a bending mode v_{2x} and a symmetric stretch v_{2y} mode (see **Figure 2.10**). The superposition of the two v_2 modes leads to a circular motion with the corresponding vibrational angular momentum labeled *l*. It can have values from -v_2 to v_2 in steps of two. These states are often labeled as $v_2 v_2^l$. The projection of *J* onto the molecular axis (labeled *k*) is a good quantum number for most molecules, but in H_3^+ there is a near degeneracy for states with the same $|k-l|$ and a strong level mixing occurs. Instead a new quantum number $G = |k-l|$ is used. For the vibrational ground state $G = k$.

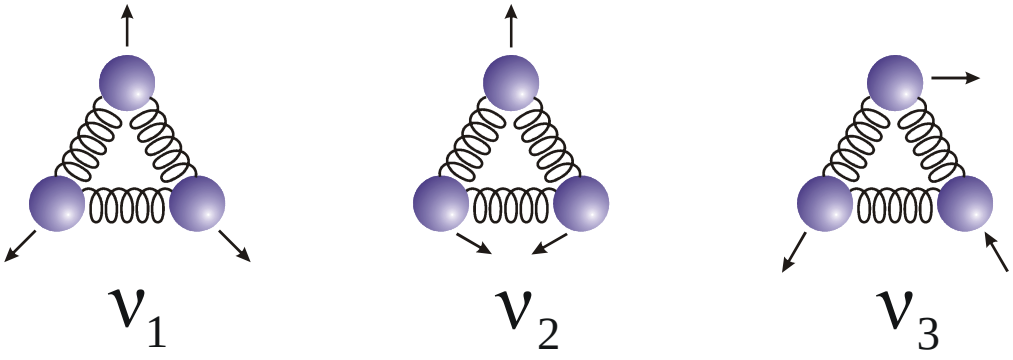

Figure 2.10 Schematic representation of the vibrational modes of H_3^+. The symmetric "breathing" mode ν_1. The ν_2 mode is doubly degenerated and has a bending mode ν_{2x} and a symmetric stretch ν_{2y} mode. Reprinted from [78]

The Pauli principle also imposes some restrictions on the total wave function of the H_3^+ system. As a consequence a relationship between particular nuclear spin modifications and the quantum number *G* arises. For *ortho* states (I = 3/2) only levels with $G = 3n$ and for para states only levels with $G = 3n+1$ fulfill the symmetry conditions imposed by the Pauli principle. States with even *J* in the ground vibrational states and $G = 0$ have the A1 symmetry. Wave functions with the A1 symmetry although mathematically possible do not satisfy the Pauli principle so the corresponding H_3^+ states do not exist [79][80]. The most notable consequence of this is that the ground state with of H_3^+ ($J = 0$, $G = 0$) does not exist. But nevertheless it is common to zero-offset the energies of other levels to this non-existing ground state. A one-dimensional projection of the H_3^+ potential energy surface with calculated vibrational levels is shown in **Figure 2.11**.The distribution of rotational energy levels of the fundamental vibrational level is shown in **Figure 2.12**. At higher energies where assignment with approximate quantum numbers fails due to severe line mixing only the good quantum numbers (J, I, ±) are used together with an energy-ordering index *n* for levels with other quantum numbers equal.

For the context of this work it is important to note that the dipole operator μ does not operate on the nuclear spin wave functions therefore the nuclear spin, the

para/*ortho* state of H_3^+, does not change in radiative transitions. In other words I obeys the selection rule $\Delta I = 0$ and the nuclear spin state of H_3^+ (*para* and *ortho*) changes only in reactive collisions, which will be briefly discussed in the following chapter. A detailed discourse on H_3^+ structure, quantum states and radiative selection rules can be found in [80][81][82][83].

In this work the H_3^+ quantum states and transitions labeling scheme proposed by McCall [84] is used. Energy levels are designated by

$$\{J,G\}\{u\,|\,l\}\mathrm{v}_1\nu_1 + \mathrm{v}_2\nu_2^{|\ell|}. \tag{2.8}$$

For states that form an l resonance pair, i.e. have the same G but different k and l, the symbols u and l are used to distinguish if the level is the upper or lower energy level of this l resonance pair, respectively. For transitions the notation is

$$^{[n|t]}\{P\,|\,Q\,|\,R\}(J,G)^{[u|l]}_{[u|l]}\mathrm{v}_1\nu_1 + \mathrm{v}_2\nu_2^{|\ell|} \leftarrow 0, \tag{2.9}$$

where PQR is the common ΔJ = {-1|0|1} notation, respectively. The [n|t] superscript labels the Δg = –3 and Δg = +3 respectively ($g = k - l$), for Δg = 0 no notation is used. The J and G quantum numbers of the lower state are used. The u and l superscript and subscript designate the position of the upper and lower level, respectively, in the l resonance pair.

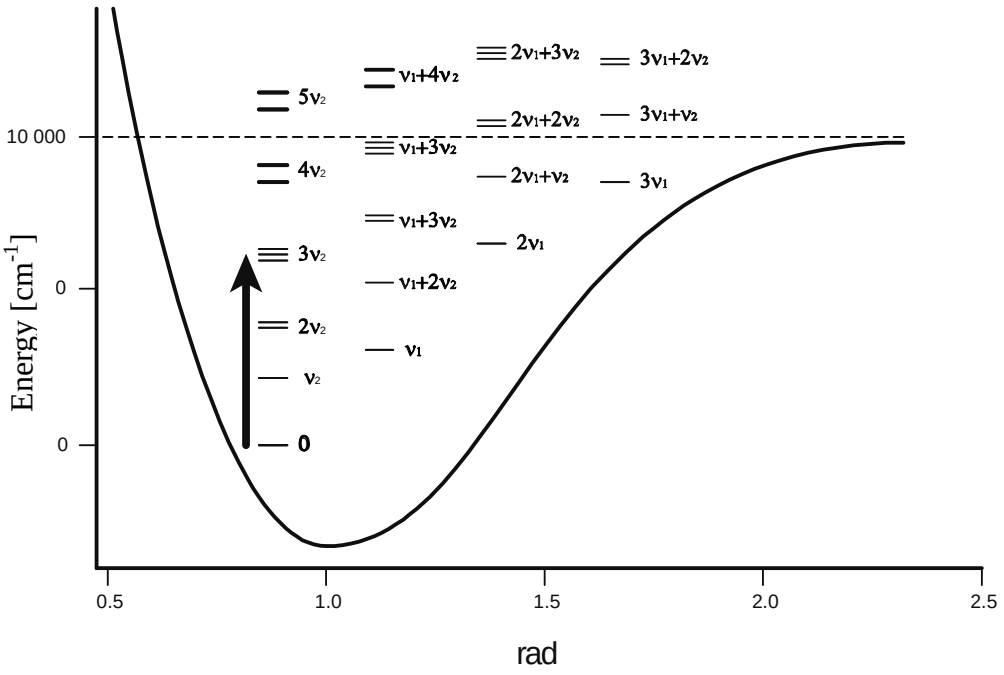

Figure 2.11 A one-dimensional projection of the H_3^+ potential energy surface. The length of the two H-H bonds is kept constant and the angle θ between them is varied. Calculated vibrational levels are also plotted. Dashed line represents the barrier to linearity. Reprinted from [84]

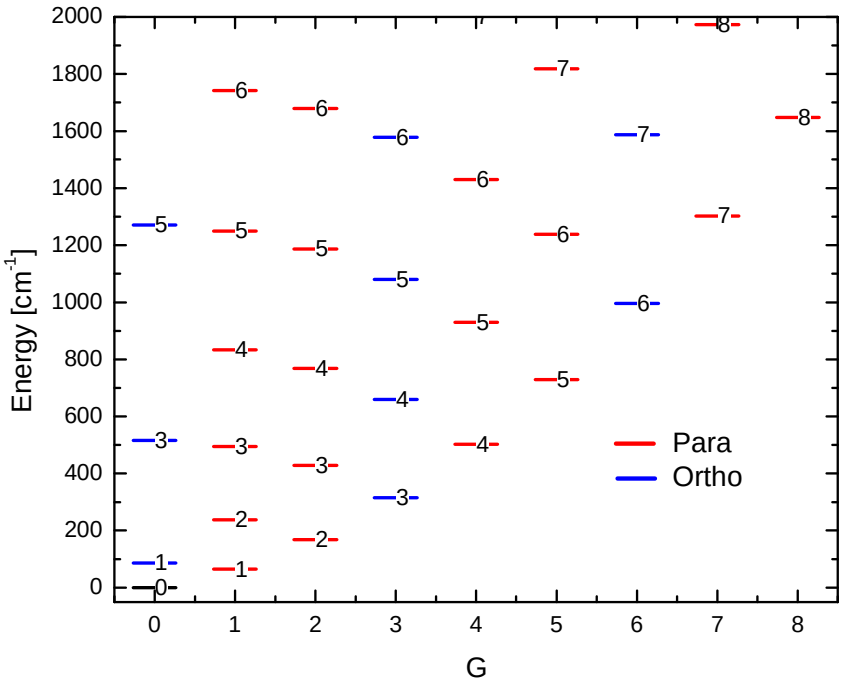

Figure 2.12 Distribution of H_3^+ rotational energy levels of the ground vibrational state. Levels are labeled with the corresponding value of the quantum number *J*. Red color designates *para* states Blue color designates *ortho* states. The non-existing (0,0) state is black; rest of the symmetry forbidden states is omitted. Compiled from data from [79]

2.6 The H_3^++H_2 reaction complex

Since H_2 is the most abundant molecular species in the universe and H_3^+ is the most abundant molecular ion, the reaction

$$H_3^+ + H_2 \rightarrow \left(H_5^+\right)^* \rightarrow H_3^+ + H_2 \qquad (2.10)$$

is one of the most common molecular reactions. Although at first sight the reaction bears no evident complications and no interesting features either. But the existence of different spin modifications of both H_2 and H_3^+ hides a great deal of complexity. Study of this reaction is an ongoing effort both theoretically and experimentally. The properties of reaction (2.10) at low temperatures (~10 K) have profound implications for interstellar chemistry. This work focuses on the state sensitive recombination studies of H_3^+ it is therefore necessary to keep in mind the peculiarities of this reaction in order to obtain reliable values of the recombination rate coefficient. A short overview of theoretical predictions for this reaction will be presented.

Similar to H_3^+ (mentioned above), H_2 also exists in two different nuclear spin symmetry configurations, *para* (anti-parallel spin orientation) and *ortho* (parallel spin orient.). The interaction of nuclear spin with other degrees of freedom is very small in both H_3^+ and H_2. Therefore under normal circumstances in radiation

processes and inelastic collision the energy of the interaction is small compared to the energy gap between different spin symmetries and nuclear spin is not affected [85][86]. Closely degenerate states of different symmetries that could circumvent this energy barrier are usually not available for this two species. This circumstance was used in the presented work to create Hydrogen gas with an enriched population of states with para spin symmetry using the apparatus described in chapter 4.5. In reaction (2.10) a reaction complex is formed $(H_5^+)^\#$ that at first sight can lead to full scrambling of involved nuclei. Simple combinatorics suggests that 16 reaction channels are possible for this reaction with regard to different spin combinations. But the consequences for nuclear spin of participating particles after this reaction are not so straightforward. Different theoretical approaches have been tried to tackle the problem in detail and gave similar but not the same results. Full quantum scattering study of this reaction that would confirm either theoretical calculation has not been performed to date.

First one to quantify the probabilities of the various possible reaction channels of (2.10) was Quack in 1977 [87]. In his paper he presented "a simple general method for obtaining selection rules for the ro-vibronic states of reactant and product molecules connected in a reactive collision". His work was based on group theory of permutation-inversion operations and showed that in reactions involving three or more identical particles quite strong selection rules apply. In other words the final product state and product distribution are a function of the initial state of the reactants and that some pathways are even forbidden. Experimental evidence of such selection rules was presented by *Cordonnier* and *Oka* [88][89] in a pure Hydrogen plasma using H_2 with different fractions of para-H_2 states as a precursor.

Oka presented an alternative but equivalent theoretical description for calculating the branching ratios using angular momentum algebra [90]. Creation of H_3^+ in reaction (2.1) is treated as a simple proton transfer process. This is not fully correct but is a good approximation at higher temperatures. Energy of different states involved in the reaction has been neglected in both theoretical treatments (*Oka* and *Quack*) which is acceptable at high temperatures, as many rotational states are available, but the results of this work can not be applied to process in interstellar space. The reaction probabilities for different pathways of the H_3^+ formation reaction (2.1) derived by *Oka* are presented in Table 2.2

Park and *Light* [91] expanded the work of *Oka*, they used a micro-canonical statistical approach and assumed complete proton scrambling of the reactants. They arrived at state to state rate coefficients, including para/ortho conversion, and their dependence on collision energy down to astrophysical relevant temperature equivalents. The high temperature limit of their work was approaching values obtained by Oka's. Relative branching ratios obtained by *Oka* and *Park* & *Light* are shown in **Table 2.3**. Basically the same theoretical approach was used by *Hugo et al*. [92] but they extended their work on isotopic reactions with deuterated analogous and focused on low temperatures (<50 K).

$p/oH_2^+ + p/oH_2$	ortho H_3^+	para H_3^+
oo	2/3	1/3
op	1/3	2/3
po	1/3	2/3
pp	0	1

Table 2.2 The possibilities of various reaction channels in the $H_2^+ + H_2$ reactive collision. First column indicates the reactant spin configuration (p – para, o – ortho). The probability of forming in the particular spin configuration is in the corresponding row. It is evident that in first collision in pure paraH_2 only paraH_3^+ is created.

Gerlich presented an alternative approach by using a dynamically biased statistical theory. Besides using the good quantum numbers for all bimolecular collision the total energy, total momentum, total angular momentum and parity he explicitly imposed spin conservation and carefully considered the anisotropic interaction potential[93]. The results of his approach have been challenged by others, see discussion in Appendix A of ref [91]. The results of *Gerlich et al.* and *Hugo et al.* focus mainly on astrophysically relevant low temperatures (<10 K) and do not reach the range 77 – 200 K and therefore are not reprinted here.

	pp	po	op	oo
Angular momentum algebra (Oka [90])				
pp	2/5	2/5	0	1/5
op	0	1/2	1/ 4	1/4
po	2/15	7/15	1/6	7/30
oo	1/15	7/30	1/12	37/60
80 K full scrambling (Park and Light [91])				
pp	1,77	0,11	0	0,05
op	0	0,22	1,61	0,1
po	0,26	0,95	0,26	0,46
oo	0,11	0,43	0,1	1,27

Table 2.3 Possibilities of various reaction channels in the $H_3^+ + H_2$ reactive collision, excluding the H_5^+ formation. Reactant spin configuration is in the first column and the probability of various product channels is in the corresponding row. Data from Oka 2004 [90] and Park and Light 2007[91]. In column and row description the first letter is the spin of H_3^+ second is the spin of H_2.

The full extent of this spin selection rules and branching ratios on the overall plasma composition can be evaluated only through numerical modeling of the kinetics of all participating species and their particular spin modifications. Since knowledge about the precise equilibrium creation process is not of vital importance for the work presented in this thesis numerical kinetic modeling was not performed but is underway as future work of the group. The main conclusion of the mentioned works for the experiments presented herein is that it is possible to change the para/ortho H_3^+ ratio by changing the ratio of para/ortho states in the used reactant H_2 gas.

3 Absorption spectroscopy

3.1 *Spectroscopy general and History*

Optical spectroscopy is by far the single most used and most versatile analytical technique in physical sciences. We can trace its origins to the work of Newton who first dispersed sun light into its spectral components using a glass prism. Today the number of available and commonly used spectroscopic techniques is staggering. Most of them were realized only after the advent of the laser in 1960 and its many different realizations. Spectroscopy is commonly used to determine number densities of particular components of studied samples. The main advantage of spectroscopy is its ability to observe particular quantum states of the observed sample, at right conditions, thereby giving valuable information about the inner composition of observed matter. As molecular and atomic spectra are a direct consequence of the quantum properties and quantum behavior of matter, it is also the technique of choice for feedback information on quantum computations. A short introduction into absorption spectroscopy in gaseous environments will be given here.

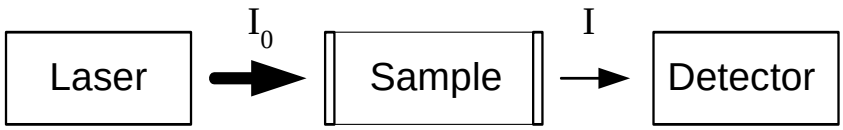

Figure 3.1 Schematic picture of the simplest form of laser absorption spectroscopy measurements. A tunable laser passes through a sample of interest.

3.1.1 Absorption spectroscopy basics

In its simplest form, absorption spectroscopy measures the frequency dependent decrease of radiation intensity (photo-absorption) after it has passed through a sample of interest **Figure 3.1**. As the light source for absorption spectroscopy many different sources have been and are still used. Before the invention of laser mostly high-pressure lamps were used to generate broadband radiation, which was than dispersed into its spectral components by means of a wavelength selective element (grating, prism etc.)

In general when monochromatic light of frequency v with intensity I passes through a homogenous absorbing medium its intensity decreases. This decrease depends on the absorption coefficient $\alpha(v)$, initial intensity I_0 and distance traveled through the absorbing medium x, according the Lambert-Beer law:

$$\frac{dI(x,\nu)}{dx} = -\alpha(\nu) I(x,\nu). \tag{3.1}$$

The solution of this equation is an exponential decay which describes the decrease of the light intensity as the light beam travels through the absorbing medium.

$$I(x,\nu) = I_0 e^{-\alpha(\nu)x}. \tag{3.2}$$

In absorption spectroscopy a spectral line is commonly characterized by its cross-section of photo-absorption $\sigma(\nu)$ and is defined as

$$\alpha(x,\nu) = N(x)\sigma(\nu), \tag{3.3}$$

where $N(x)$ is the concentration of absorbing particles. To characterize the shape of the absorption line the line-shape function $g(\nu)$ is used.

$$\sigma(\nu) = Sg(\nu), \tag{3.4}$$

where S is the integral absorption coefficient or spectral line intensity, which gives the actual strength of the absorption line. The particular form of the line shape function $g(\nu)$ depends on conditions at which the sample is observed but all forms have to fulfill the normalization condition

$$\int_0^\infty g(\nu) d\nu = 1. \tag{3.5}$$

For analytical use the term *Absorbance* is commonly used and is defined as:

$$A = -\ln\left(\frac{I}{I_0}\right). \tag{3.6}$$

One has to be careful when processing absorbance data since the convention defining it with the use of decadic logarithm is also commonly used. Considering the general solution of the Lambert-Beer law we can write

$$A(\nu) = \alpha(\nu) L. \tag{3.7}$$

3.2 Energy levels population

In a sufficiently large ensemble of identical particles, with internal structure, in thermodynamic equilibrium at temperature T the population of internal energy levels obeys the Maxwell-Boltzman distribution. Probability that a particular particle occupies the energy level with energy E_m that is g_m times degenerated is

$$P(E_m) = \frac{g_m}{Q(T)} e^{-\frac{E_m}{kT}}, \tag{3.8}$$

where *Q(T)* is the partition function corresponding to the internal structure of the particles. It serves as a normalization factor and if an energy levels list is available it can be obtained by explicit summation as

$$Q(T) = \sum_m g_m e^{-\frac{E_m}{kT}}. \tag{3.9}$$

For a precise determination of the partition sum a complete an accurate energy level list is necessary. Such accurate lists are seldom available, but because the lower energy levels of many systems are well known this approach is sufficiently accurate at low temperatures where the contributions of the „unknown“ levels are negligible. When using temperature dependences it is practical to have an analytical expression for the partition function. Usually numerically calculated values at different temperatures are fitted to the following equation

$$\log_{10} Q(T) = \sum_{i=0}^{4} a_i (\log_{10} T)^i. \tag{3.10}$$

Using an energy levels list from [79][94] the partition function of H_3^+ at various temperatures has been calculated. Also partition functions for only para and only ortho states have been calculated. The dependences have been fitted to eq. (3.10) and the corresponding parameters are shown in **Table 3.1**.

3.3 Broadenings

When using optical spectroscopy as a diagnostic tool for monitoring plasma many different processes have to be considered during the evaluation. The broadening of the observed spectral lines is one of the most important. Among others it defines the line-shape function of the observed absorption lines which is of direct consequence for the number density calculation of observed absorbing species. The three most important broadening processes in afterglow plasmas are: life-time broadening, collisional broadening and Doppler broadening. The corresponding line-shape functions are applicable for absorption, emission and stimulated emission.

	$^{n}H_3^+$	$^{p}H_3^+$	$^{o}H_3^+$
Offset [cm^{-1}]	0	64,123	86,9591
a_0	-35,2	1,6701	0,55785
a_1	73,1854	-4,3613	2,84975
a_2	-68,18	8,2473	-6,16722
a_3	37,2205	-7,6655	6,74331
a_4	-12,372	3,66181	-3,91438
a_5	2,3412	-0,84791	1,13664
a_6	-0,1923	0,07643	-0,12745

Table 3.1 Coefficients of the partition function expression using equation (3.10) for all H_3^+ states ($^{n}H_3^+$) and for para and ortho states as separate gasses ($^{p}H_3^+$, $^{o}H_3^+$).

3.3.1 Life-time broadening

To each energy level of a quantum system, a lifetime τ can be assigned. It is the inverse value of the speed at which this particular energy level is depopulated by transitions to all lower states. These transitions can be both radiative and non-radiative. The Fourier transform of an exponentially decaying harmonic function with a time constant τ, the spectrum, has a Lorentzian shape with a full width at half maximum (FWHM) $\Delta\nu = 1/2\pi\tau$. This frequency spread corresponds to an energy uncertainty $\Delta E = h\Delta\nu = h/2\pi\tau$ of energy of the particular quantum state. If we consider a transition between the levels m and n, with corresponding life-times τ_m and τ_n, the energy uncertainty of the this transitions is given by the following equation

$$\Delta E = \Delta E_n + \Delta E_m = \frac{h}{2\pi}\left(\frac{1}{\tau_n} + \frac{1}{\tau_m}\right). \tag{3.11}$$

The corresponding frequency broadening for this transition is called the lifetime-broadening line width and can be calculated as

$$\Delta\nu = \frac{1}{2\pi}\left(\frac{1}{\tau_n} + \frac{1}{\tau_m}\right). \tag{3.12}$$

Lifetime broadening is symmetrical around the central frequency $\nu_{nm} = (E_n - E_m)/h$ and the corresponding line-shape function is a Lorentzian function

$$g(\nu) = \frac{\Delta\nu/2\pi}{(\nu - \nu_{nm})^2 + (\Delta\nu/2)^2}. \tag{3.13}$$

Even though this broadening is present with all transitions, in plasmatic experiments it is often much smaller than other present broadenings and can be neglected in most cases.

3.3.2 Collisional broadening

Collisional broadening of absorption lines is caused by collisions of observed particles. In inelastic collision the energy level is changed when a portion of energy is transferred from or to the colliding particle. This leads to a change in the lifetime of the participating energy levels and influences the line shape of the corresponding spectral lines (see natural life time above).

In elastic collisions no change of the energy level occurs but the collision causes a random change of the wave function phase. This leads to random change of the phase of the emitted field at each collision. The spectrum of such randomly phase shifted radiation has a Lorentzian profile with the half-width:

$$\Delta\nu = \frac{f_{col}}{\pi}, \tag{3.14}$$

where f_{col} is the collision frequency. Collision frequency for H_3^+ in He buffer gas at 10 mbar and 77 K is ~$1{,}1\times10^8 s^{-1}$. This corresponds to a collisional broadening of 36,1 MHz.

3.3.3 Doppler broadening

When a gas particle is moving with respect to the light source (detector) then due to the Doppler effect is the frequency of photons absorbed (emitted) by the moving particle shifted. Because each of the gas particles is moving in a different direction and has a different velocity, each particles line shape function central frequency exhibits a different Doppler shift. The resulting line shape function observed with many particles is an average of line shape functions of all particles. If we assume a Maxwell-Boltzman particle velocity distribution then the average line-shape function, which can be observed, is described by a Gaussian function

$$g(\nu) = \frac{1}{\sqrt{2\pi}\sigma_D}\exp\left[-\frac{(\nu-\nu_0)^2}{2\sigma_D^2}\right], \tag{3.15}$$

where

$$\sigma_D = \frac{1}{\nu_0}\left(\frac{k_b T}{M}\right)^{1/2}, \tag{3.16}$$

T is the particle temperature, *M* is the particle mass. The commonly used full width at half maximum (FWHM) can be obtained by multiplying σ_D with the factor $2(2\ln 2)^{1/2} = 2{,}35$. Kinetic temperature of particles whose absorption lines are Doppler broadened can be calculated from the width of the spectral line as

$$T = \frac{\Delta\nu^2}{\nu_0^2}\frac{M}{4k_b}c^2 \tag{3.17}$$

The Doppler broadened width of an absorption line of the H_3^+ ion around 1381 nm at 77 K temperature is 786 MHz. The above calculated value of 36.1 MHz for the collisional broadening at 10 mbar and at the same temperature shows that at these conditions the Doppler broadening is by far the most prominent broadening mechanism. Therefore the temperature of H_3^+ ions can be calculated from line widths of observed absorption lines.

3.4 Number density determination

For the purpose of measuring the effective recombination rate coefficient of recombination it is necessary to know the number density of recombining particles. For this it is necessary to go beyond the phenomenological Lamber-Beer law (equation 2.1) and consider the absorption process in more detail.

Let us consider a transition between states *m* and *n* with a corresponding Einstein coefficient *B*. The rate of change of particle population in the lower state due to transitions from and to the upper state due to stimulated absorption and emission per unit volume is

$$\frac{dN_m}{dt} = \left(N_n B_{nm} - N_m B_{mn}\right)\rho(\nu)\,g(\nu), \tag{3.18}$$

where N_m and N_n are the densities of particles in the lower state *m* and higher state *n*, respectively, $\rho(\nu)$ is the light energy density determined as $\rho(\nu) = I(\nu)/c$, with $I(\nu)$ being the intensity in W/m^2 of the light with frequency ν. Using the relation between Einstein coefficient of stimulated emission and absorption

$$\frac{B_{mn}}{B_{nm}} = \frac{g_n}{g_m}, \tag{3.19}$$

where g_m and g_n are the degeneration factors of the involved states, we can write

$$\frac{dN_m}{dt} = -\left(1 - \frac{g_m}{g_n}\frac{N_n}{N_m}\right)B_{mn}N_m\,g(\nu)\,\rho(\nu). \tag{3.20}$$

Each of the transition corresponds with an absorption or emission of a photon with energy *hv*. Therefore the change in energy density due to stimulated absorption and emission is

$$\frac{d\rho(\nu)}{dt} = -\left(1 - \frac{g_m}{g_n}\frac{N_n}{N_m}\right) N_m A_{mn} \frac{c^2}{8\pi\nu_0^3} g(\nu) I\nu \,. \tag{3.21}$$

The relation between the Einstein coefficient of spontaneous and stimulated emission was used

$$\frac{A_{nm}}{B_{mn}} = \frac{8\pi h\nu_0^3}{c^3}, \tag{3.22}$$

where is v_0 is the central wavelength of the corresponding transition. Using the speed of light *c* as a conversion factor we can express the energy density loss on the distance traveled instead of time passed

$$\frac{d\rho(\nu)}{dt} = \frac{dI(\nu)}{cdt} = \frac{dI(\nu)}{dx}. \tag{3.23}$$

Now we can write the before mentioned Lambert-Beer law, but with an detailed expression for the absorption coefficient

$$\alpha(\nu) = \left(1 - \frac{g_m}{g_n}\frac{N_n}{N_m}\right) N_m A_{nm} \frac{c^2}{8\pi\nu_0^3} g(\nu)\nu \,. \tag{3.24}$$

If we assume that the upper state is unpopulated then we can write for the absorption coefficient at the central wavelength v_0

$$\alpha_m(\nu_0) = N_m A_{nm} \frac{c^2}{8\pi\nu_0^2} g(\nu_0). \tag{3.25}$$

Since the absorption coefficient $\alpha_m(v_0)$ can be directly measured the number density of particles in the state *m* can be easily calculated from experimental data.

Often the number density of the whole species is desired. To extract this information from measurements of one transition we need to assume a certain distribution of states. For an arbitrary distribution of states we can rewrite the equation (3.24) using equation, (3.3) and (3.4) and integrating through *v* as

$$S = P(m)\left(1 - \frac{P(n)}{P(m)}\right) A_{nm} \frac{c^2}{8\pi\nu_0^2}, \tag{3.26}$$

where *P(m)* and *P(n)* are the probabilities of populating the states *m* and *n* resulting from the selected arbitrary distribution. If the observed system is in a thermal equilibrium the Maxwell-Boltzman distribution, (3.8) can be applied

$$S = \frac{c^2}{8\pi}\frac{g_n}{Q(T)\nu_0^2}\exp\left(\frac{-E_m}{kT}\right)\left[1-\exp\left(\frac{-(E_n-E_m)}{kT}\right)\right]A_{nm} \quad . \tag{3.27}$$

The integral absorption coefficient *S* has the dimension of [cm^{-1}/(molecule×cm^{-2}] in literature it is commonly referred to as the "Hitran" unit [95]. By explicitly expressing the degeneracy factor we obtain

$$S = \frac{C\tilde{g}_n(2J_n+1)}{Q(T)\nu^2}\exp\left(\frac{-E_m}{kT}\right)\left[1-\exp\left(\frac{-\Delta E}{kT}\right)\right]A_{nm}, \tag{3.28}$$

where $\tilde{g}_n$ is the spin degeneracy factor and J_n is the nuclear angular momentum of the state *n*. The constant C is $c^2/8\pi = 1.3266\times10^{-12}$ cms^{-1}.

The calculated integral absorption coefficient can be used to extract number densities of observed absorbing particles. From measurements at peak center of Doppler broadened absorption lines the number density N at temperature *T* can be calculated as

$$N = \frac{A\sqrt{2\pi}\sigma_D(T)}{LS(T)}. \tag{3.29}$$

Temperature [K]	77	145	300
Q(*T*)all	4,81	12,99	37,46
Q(*T*)para	7,82	12,11	25,56
Q(*T*)ortho	12,43	15,45	28,49
(1,0)			
all	$1,84\times10^{-19}$	$1,46\times10^{-19}$	$7,92\times10^{-20}$
ortho	$3,62\times10^{-19}$	$2,91\times10^{-19}$	$1,58\times10^{-19}$
(1,1)			
all	$7,78\times10^{-20}$	$5,05\times10^{-20}$	$2,43\times10^{-20}$
para	$1,59\times10^{-19}$	$1,02\times10^{-19}$	$4,85\times10^{-20}$
(3,3)			
all	$4,07\times10^{-21}$	$2,39\times10^{-20}$	$4,17\times10^{-20}$
ortho	$8,15\times10^{-21}$	$4,81\times10^{-20}$	$8,38\times10^{-20}$

Table 3.2 Calculated integral absorption coefficients used for calculation of H_3^+ number density

3.5 Cavity ring down spectroscopy

Cavity ring-down spectroscopy (CRDS) is a relatively new method compared to the time that absorption spectroscopy has been used as an analytical tool. The basic principle, on which CRDS stands, leakage of light confined in an optical resonator has been known for quite some time. At first it was used to obtain absolute measurements of the reflectivity of high reflectivity mirrors, which were used for laser resonators [96]. The first one to demonstrate the use of optical cavities for trace gas detection were O'Keeffe and Deacon in 1988[97] when they introduced the pulsed version of CRDS. Today high finesse low loss optical cavities are a crucial centerpiece for many scientific and technological advances. Simple direct one-pass absorption spectroscopy can detect absorptions down to a relative change in light intensity of 10^{-3}. Using multi-pass techniques like a Herriott type cell, the sensitivity can be increased to 10^{-5} relative change by increasing the effective absorption path up to 100 m. Further increase in sensitivity can be achieved by applying a proper frequency modulation scheme and lock-in detection. This can increase the sensitivity to roughly 10^{-6}. For further increase in sensitivity indirect methods can be used. (PAS, fluorescence etc.) Although highly sensitive all of the indirect methods suffer from a significant disadvantage, namely that they are not self-calibrating. Reference measurements are needed in order to extract quantitative data. On the other side when using high finesse optical cavities to extend the effective absorption path like in a CRDS or Cavity Enhanced Absorption Spectroscopy (CEAS) one can without extreme effort reach sensitivities of 10^{-7} cm^{-1}. With careful design and alignment the sensitivity of a CRDS setup can be extended to ~10^{-10} cm^{-1}. Today, absorption spectroscopy techniques utilizing optical cavities and particular modulation techniques can reach sensitivities of 10^{-13}[98]. These values are only a few times above the corresponding shoot noise limit given by the finite number of photons in the probing laser beam [98].

3.5.1 Pulsed CRDS

The first demonstration of CRDS ability to detect absorption was performed using a pulsed laser. Pulsed CRDS is the best experimental arrangement to explain the basic principles of CRDS.

Consider a stable optical resonator of length d that is made of high reflectivity mirrors with reflectivity R~1. For a schematic representation of this arrangement see **Figure 3.2**. Now consider a pulsed laser as the light source. The pulses are fired along the optical axis of the resonator. In order to avoid interference effects let us assume that the pulse length T_{pulse} is significantly shorter than the round trip time τ_R of the pulse inside the optical cavity

$$T_{pulse} < \tau_R = \frac{d}{c}. \tag{3.30}$$

Upon the impact of the laser pulse on the first mirror, of the resonator, small fraction of the light is transmitted through the mirror. When scattering losses in the mirror substrate and coating are neglected then the transmitted fraction is $T = 1\text{-}R$. This transmitted light is then effectively confined inside of the optical resonator since it suffers only very low losses ~($1\text{-}R$) in reflections on both mirrors. These small losses due to transmission upon each reflection can be detected. The first pulse transmitted also through the detector side mirror is attenuated by a factor of T^2 compared to the incident beam. Typically mirrors with $T\sim10^{-4}$ and less are used (R~0,9999). To detect the small fraction (~10^{-8}) of the incident pulse the detector used for pulsed CRDS has to be very sensitive. Typically photo-multiplier tubes are used. The transmitted pulse is also further attenuated by absorption along its path inside the resonator. Light intensity after one trip through the resonator is decreased by photo-absorption according to Lambert-Beer law by the factor

$$\exp\left(-\int_0^L \sigma(\nu)N(x)dx\right), \tag{3.31}$$

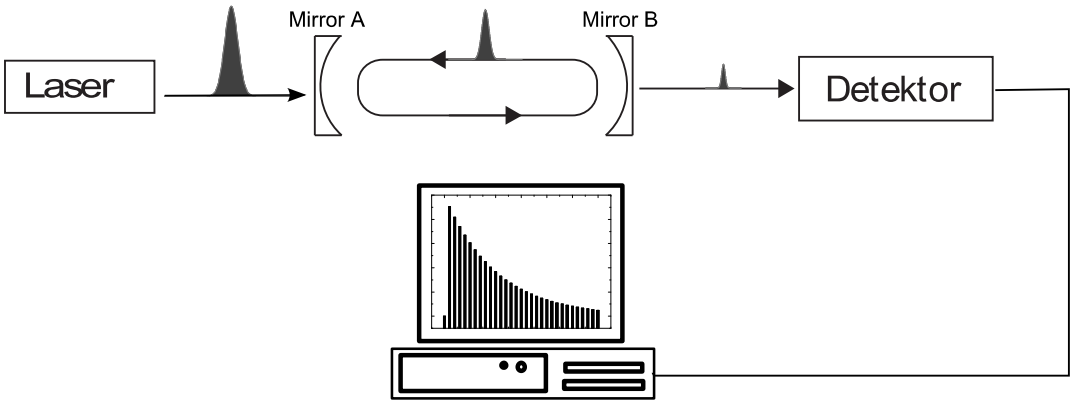

Figure 3.2 Schematic representations of pulsed Cavity Ring-down Spectroscopy set up. Small transmited fraction of incoming laser puls is confined in an optical cavity. The exponential decay of the confined pulse via leakage through the mirrors of the cavity is monitored**.**

where $\sigma(\nu)$ is the frequency dependent cross-section of photo-absorption, L is the path length trough the absorbing medium. The intensity of light after n reflections $I(n,\nu)$ inside the optical resonator inside will be

$$I(n,\nu) = I_0(\nu)\,R(\nu)^{2n} e^{-2n\sum_j \sigma_j(\nu)\int_0^L N_j(x)dx}, \tag{3.32}$$

where I_0 is the light intensity transmitted from the initial light pulse at the beginning of the way through the resonator. The sum in the exponent represents the fact that at the frequency v many absorbing species can be present inside the resonator. The sum is through all of them. Expressing the number of the roundtrip n inside the cavity with the corresponding time according to $t = \tau_R n = 2dn/c$

$$I(t,\nu) = I_0(\nu)\exp\left[t\frac{c}{d}\left(\ln R(\nu) - \sum_j \sigma_j(\nu)\int_0^L N_j(x)dx \right)\right]. \tag{3.33}$$

This can be rewritten as

$$I_\nu(t) = I_0 e^{-\frac{t}{\tau(\nu)}}, \tag{3.34}$$

where $\tau_R(\nu)$ is

$$\tau(\nu) = -\frac{d}{c\left[\ln(R(\nu)) - \sum_j \sigma_j(\nu)\int_0^L N_j(x)dx \right]}. \tag{3.35}$$

Expression (3.35) can be simplified by introducing $\tau_0(\nu)$ the time constant of light decay of an empty cavity the so called baseline

$$\tau_0(\nu) = \frac{d}{c}\frac{1}{ln\left(R(\nu)\right)} \tag{3.36}$$

and $A(\nu)$ the overall absorption inside the optical cavity caused by all present absorbing species

$$A(\nu) = \sum_j \sigma_j(\nu)\int_0^L N_j(x)dx. \tag{3.37}$$

With this the equation (3.35) rewritten as

$$\frac{1}{\tau(\nu)} = \frac{1}{\tau_0} + \frac{c}{d}A(\nu). \tag{3.38}$$

From this we can write

$$A(\nu) = \frac{d}{c}\left[\frac{1}{\tau(\nu)} - \frac{1}{\tau_0} \right]. \tag{3.39}$$

Using this equation the frequency dependent absorption *A(v)* can easily be calculate when the decay times of the light pulses trapped inside the optical resonator are measured both for the empty cavity and cavity filled with the absorbing species. From equation (3.39) the greatest advantage of CRDS is also clearly visible. The obtained absorption coefficients from decay times do not depend on the intensity of the laser used and sensitivity of the detector, as long as it is linear. CRDS is an absolute absorption spectroscopy method.

3.5.2 Continuous wave CRDS

Although pulsed CRDS is a very simple method, it has several major drawbacks. High powered lasers and sensitive photo-detectors are required in order to be able to observe ring-down decays. High power lasers are often bulky and quite expensive with high maintenance and operation cost. Frequently they also have poor wavelength stability. But the main disadvantage of pulsed laser is the broad laser-line bandwidth that makes Doppler-limited or sub-Doppler high-resolution spectroscopy hard or even impossible to do in this setup. Although recently CRDS with ultra-short pulses, frequency combs, has been demonstrated [99] that offers among other advantages Doppler-limited resolution.

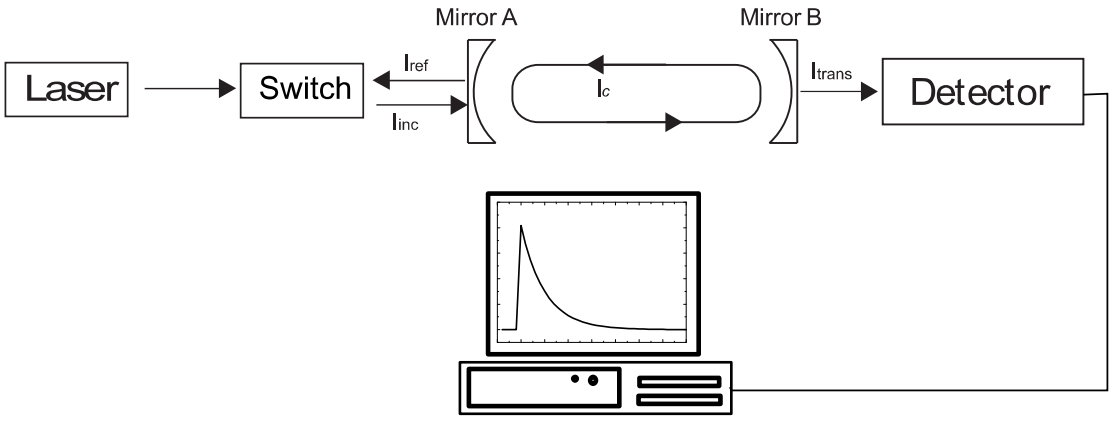

Figure 3.3 Schematic representation of the continuous wave Cavity ring-down spectroscopy technique setup.

In continuous wave CRDS (cw-CRDS) basically all of the disadvantages of pulsed CRDS are eliminated at the cost of a little more complex optical setup. Using continuous single frequency tunable lasers that have line-widths in the range from 1 kHz to 10 MHz, sub-Doppler spectroscopy is easily achieved. In continuous wave CRDS the injection of light exploits the interference effects that one tries to avoid in pulsed CRDS and multi-pass techniques. The injection of light exploits the resonant structure of the optical cavity to achieve a high effective transmission of laser light into the cavity so sufficiently high signal levels are observed even with low power

lasers (<1 mW) and ordinary detectors (PIN diodes or avalanche photo diodes). This allows the use of low power diode lasers with this technique that have excellent operational characteristics, stability and are low cost nowadays. This particular modification of CRDS has been first demonstrated be *Romanini at al*. [100] using a continuous single frequency dye laser. The basic setup of cw-CRDS is schematically depicted in **Figure 3.3**.

As the full explanation of the resonant build up inside of optical cavities exceeds the scope of this work, only very basic concepts and results necessary for a good understanding of this method will be presented here. Please refer to the original work of *Romanini* and *Lehman* [101] and a detailed study from *Morville* [102] for a detailed analysis.

The shape of the optical transfer function of a stable optical cavity is quite similar to the transfer function of a simple Fabry-Perot cavity with equally spaced resonance peaks. The intensity of transmitted light (see **Figure 3.4**) has the following form

$$I(\lambda) = I_0 \frac{(1-R)^2}{(1-R)^2 - 4R\sin^2\left(\frac{2\pi L}{\lambda}\right)}. \tag{3.40}$$

From this one can see that for certain wavelengths of incident light and resonator dimensions the full intensity is transmitted through the resonator regardless of mirror reflectivity. For each peak in the transmittance of the resonator a standing wave pattern is formed inside of the resonator that fulfils the condition $L = n\lambda/2$ a so called mode of the resonator. The mode separation distance is called the *free spectral range* (FSR) and its value in hertz can be calculated as

$$FSR = \frac{c}{2L}. \tag{3.41}$$

For a resonator with mirrors placed 15 cm apart is the FSR equal to 1 GHz. The full width at half maximum of the resonance peaks depends on the mirror reflectivity and mirror separation as

$$\Delta\nu_{1/2} = \frac{c(1-R)}{2\pi L\sqrt{R}}, \tag{3.42}$$

where R is the mirror reflectivity, τ_R is the round trip time of the cavity. For a cavity with 15 cm mirror separation and $R_a = R_b = 0{,}9999$ the resonance peak width is 32 kHz. Commonly a parameter called *Finesse* (F) is used to characterize an optical cavity

$$F = \frac{FSR}{\Delta\nu_{1/2}} = \frac{\pi\sqrt{R}}{(1-R)}. \tag{3.43}$$

Since for real applications the planar mirrors and divergent laser beams do not produce a stable resonator this approach can not be used for CRDS. Stable resonator configuration is necessary. In a stable optical resonator the laser beam trapped inside is after a few reflections reflected perfectly upon it self, when losses due to finite dimensions are neglected. A stable resonator is easily achieved with spherical mirrors that fulfill the following condition

$$0 \le \left(1-\frac{L}{r_a}\right)\left(1-\frac{L}{r_b}\right) \le 1, \tag{3.44}$$

where r_a and r_b is the radius of curvature of mirror *a* and *b*, respectively. The mode structure of such resonators is more complex when compared to the simple planar case mentioned beforehand. The transversal modes of resonators composed of spherical mirrors are labeled with *m* and *n* and commonly referred to as TEM_{mn} modes. The transversal profiles of few first TEM modes are shown in **Figure 3.5**. The formulas stated above for the planar Fabry-Perot resonator also hold for the TEM_{00} mode. For higher order modes ($m, n > 0$) the same qualitative results apply as for the TEM_{00} mode but the formulas for particular numerical values have a different form. For a detailed description of resonator mode structures see reference [103].

The continuous wave CRDS setup exploits this resonant mode structure of a stable optical cavity composed of two spherical mirrors. If the incoming lasers spatial characteristics coincide with one the eigen-modes of the optical cavity and the laser wavelength coincides with one of the longitudinal modes then the mirrors become effectively transparent and an intensity build-up takes place inside the optical cavity. This build up can be observed on the detector behind one of the cavity mirrors. When a predefined signal level is reached the incoming laser is turned of with a suitable mechanism. After the laser has been shut-off an exponential decay (ring-down) of light intensity is observed. It is necessary that the laser turn-of time be fast compared to the ring-down time of the cavity. Usually an *acousto-optical modulator* (AOM) or an electro-optical modulator (EOM) is used to achieve the needed short turn off times. Since the ring-down time of the optical cavity is mode dependent, with the longest time associated with the TEM_{00} mode, spatial filtering and mode-matching optics are used to facilitate effective coupling into the TEM_{00} mode. It can be shown that for the TEM_{00} mode the relation between ring-down time and absorption is the same as in pulsed CRDS . The frequency overlap with one of the longitudinal modes can be achieved either by scanning the laser frequency or by modulating the cavity length. For the particular realization of cw-CRDS used in this work see **Chapter 5**.

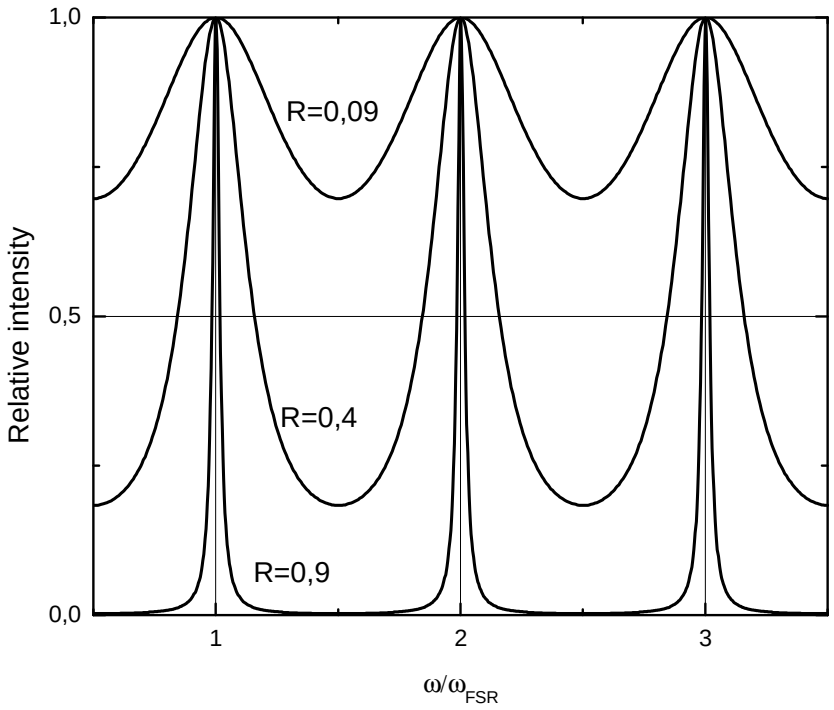

Figure 3.4 Transfer function of an ideal planar Fabry-Perot resonator calculated using (3.40.)

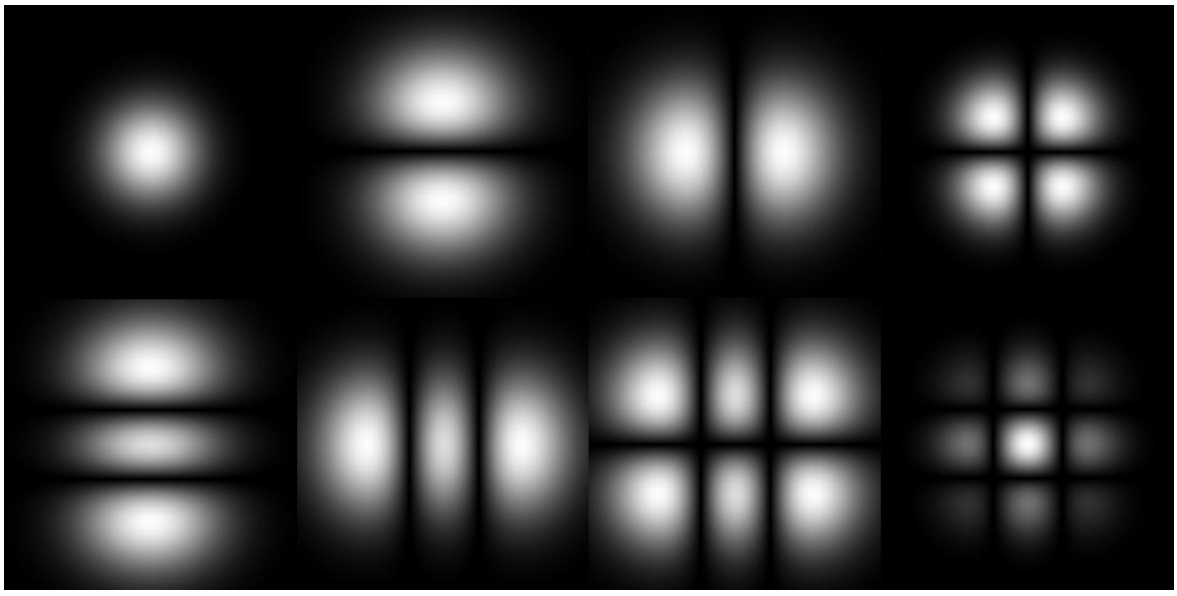

Figure 3.5 The first few Transverse Electrecal Modes(TEM) of a stable optical resonator with spherical mirrors. From left to right: *upper row* TEM_{00},TEM_{01},TEM_{10},TEM_{11}, *lower row* TEM_{02}, TEM_{20}, TEM_{21}, TEM_{22}

3.5.3 Coupling efficiency

The matter of efficient coupling of a Gaussian laser beam into an optical cavity is of crucial importance for many technologies in use today and for continuous wave CRDS. The matter has been studied extensively. Important results and consequences can be found in literature [102] that can significantly aid in the use of a cw-CRDS setup. The interested leader is strongly advised to look into the given references. Especially figures 2.4 and 2.5 of the dissertation thesis of *J. Morville* [102] that summarizes among other the coupling coefficients into a range of resonator modes in different suboptimal situations. Such as laser beam waist different from the resonator waist, misalignment of the laser beam with respect to the resonator axis, etc.

The dependence of the coupling coefficients on the spectral laser line-width, cavity finesse and cavity sweep speed were published by *Jae Won Hahn* et al. [104].

4 Experimental apparatus

The main diagnostic technique used in this work is cavity ring down spectroscopy in the continuous wave modification (cw-CRDS). The used experimental apparatus can be divided into four parts. First it is the optical system of the CRD spectrometer, second is the gas handling and microwave system, third is the acquisition and control electronics and fourth is the so-called “para-generator”, used to produce H_2 with enriched populations of para states. Each of this parts will be described in a separate section.

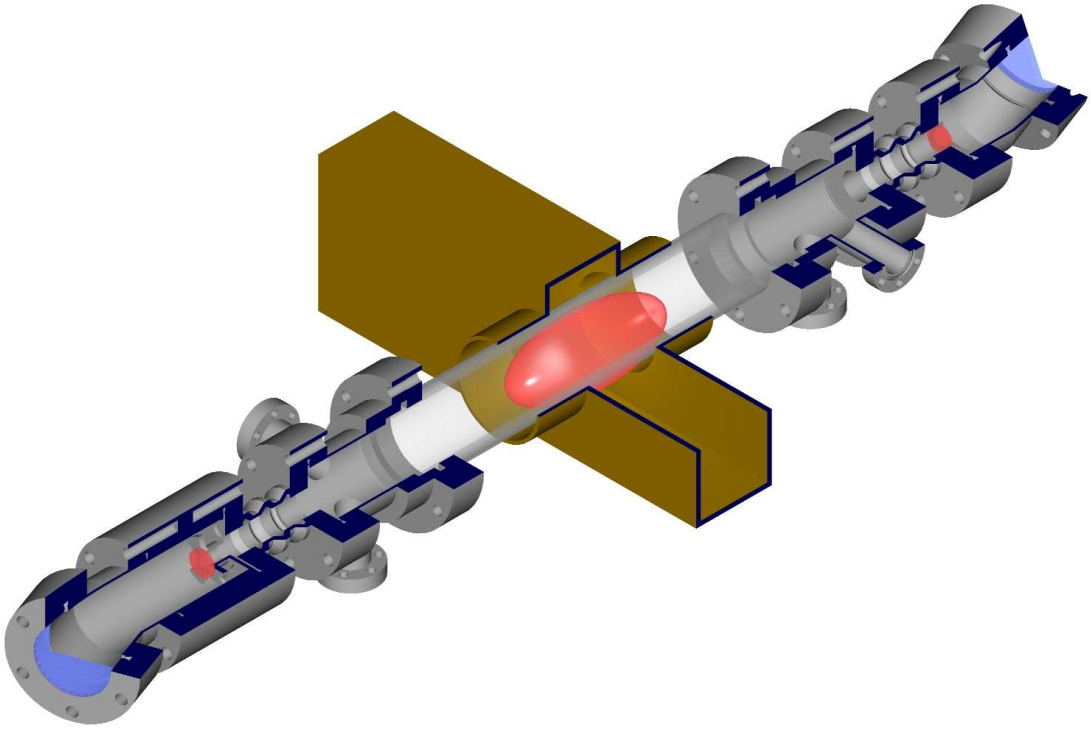

Figure 4.1 Schematic 3D view of the optical resonator inside the vacuum vessel. Entrance and exit windows are tapered to prevent the creation of parasitic resonators along the optical path that would interfere with the measurement. Middle part depicts a microwave discharge inside the discharge tube.

4.1 CRD spectrometer

First demonstration of the particular configuration of CRDS used in the present work was by *Romanini et al*. [100]. Details and theoretical background of this technique were presented in **Chapter 3**. The cavity ring down spectrometer used during presented studies was built in our laboratory to allow for spectroscopic time

resolved studies of elementary processes in plasma such as ion-electron recombination. The primary purpose is to validate results obtained with different experimental techniques that lack the ability to observe particular ion species and their internal excitation. Only brief descriptions were presented in our journal publications mostly due to space constraints (e.g. see attached publications), therefore in this work a more thorough and detailed description will be presented.

4.1.1 Optical cavity

The optical cavity of the spectrometer consists of two spherical high reflectivity dielectric mirrors spaced 75 cm apart. The mirrors are ½ inch in diameter and have a radius of curvature of 1 m. They are positioned so that they form a stable optical cavity [103]. Due to the numerous roundtrips of trapped photons, any optical surface inside the optical cavity would significantly increase the losses and hence decrease sensitivity. Therefore, mirrors are placed inside the vacuum vessel to minimize losses from transitions through additional surfaces. Placing the mirrors outside the containment vessel is commonly used only with aggressive substances mostly in the liquid phase [105]. Still some reflection minimizing techniques have to be used such as Brewster angle placement. For these cases the loss of sensitivity is somewhat countered by the high number density of the absorbing species. Nevertheless much faster acquisition electronics (up to 1GHz) has to be used in those experiments to reliably measure RD transients that have decay times on the order of

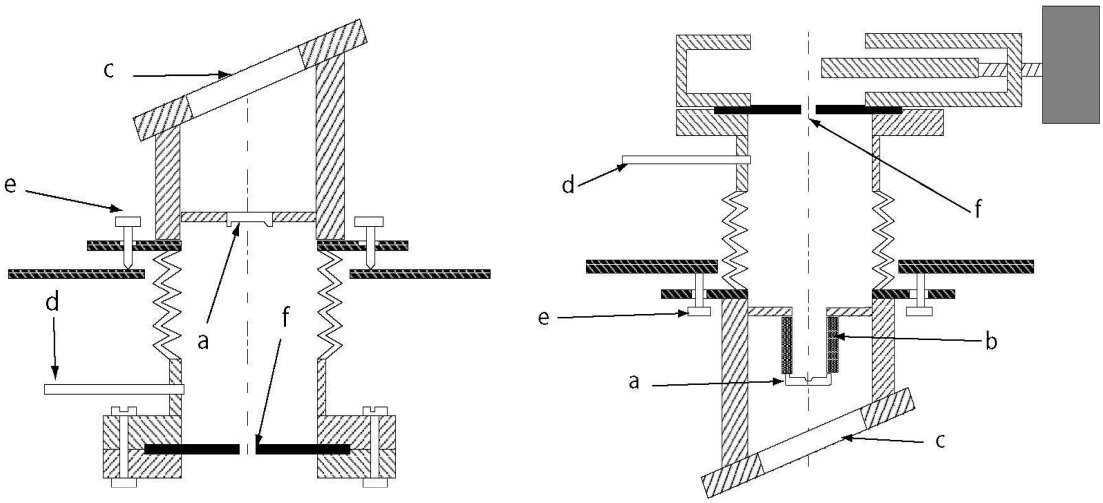

Figure 4.2: Cross section of the exit (left) and entry (right) resonator mirror holders. a) mirror; b)piezoelectric tube; c)entrance and exit window; d) gas entry port; e) micro-turn adjust screws; f) aperture

few ns. In our setup one of the mirrors is placed on a cylindrical piezoelectric element that is used to vary the length of the optical resonator. Mirror holders in our setup are connected to the rest of the vacuum system via flexible bellows and are equipped with micro turn screws to allow for fine adjustment of the optical cavity. Schematic 3D view of the optical cavity inside the vacuum vessel is depicted in **Figure 4.1** schematic cross-sections of the mirror holders are in **Figure 4.2** .

Manufacturer of the mirrors claims a reflectivity of more then 99.98%. From the maximal obtained ring down time of 33 μs and the equation (3.35) one can calculate that the reflectivity in the observed spectral region is ~99,9925%. The observed ring down time of 33 μs is also the life-time of photons inside the optical resonator. This corresponds to an effective absorption path of roughly 9 km. $L_{\text{eff}} = L/(1- R)$ [106]. According to equation (3.40) and (3.41), the free spectral range of this optical cavity is FSR~200 MHz and the full width at half maximum of the resonance is ~5,1 kHz. Compared to our previous studies where the optical cavity was oriented vertical the optical cavity was now placed horizontally. This drastically reduced the probability of dust particles falling on the cavity mirrors during the experiment. Consequently, the significantly prolonged periods between breaching of the vacuum vessel for mirror cleaning resulted in a lower achievable rest gas pressure and impurity content.

4.1.2 Light source

As the light source, a fiber-coupled commercial distributed feedback (DFB) laser diode from NTT Electronics Inc. in a 14-pin butterfly package was used. Central wavelength of the laser is 1381.55 nm. The line-width of the laser is <2 MHz at 1 second timescales. Maximum output optical power is 20 mW. DFB lasers have a wavelength selective element (Bragg grating) integrated directly in the laser resonator. By changing the temperature of the laser resonator the Bragg grating thermally expands or shrinks, thereby changing the feedback wavelength. Temperature control is facilitated with an integrated thermoelectric cooling (TEC) element. Very stabile and precise temperature stabilization and control is therefore necessary for good stability and wavelength tuning. Temperature control and laser current is provided by a Thorlabs ITC502 laser diode controller. The controller is fully operated remotely via GPIB from the control computer. The lasing wavelength can also be adjusted with the laser diode forward current flowing through the diode. Generally current tuning is much faster than temperature tuning but has a limited tuning range, compared to temperature control. Current tuning is therefore predominantly used in experimental setups where continuous coupling to an external cavity is employed [107]. The tuning range ±3 nm of a DFB laser diode is quite small, the central wavelength was therefore specially selected so all the transitions required for the experiment fall inside the tuning range (see chapter 5). The biggest

advantage of DFB laser diodes is their mode-hop free tuning behavior over the whole tuning range. Although external cavity lasers with much narrower laser line-width (300 kHz) offer an increased coupling efficiency into the optical cavity, their lower achievable power and operational bulkiness would negate the line-width advantage. Therefore, they were not used even though they are available in our laboratory.

The laser light exiting the diode is fiber-coupled, within the lasers package, into a single mode optical fiber ending with an FC-APC. The angled FC connector minimizes back reflections and the corresponding etaloning effects. Next, two 95:5 fiber beam splitters are used to obtain two laser beams used for wavelength and wavelength change determination using the Wavementer and Fabry-Perrot etalon (see bellow for description).

4.1.3 Laser beam manipulation setup

To achieve the required beam shape, for efficient coupling into the optical cavity, and to facilitate beam switching, required for observing clean ring down transients, a relatively simple optical setup has to be employed. Schematic top view of the beam manipulation optical setup is shown in the **Figure 4.3**.

The output laser beam from the optical fiber is collimated using an antireflection-coated aspheric lens. The diode laser is very sensitive to back-reflections that can cause a shift in the lasing wavelength or broaden the laser line-width and thus decreasing the precision of measurements. To minimize back-reflections an optical isolator is employed. This allows for a ~2000 fold decrease in intensity of back-reflections that could be potentially coupled into the laser resonator via the collimation optics.

The next active component along the beam path is the *acousto-optic modulator* (AOM) that is used for beam switching; . The CRDS apparatus has received minor upgrades over previously reported realizations that improve the overall performance of the system. One of those is a beam-shrinking telescope, placed prior to the AOM that increases the fraction of the laser beam passing through the active region of the AOM. The laser collimator used produces a beam that has a waist of roughly 3 mm, at the distance where the AOM is placed, whereas the AOM active region diameter is only approximately 1 mm. By using a Keppler type telescope consisting of lenses with focal lengths of f1 =100 mm and f2= 15 mm the beam is shrunk f1/f2 ~ 6,6 times. Because the focal length of the lenses is given for light with 650 nm, the shrinking ratio is calculated only approximately. The transmitted intensities of the laser beam before and after the AOM were measured with a Power meter (Thorlabs PM100) allowing for quantization of the improvement. Using the setup with the shrinking telescope, 95% of the incident laser intensity was transmitted through the AOM.

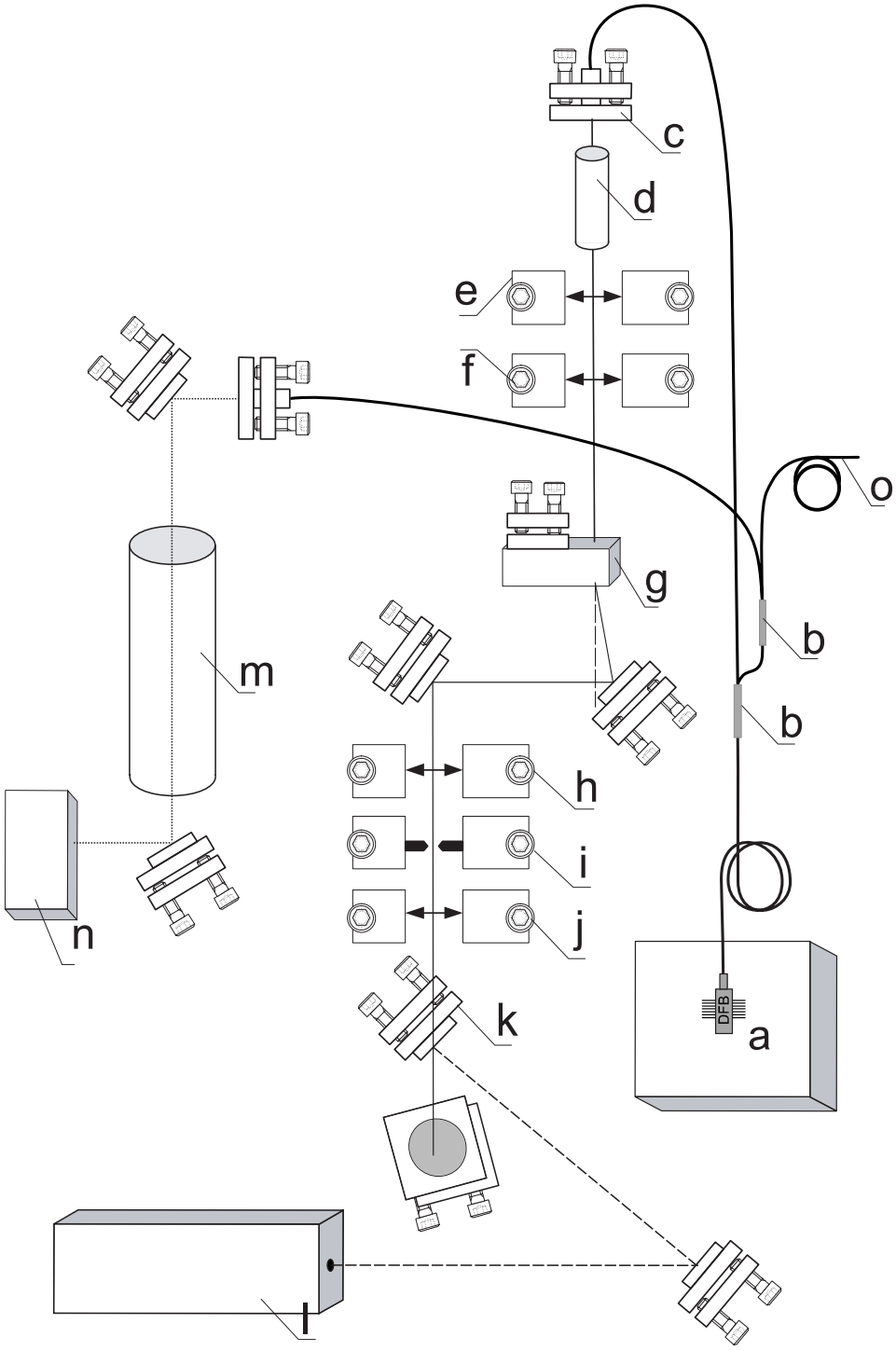

Figure 4.3: Top view of the optical components placement. Optical fiber from the DFB laser (a) is connected to two 95:5 fiber beam splitters (b). The main fraction of the laser exits the fiber via the collimator (c). The optical isolator (d) follows. The beam shrinking telescope from lenses (e) and (f) focuses the beam on the active region of the acousto-optical modulator (g). The beam is focused on the pinhole (i) by the lens (h) and mode matched with lens (j). The HeNe guiding laser (l) and Fabry-Perrot (m) resonator are also placed on the optical breadboard.

This is an improvement over the 80% transmittance achieved without the beam-shrinking telescope. Additionally, better focusing onto the active region resulted in a less distorted laser beam after the AOM. When using higher power lasers for the experiment, care has to be taken not to exceed the upper limit of the allowed incident power density inside the AOM crystal (500 mW/mm^2) to avoid damage to the AOM. With proper adjustment of the AOM placement and orientation, ~80% of the transmitted intensity is channeled into the first diffraction maximum of the AOM and can be used further. A short description of the adjustment process of the AOM is presented in Appendix A.

After two adjust mirrors the spatial filtering and mode matching components are placed. First one lens with f=50.2 mm (at 1550nm) focuses the incoming laser beam on a small aperture (50 μm), commonly referred to as a pinhole. The first lens performs a Fourier transformation of the incoming laser beam. The pinhole, placed in the focal plane of the lens, effectively stops all higher spatial frequencies present in the incoming beam from propagating further. A high quality clean Gaussian beam is necessary for single TEM00 mode excitation of the ring-down cavity in that it significantly lowers the excitation rates of higher order modes of the ring-down cavity thus improving the achievable sensitivity of the whole apparatus. The beam after the pinhole has a pseudo-Gaussian profile due to the diffraction contribution from passing through the pinhole. However, the divergence from a pure Gaussian beam profile can be in praxis neglected. Using a pinhole spatial filter has also another advantage as *Romanini* [108] states, the walk-off or directional instability (pointing instability) of the laser is converted to intensity fluctuations, which CRDS is "immune" to, but excitation remains mode selective. The beam from the pinhole can be easily mode matched, using another lens, to the cavity mode TEM00 by setting the proper pinhole-lens-cavity distance. In previous realization of the spectrometer, the setup did not account for the dependence of the spatial filtering lens focal length on the wavelength and divergence of the incoming laser beam. The lens-pinhole distance was held constant and this caused a significant loss of intensity on the pinhole, since the lens-pinhole distance could not be precisely measured nor set. In the current realization, this has been overcome by placing the spatial filtering pinhole on a linear translation stage. Now, using a simple iterative adjustment process, utilizing this translational stage, the transmission of the spatial filtering subsection was increased from ~70% before to more than ~95% now. For details of the tuning procedure, see Appendix A. All mentioned optical components reside on a rigid optical breadboard that lies under the ring-down cavity. After mode matching is the laser directed upwards and then again leveled on axis of the RD cavity. The optical setup in the present implementation is passively vibration isolated by a 10 cm thick Styrofoam panel. This reduces dynamic deformations of the ring-down cavity (i.e. fluctuations of the ring-down time) caused by ground vibrations.

To aid guiding of the IR beam invisible to the naked eye a visible HeNe laser is used. It is brought on the same path as the IR laser using a flip-flop mirror mount after the mode matching lens.

4.2 Detection and Control electronics

4.2.1 Detector

The ring-down signal exiting the optical cavity is detected by an InGaAs avalanche photodiode (APD) (type C30645E from PerkinElmer) that is used in combination with a homebuilt trans-impedance amplifier. The APD is operated with a floating bias voltage of approximately –45 V (breakdown at -49,1 V). To increase the detection efficiency the light exiting the RD cavity is focused using a single lens on the 50 μm active area of the APD. The detector is placed on a XYZ movable mount for adjustment.

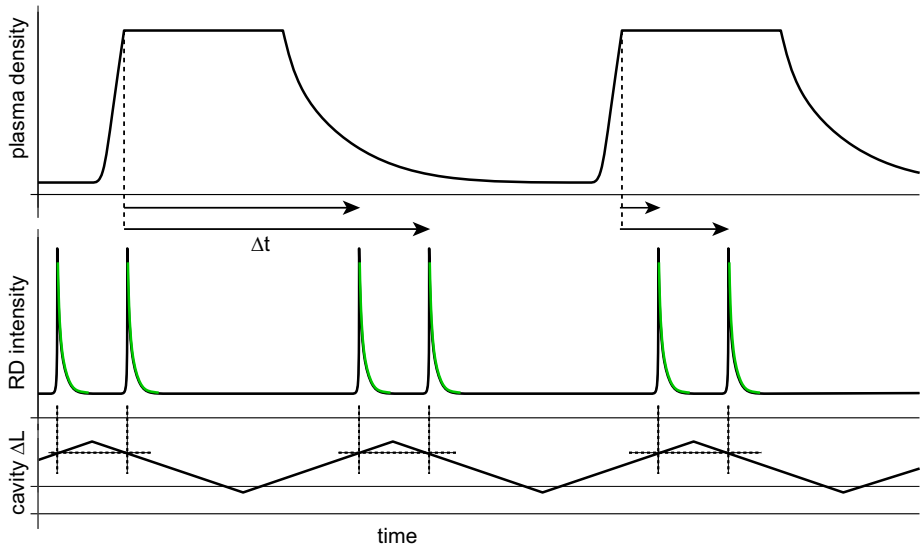

Figure 4.4 The timing scheme of the time resolved CRDS. The resonant cavity intensity build-ups are triggered by sweeping the cavity length. Cavity length modulation is not correlated to the discharge cycle but for each RD event the time in respect to the current discharge cycle is recorded. Reprinted from [66]

A short note on the detector amplifier is in place here. The resistance of the feedback resistor of the trans-impedance amplifier should be as high as possible. Generally the thermal noise generated by a resistor rises as the square root of its resistance, so high resistances should be avoided in precision circuits due to high thermal noise. The signal in a trans-impedance amplifier rises linearly with the resistance of the feedback resistor. Therefore in a transimpedance amplifier the

signal to noise (SNR) ratio rises with the square root of the feedback resistance. For the best SNR the biggest available resistance is to be used. The limit for the feedback resistor is the input impedance of the operational amplifier used. The resistors value should be sufficiently small when compared to the input impedance of the operational amplifier used.

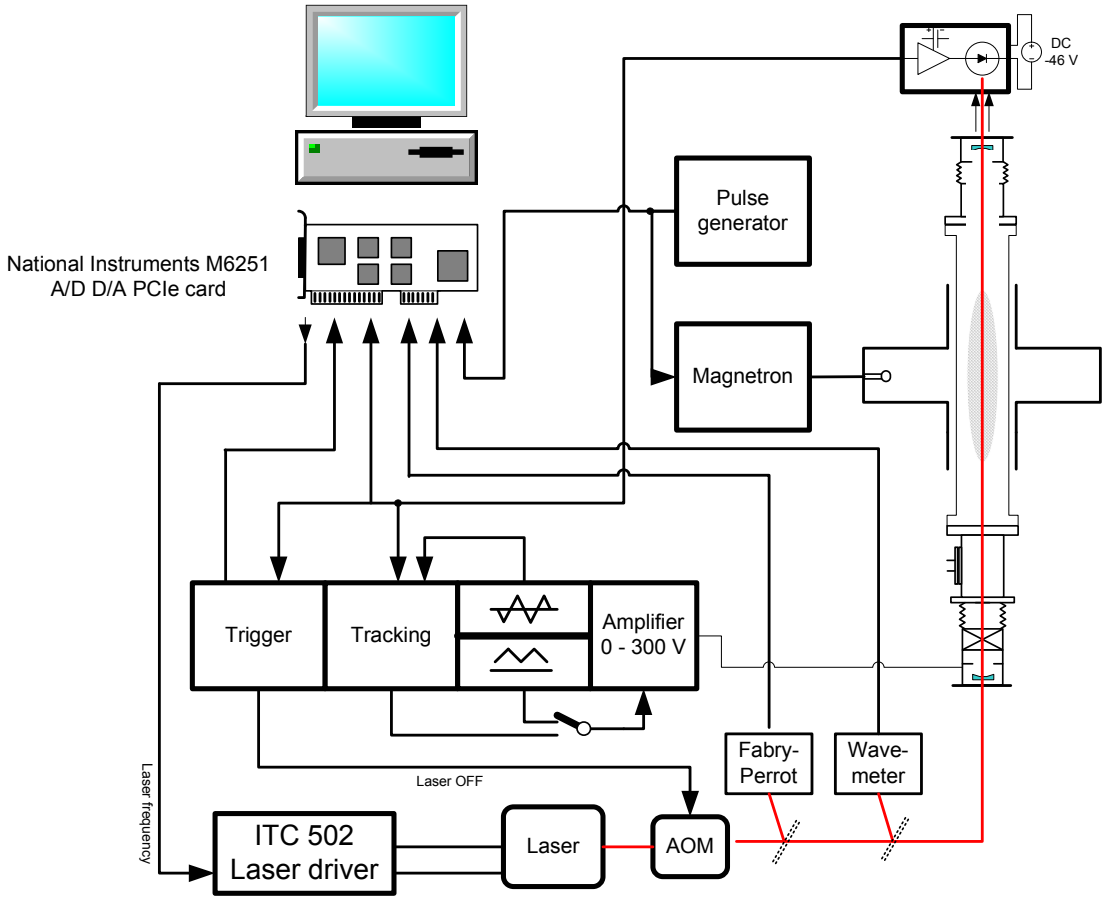

Figure 4.5 Schematic representation of the control electronics of the used CRD spectrometer.

4.2.2 Control electronics and Data Acquisition

To assure highest speed and reliability the core control mechanisms of the experimental apparatus are hardware implemented whereas the data acquisition is performed with a National Instruments M6251 AD/DA lab-card. Although this approach lacks the flexibility of solutions based on general-purpose AD/DA cards combined with control software, it is much more stabile, reliable and less complex (and cheaper). The electronic circuit controls the threshold detection, laser switching, signaling of RD event star/end and the cavity length modulation via the piezo-

electric transducer in one of the mirror holders. The integrated lab-card sampling clock is used to make the whole apparatus time aware. Schematic representation of the control electronics with corresponding data flows is shown in Figure 4.5

The voltage from the detector is fed to the AD/DA lab-card and in parallel to the control electronics. The lab card continuously samples the detector signal at 1 MHz sampling rate and 16-bit resolution as a digital waveform. During a ring-down event the signal on the detector sharply rises. When a predefined voltage level is reached, the control electronics triggers a signal to switch off the laser (using the AOM) for a set amount of time. After the laser is turned off a short delay is necessary for transient effects to subside. After this, the control electronics waits until the RD signal drops bellow a second predefined voltage level to generate a data acquisition signal. This signal holds for a set amount of time. In all of here presented experiments, it was 400 μs of the RD decay. Since the maximum decay time of ring-down events is33 μs, the 400 μs period is long enough to enable proper numerical fitting of the obtained data. After the acquisition period the data acquisition signal is turned off until the next RD event.

It is worth noting that the acquisition timing of a single RD events should as stable as possible. During a malfunction of the acquisition electronics the start data acquisition signal has been started at varying voltages. Data for **Figure 4.16** were recorded during such a malfunction. It is evident that this leads to a significant sensitivity reduction of the spectrometer.

In pulsed, time resolved measurements, the timing of the discharge pulses was controlled by an external signal (pulse) generator with no synchronization to the rest of the control electronics. The logical information about the discharge state was also routed to the PC lab-card where it is also continuously acquired as a digital waveform. During the experiment three signals are continuously sampled, the analog RD detector signal, the digital data acquisition signal and discharge signal. The continuous signal sampling is performed by a double-buffered DMA transfer. The acquired signals are real time preprocessed. Using the data acquisition signal only the detector data belonging to an actual RD event are recorded as signaled by the control electronics. The discharge state signal is used as a time reference. The data acquisition and control software is described in detail in [109]. Stored raw experimental data are later processed via an application that numerically fits the particular RD decays and stores the results in plain text format. These are later processed via specialized routines written in the OriginLab® environment.

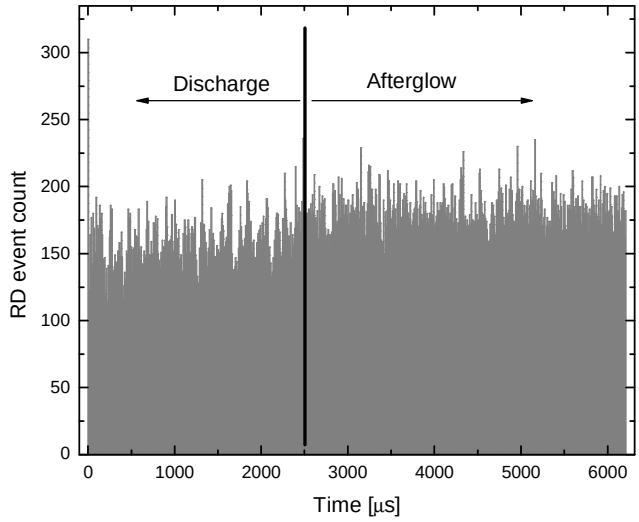

Figure 4.6 Example Histogram of observed RD event distribution during a discharge after many cycles at a fixed wavelength. Total amount of RD events is ~150 000, bin size is 7 μs. Average number of RD events per bin is 169. High count at time 0 is due to RF switching interference.

Separately the control electronics also handles the optical cavity length necessary for the frequent occurrence of RD events. In the standard mode a triangular signal is applied to the piezo-electrical transducer on which one of the cavity mirrors resides. The applied voltage range is high enough that the cavity mirror excursion in each direction is grater than the FSR of the cavity. This way it is ensured that for each cycle the cavity can be in resonance twice. This mode of operation is helpful when tuning the apparatus (see Appendix A). But on the other side in this approach, the optical cavity is in resonance only for a short while and spends most of the time off-resonance (see **Figure 4.4**). The number of RD events observed is at most equal to double the sweep frequency. Since there is a limit on how fast the mirror can move without damage and the coupling efficiency into the cavity decreases with faster mirror movements the achievable RD event frequency is limited to roughly 100 RD per second. This can be dramatically improved by using the so-called tracking mechanism. The cavity length undergoes only minor excursion (compared to the FSR) from a middle position. This middle position is slowly swept across the FSR of the cavity until the point a RD event occurs. The middle position stays in place where minor periodic excursions of the cavity length cause RD resonances. Due to random mechanical and thermal fluctuations combined with small mirror excursions, RD events do not occur in some cycles. But because of the lower excursion much higher repetition frequencies can be used. In the presented implementation RD rates of well over 400 Hz were commonly achieved.

4.2.3 Time resolved detection

Due to the stochastic occurrence of RD events in cw-CRDS the classical time resolved schemes such as pump-probe or laser pulse synchronization, can not be used. The time each of the RD takes place is recorded with respect to the discharge cycle. RD events are only recorded with respect to the discharge cycle but are not

synchronized with it in any way. After a sufficient number of discharge cycles the whole time axis of the discharge is covered with evenly distributed RD events (see **Figure 4.6**). This allows for time resolved processing of the experimental data. Using this apparatus and data processing features, evolutions of absorption during the discharge cycle can be obtained. Combined with the wavelength tuning of the laser diode evolution of absorption line profiles can be obtained thus enabling the determination of the kinetic temperature and its evolution during the discharge cycle from Doppler broadening of the observed lines. Absorptions can be subsequently recalculated to concentrations. When performing time resolved measurements of fast decaying species the problem of baseline determination can be elegantly solved. The absorption observed at the far afterglow when the short lived species have already decayed can be taken as the baseline value of absorption for the empty cavity. Commonly is this ability is referred to as *Synchronous detection* because both the signal and baseline are recorded simultaneously. The long term drifts of the apparatus are circumvented by this approach. With long-lived and neutral species, the baseline value has to be determined by interpolating the off-line background values (see **Figure 4.7**).

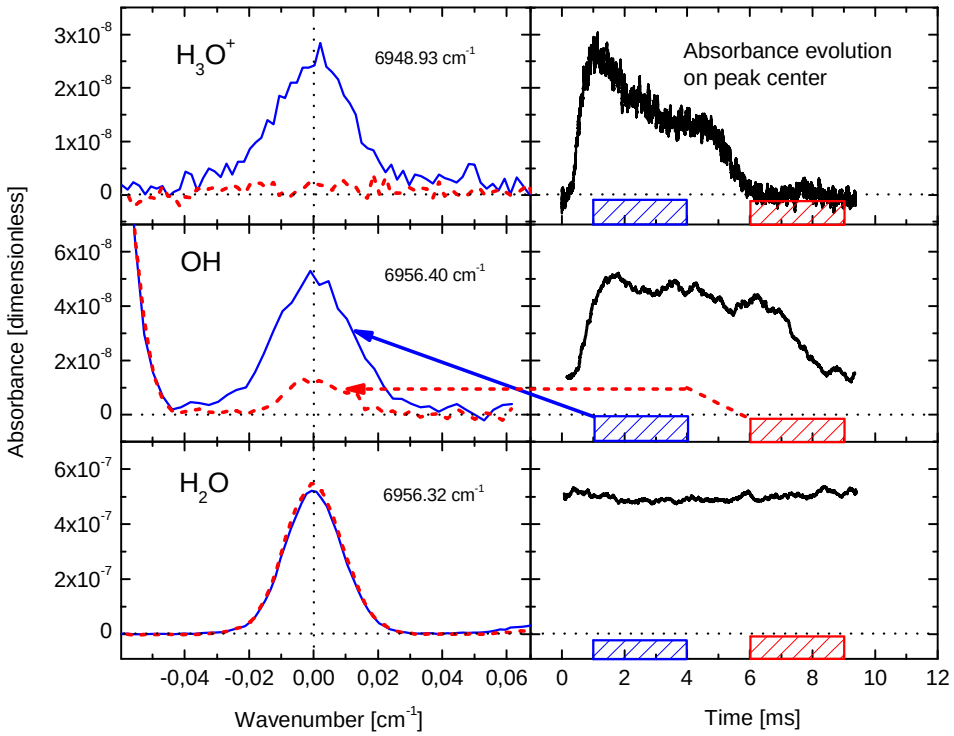

Figure 4.7 Example of evolutions for various absorbing species. Due to the time resolved character of the measurements species with various decay rates can be easily distinguished.

4.3 Wavelength calibration

Although CRDS is a very powerful technique, it does not explicitly provide information about wavelength. The wavelength of the used DFB laser is quite stable in comparison with other tunable laser sources, but its dependence on particular environmental conditions is slightly nonlinear. To acquire correct values of full widths at half maximum of the Doppler broadened absorption lines precise wavelength information is required. Therefore, in scan measurements two independent methods have been used for wavelength calibration. The *Fabry-Perrot etalon* for relative wavelength change information and the Michelson interferometer based *Wavemeter*. It is important to note that when using the AOM the frequency of the laser entering the RD cavity is shifted by 80 MHz compared to the beams used for wavelength calibration.

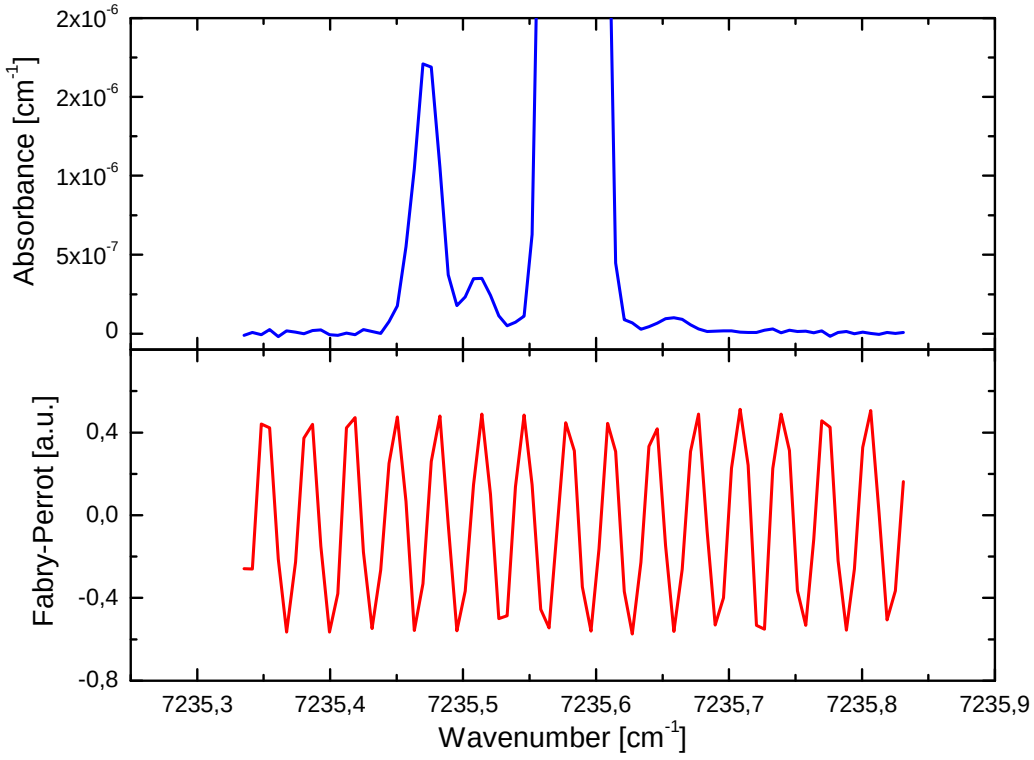

Figure 4.8 Example of measured data used for wavelength calibration. (*Upper panel*) Absorbance of water present in the rest gas. The wavelength of the observed lines is precisely known. (*Lower panel*) Corresponding signal from a low finesse Fabry-Perrot etalon.

4.3.1 Fabbry-Perrot etalon

The relative wavelength changes have been measured using a Fabry-Perrot etalon. As the etalon a cylindrical block of BK7 optical glass was used. Both ends of the glass cylinder have been polished and are plan-parallel. The reflectance of the glass-air boundary at 0 degrees incidence is roughly 4%. The low reflectivity translates into a low finesse cavity and the transmission function of this Fabry-Perrot resembles more a sinusoidal function than the usually observed high finesse etalon transfer function with sharp transmission peaks (see **Figure 3.4** for calculated 9% end **Figure 4.8** for experimental data). The resonator is 10cm long which results in a FSR of 1±0,07 GHz. The uncertainty is caused by the temperature dependence of the refraction index on temperature. The wavelength difference of successive interference maxima of the Fabry-Perrot etalon can be calculated as:

$$\Delta\lambda = \lambda - \frac{\lambda}{\frac{c}{\lambda} + FSR}. \tag{4.1}$$

The precise value of the FSR for the Fabry-Perrot etalon was calibrated using known absorption lines of H_2O.

4.3.2 The Wavemeter

For absolute wavelength calibration a Michelson type interferometer was used. The device has been built in our laboratory during previous experimental studies based on the design from [110]. Using this device the interference pattern change of a laser with unknown wavelength is compared to the pattern change of a reference laser with precisely know wavelength. In our case as the reference laser a stabilized Helium-Neon laser was used, with 632,988 nm (15798,071 cm^{-1}). The device is schematically depicted if **Figure 4.1**. The basic operation principle is as follows. Two laser beams are sent counter-propagating on the same optical path. First, both lasers are split using a 50:50 beam splitter and then send on different arms

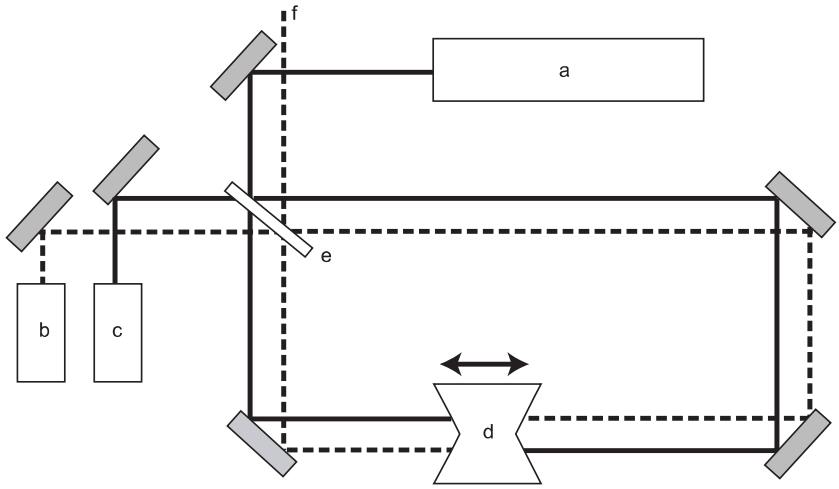

Figure 4.9 Schematic representation of the Wavemeter used for absolute wavelength measurements. a) Stabilized He-Ne laser b) detector for the measured laser c) detector for the He-Ne laser d) movable corner retro-reflector e) beam splitter f) measured laser with unknown wavelength

of the Michelson interferometer. Both arms of the interferometer end with corner retro-reflectors that are placed on a single movable carriage. This way when the carriage moves the change of length of both interferometer arms is precisely the same. The reflected laser beams are then directed back on the beam-splitter where beams from the two arms produce an interference pattern. The movement of the carriage with retro-reflectors causes a periodic change of maximum and minimum intensity in the observed interference pattern. The number of interference maximums and minimums observed during one trip of the carriage depends on the wavelength of the lasers and the distance traveled. Because the distance is the same for both lasers, the ratio of number of interference maximums of both lasers is the same as the ratio of wavelengths of both lasers. The unknown wavelength of the IR laser is calculated as

$$\lambda = \frac{N_{HeNe}}{N_{unknw}} \lambda_{HeNe}\,, \tag{4.2}$$

where N_{HeNe}, N_{unknw} is the number of interference maximums of the reference laser and the unknown laser, respectively, which were observed during one trip of the retro-reflector carriage. With 20 cm of carriage traveling distance and assuming a detectable change of only ±1 interference fringe, the theoretically attainable resolution of this device is 0,01cm^{-1} at 7200 cm^{-1} (0,003 nm around 1388 nm). In reality due to various fluctuations, the resolution of the Wavemeter is about one order of magnitude worse. But in combination with the Fabry-Perrot etalon, using calibration on known reference absorption lines and statistical averaging of Wavemeter data the precision can be improved even to values lower than 0,01.

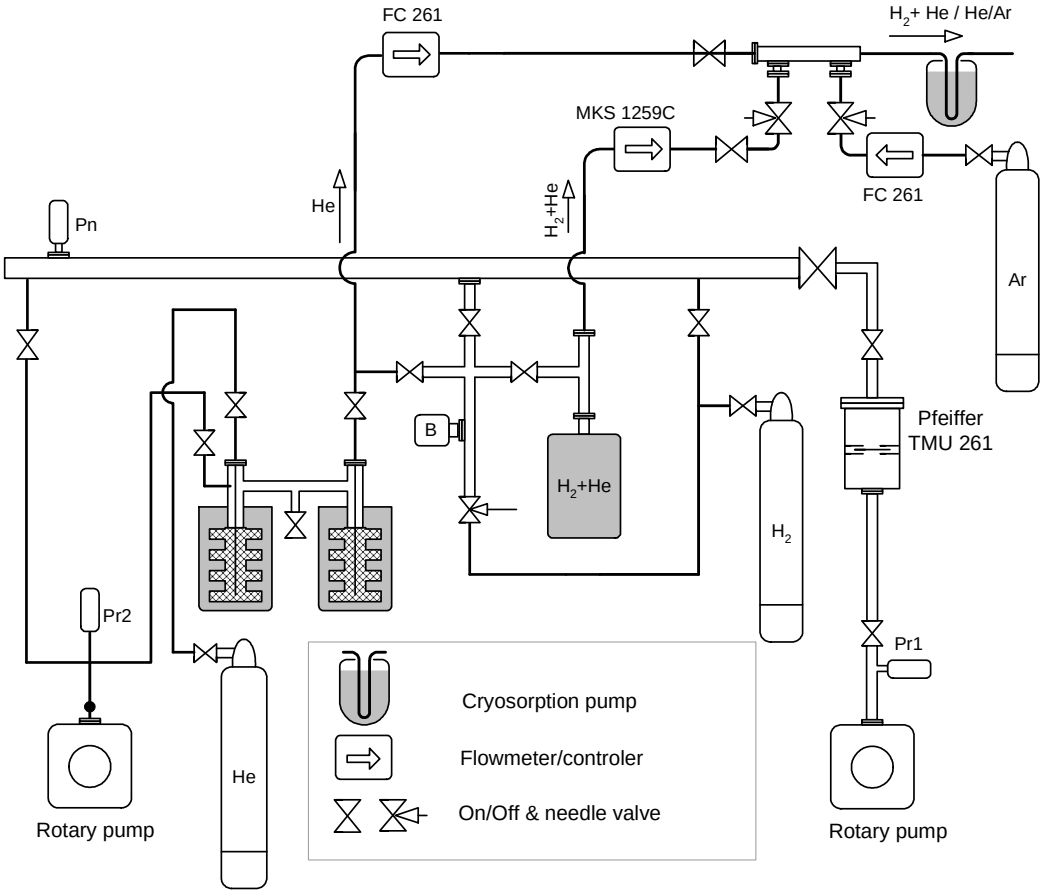

Figure 4.10 Schematic of the main gas handling and gas preparation system. This system is common with the FALP apparatus present in our laboratory.

4.4 Vacuum and gas handling system

The study of recombination of molecular ions, formed in ion-molecule reactions requires a meticulously clean environment to prevent impurities from influencing the observed process. Therefore, lot of attention was directed towards the gas handling and vacuum equipment. Apart from the "para-generator" described below, the gass-handling manifold consists of two parts, the actual gas handling system and the vacuum parts of the discharge tube that contain the optical cavity.

4.4.1 Gas handling and inlet

The gas handling system is in a big part shared with the *Flowing Afterglow Langmuire Probe* (FALP) apparatus placed also in our laboratory. A thorough description of the FALP apparatus can be found in [111,112]. The whole system is designed as UHV capable to minimize the presence of impurities. Vacuum is created using the Pfeifer TMU 261 turbo pump with rotary pump backing. The whole inlet system is bake-able to 120 centigrade. Helium was used as buffer gas in all here presented experiments. The gas was provided from a pressure vessel containing helium of 5.0 purity. Additionally, to further clean the helium, it flows through a zeolit molecular sieve cooled by liquid nitrogen. During experiments, the flow of helium is measured by a mass flow meter from MKS Instruments with range 0-10000 sccm and controlled by a throttle valve. Argon is controlled in the same way using a flow meter from the same company with a working range 0-10 sccm. Control and feedback of the reactant flow (hydrogen) is provided by means of a mass-flow controller from MKS instruments with range 0-10 sccm. In order to achieve lower concentrations of reactants in the discharge tube, Hydrogen is mixed with helium prior to the experiment in a reservoir and the resulting mixture is used as the source of the reactant. Argon is be added to the mixture optionally as well. This allows for concentrations of the reactant hydrogen gas of ~10^{12} cm^{-3} in the discharge tube at 5 mbar and 77 K, i.e. ~5×10^{18} cm^{-3} buffer gas density. Using argon diluted in helium for injection from the mixing reservoir is employed with the use of para-enriched Hydrogen that is fed into the discharge tube from the "para generator" that has a separate vacuum and gas handling system (see description below). This way lower concentration of Ar in the discharge tube is achieved than would be otherwise possible when using only the mass-flow controller for Ar flow. All gases from the shared gas handling system are mixed together. The gas He/H_2/Ar mixture passes through another cryogenic molecular sieve at 77 K prior to entering into the discharge region. To prevent Argon from freezing to the walls in the sieve it is located in the low-pressure part of the inlet tubing. Pressure in the inlet system is monitored by a cold cathode Penning gauge combined with a Pirani gauge in the form of a Pfeifer vacuum compact full range gauge. The backing pressure of the turbo pump and the auxiliary rotary pump pressure are controlled with Pirani gauges.

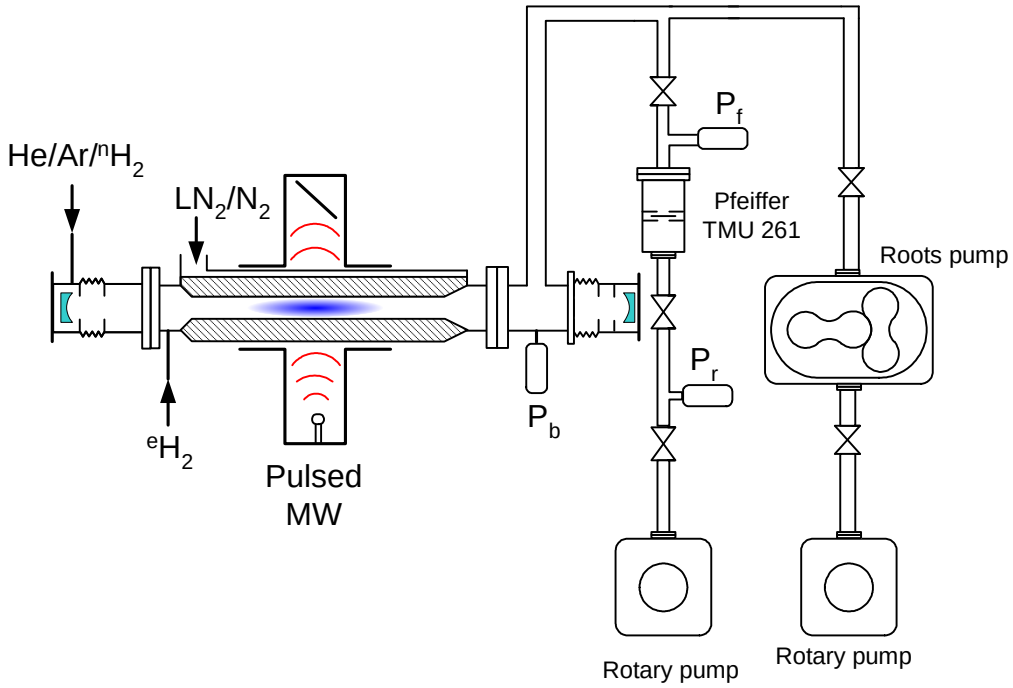

Figure 4.11 Schematic of the vacuum of the discharge tube housing the CRD spectrometer high reflectivity mirrors. P_r – Pirani gauge, P_b-capacitance gauge, P_f – full range gauge (see text)

4.4.2 Microwave Discharge Tube

The discharge tube with the corresponding vacuum and temperature control equipment served as the inspiration for the name of the whole experimental setup, the *microwave discharge tube* (MDT). Vacuum schematic of core parts of the microwave discharge tube is depicted in **Figure 4.11**. The vessel is evacuated by a Pfeifer vacuum TMU 261 turbo pump backed by a rotary pump. The MDT is heated during pumping to ~60°C for better impurity control. Lower temperatures than in the gas handling system are used due to rubber o-rings used on the glass metal interconnects and some KF connections. During pumping the pressure is monitored by a Pfeifer vacuum compact full range gauge of the same type as used in the gas handling system described above. After bake out, pressures of ~7×10^{-8} mbar are usually achieved. The lower rate of dust particles falling on the CRD cavity mirror caused by the horizontal placement of the cavity resulted in prolonged periods without the need to breach the vacuum of the MDT. This in turn resulted in a better

achievable rest gas pressure and thus lower impurity content than in implementations with a vertical cavity. The observed leak rate of the apparatus was $9{\sim}10^{-5}$ sccm. Considering the commonly used buffer gas flow of 1000 sccm these results in an impurities leak to reactant flow ratio of $\sim 10^{-7}$ during experiments. In most of the experiments the impurity ratio was further improved by the fact that walls of the apparatus were at 77 K thus majority of the leaking impurities was freezing out on the walls. During experiments the pressure inside the MDT is monitored by a Baratron® capacitance gauge from MKS instruments with a range 0-10 mbar and 0.1% precision.

The actual discharge tube is made of fused silica and has an inner diameter of approximately 1,5 cm. The middle 20 cm of the tube are cooled by either LN_2 or cool N_2 vapors. Although the thinner discharge tube resulted in faster ion ambipollar diffusion rate, the observed ion kinetic temperatures were much closer to the wall temperature than in previous experiments (see results in chapter 5). For details of the plasma microwave generator, see bellow.

To avoid confusion for readers familiar with previous publications of our group please consider that the CRD spectrometer together with its vacuum equipment was in previous works referred to as the "*Test tube*" apparatus.

4.4.3 Plasma generation

The microwave radiation for plasma creation in presented experiments was generated by a commercial microwave source from Sairem GMP-03-KED supplying radiation at 2.45 GHz with maximum output power of 300 W. The source was connected by a coaxial link to a waveguide, also from Sairem Company. The discharge tube passed through a circular aperture perpendicular to the waveguide. The wave-guide consists of a microwave input, impedance tuning section and a short circuit back plate. The impedance tuning is used to match the plasma containing waveguides impedance to the used source in order to prevent reflections and potential damage to the source. The aperture used for the discharge tube is equipped with $\lambda/2$ shielding extension to prevent radiation leakage. This limits the discharge area to the inner section of the wave-guide producing a plasma column of approximately ~5 cm. The diffusion of charged particles out of the discharge is slow and can be neglected at used conditions.

The used microwave source is equipped with and analog input for power output control. Unfortunately, the turn of speed using this analog control interface was not sufficient. For the study of recombination, it is crucial that the microwave radiation inside the discharge tube decays very rapidly and does not disturb the afterglow by residual ionization. In order to assure that, the MW source has been equipped with an external high voltage switch to cut the HV powering the MW

source magnetron and thus terminating microwave generation. This reduced the turn of time from ~0,5ms to ~30 μs (see figure 2.14 in ref. [66]).

Although the source is capable of delivering up to 300 W of incident power, only low incident power levels of around 15 W with ~50% duty cycle were used in order to avoid excess heating of ions during the discharge. The timing for microwave source and switch were provided by a pulse generator. The used repetition frequency varied from 50 Hz synchronized with the 220 AC power supply to ~200 Hz AC unsynchronized.

4.5 Para generator

Hydrogen gas at room temperature has approximately 25% of its molecules in states belonging to the para nuclear spin symmetry (spins aligned anti-parallel). The rest of the molecules are in ortho nuclear spin states (spins aligned parallel). Hydrogen with this composition is referred to as "*normal H_2*" ($^nH_2$) in this work (commonly used also by other groups). Because of the weak coupling of nuclear spin to other degrees of freedom, the probability of changing the nuclear spin in inelastic collisions is very low. Under normal circumstances in clean conditions hydrogen usually retains his normal composition. When hydrogen gas is conventionally cooled to cryogenic temperatures, its energy is removed only via inelastic collisions and molecules do not change their nuclear spin. So, molecules with ortho nuclear spin configuration can de-excite only to the second lowest rotational energy state, which belongs to the ortho nuclear spin symmetry. Even though the lowest rotational state of H_2 belongs to the para spin symmetry group and should be exclusively populated at sufficiently low temperatures also the second lowest rotational state, that has ortho spin symmetry, stays populated and H_2 retains its room temperature para/ortho composition ($^nH_2$). If hydrogen is exposed to a suitable paramagnetic catalyst that can facilitate the nuclear spin change, then a thermal distribution of populated states can be achieved. This posses a significant threat when Hydrogen is to be liquified. If liquification takes places in a clean environment and liquid H_2 is then accidentally exposed to a catalyst the energy stored in the ortho states is released leading to a pressure surge and possibly an explosion.

At LN_2 temperature the thermal ratio of para/ortho states is equal to 1. If H_2 is cooled down under ~19 K in the presence of a catalyst then only the lowest rotational state, that has para spin symmetry, is significantly populated. When the catalyst is then removed and the H_2 reheated, it retains its low temperature para/ortho ratio with a significant enrichment of para states in the gas over its thermal distribution. In this work we refer to this gas as "*para enriched H_2*" ($^eH_2$).

The production of para enriched hydrogen is a quite old matter with first successful attempts in 1929 [113] as it is bound to the production of liquid H_2. Until the present day, many technical solutions have been proposed, tried and are used. For small scale experimental purposes one of the most popular approaches today is to use

a closed circle helium cryostat (cold-head) to cool down a conversion chamber or region containing the catalyst [114]. Hydrogen either is injected once or flows continuously through the conversion chamber or region to produce the $^{e}H_2$. This approach was also used in the apparatus built in our laboratory.

4.5.1 Para generator vacuum and gas handling

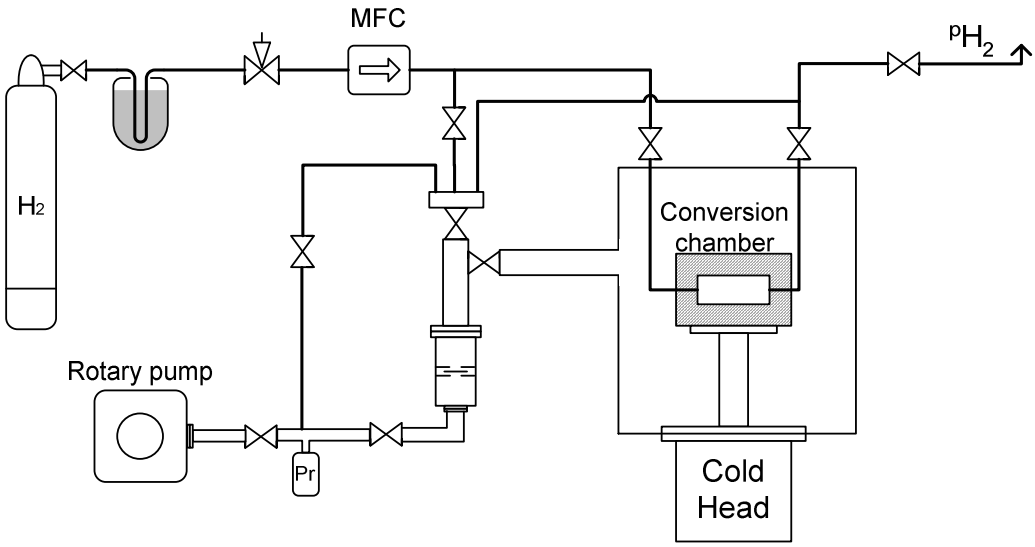

Figure 4.12 Schematic representation of the *para generator* gas handling manifold and vacuum equipment. Vacuum is used both for maintaining a clean environment and for thermal insulation.

The para generator has been built as a stand-alone apparatus with ease of operation and portability in mind. Schematic representation of the gas handling and vacuum equipment is depicted in **Figure 4.12**. Vacuum connections use the ConFlat® technology and tubing is realized with the use of Swagelok systems. The whole apparatus is UHV capable but the presence of the closed cycle helium cryostat imposes an upper limit of 50°C for the bakeout of the vacuum chamber. The gas routing tubing is routinely heated to 70°C. During the construction, special attention was paid to cleaning of the vacuum parts to minimize the possible contamination of the room temperature outlet tubing with particles of the catalyst that could thermalize the para enriched hydrogen exiting the apparatus. All vacuum and gas handling parts are non-magnetic for the same reason. To prevent the flushing of the catalyst out of the conversion chamber the entrance and exit tubes are each equipped with two fine particle filters from Svagelok company. As the catalyst Fe_2O_3 in the form of grit with particles few centimeters in diameter from the Aldrich Company was used. Although fine powder Fe_2O_3 can be obtained it was not used in order to lower to possibility of

contaminating room temperature parts of the apparatus. However, to increase the surface available for conversion the catalyst was crushed to particles with sizes of approx. 1mm that can still be effectively confined to the conversion chamber. The conversion chamber is made of solid copper with Swagelok connections brazed to it.

The vacuum vessel housing the conversion chamber is evacuated by a turbo-molecular pump thus providing the isolation vacuum for the cold head.

4.5.2 Operation and Flow calibration

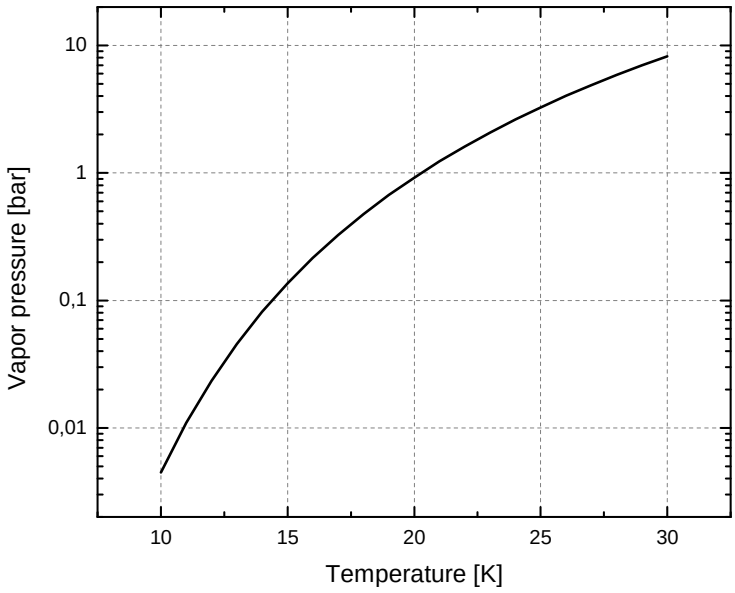

Figure 4.13 Vapor presure of normal Hydrogen at crygenic temperatures. Dependence extrapolated from [115]

After cooling the conversion chamber to 10 K, room temperature Hydrogen is introduced into it. At 10 K is the vapor pressure of $^{n}H_2$ approximately 4.6 mbar (see **Figure 4.13**). If the Hydrogen is introduced at a higher-pressure than the vapor pressure, condensation on the wall and catalyst grains starts. This way a significant amount of gas can be stored inside the conversion chamber. After the inflow of gas is stopped, the conversion chamber is then heated and stabilized at a particular temperature by means of a heating element combined with a PID regulator. Next the exit valve is opened and held in a fixed position. The out flow of hydrogen is predominantly defined by the pressure inside of the conversion chamber which is controlled by means of a heating element attached to the conversion chamber. For repeatable and reliable experimental conditions the gas flow of the para enriched hydrogen during experiments has to be known. Since the use of classical mass flow

meters on para generator exit could lead to back conversion an alternative calibration method was employed.

First a repeatable procedure for setting a fixed gas flow was devised that was later calibrated. After the filling of the conversion chamber and closing the inlet valve the conversion chamber was always heated up to 18 K so the pressure inside the conversion chamber increased to approximately 480 mbar. Next the exit valve of the para generator was slowly opened while the MDT apparatus was still being pumped. The resulting gas flow increased the pressure observed over the turbo-molecular pump that was evacuating the MDT. The exit valve was opened and fixed so that the observed pressure over the turbo-molecular pump was the same in all measurements. Next by changing the temperature of the conversion chamber the pressure of H_2 inside and the corresponding gas flow was varied. The actual gas flow was calibrated by measuring the time depended pressure increase inside the discharge tube when pumping was shut of for different temperatures of the conversion chamber. The observed dependences were linear for throughout the increase in the range 0-10 mbar for all temperatures of the conversion chamber, i.e. even low flows of $^{e}H_2$ to high pressure discharge ~10 mbar were reliably reproducible. The observed gas flows for different conversion chamber temperatures are depicted in **Figure 4.14**. The calibration was performed for two different exit valve positions at 18 K. This calibration procedure showed that even in experiments with low $^{e}H_2$ flow and high pressure inside the discharge tube (~10 mbar) the $^{e}H_2$ flow is reliably determined. From this **Figure 4.14** one can also see that there is a lower flow limit that can be reliably injected into the discharge region. It is given by the difference of pressures inside the conversion chamber and discharge region.

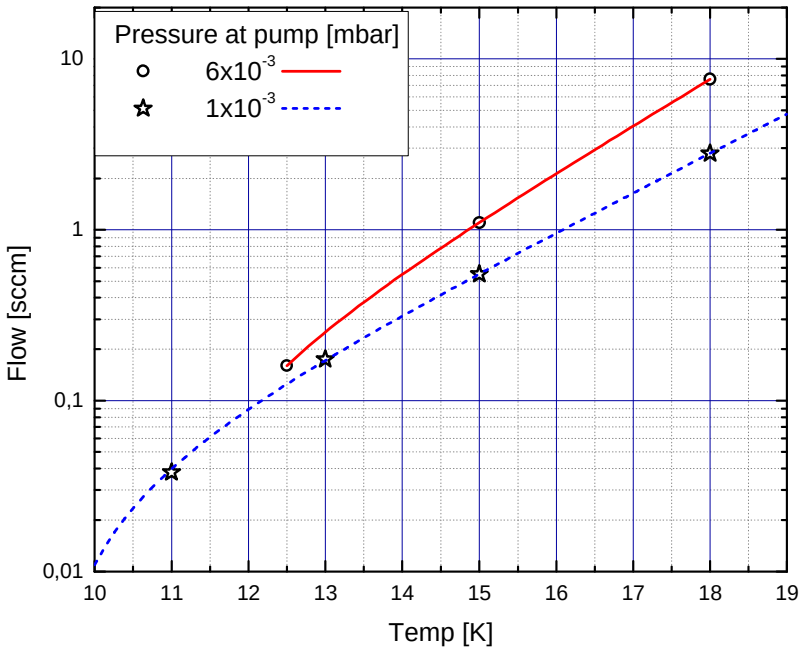

Figure 4.14 Para generator flow calibration using the 1l volume of the discharge tube as reference. Flow was determined from the slope of the pressures time dependence when pumping was shut off.

4.5.3 Measurement of para enrichment

Nuclear magnetic resonance was used to check on the para/ortho states ratio in the produced $^{e}H_2$. NMR diagnostic test tube made from pyrex low expansion glass was filled with $^{e}H_2$ and subjected to a 20 hour probing of the ortho states population. Para Hydrogen has no overall nuclear spin and is therefore not detectable using NMR. The NMR test tube was submerged in LN_2 during filling in order to increase the number density of $^{e}H_2$ inside. The measurements indicate a 87±5% content of para states and a lifetime of (96±4) hours (see **Figure 4.15**). The observed lifetime is in agreement with observations of other groups for para back-conversion in glass containers [116][117].

Apparatuses of similar design all around the world produce $^{e}H_2$ with over 99% enrichment ratio. Although a very high enrichment was not necessary for the experiments presented in this work (see chapter 2.6) it is an interesting question why higher enrichment ratios were not observed. The reason for this could be various. In literature one finds information about “activation” of the catalyst by heating it in a hydrogen atmosphere [116]. This increases the efficacy of the conversion by desorbing water and impurity molecules from the surface of the catalyst thus increasing the space available for conversion. No activation of the catalyst was performed so the catalyst stored at almost atmospheric conditions can operate below optimal. Another, more plausible explanation, is that the low observed ratio is tied to

the extraction procedure of the $^{e}H_2$ into the NMR test tube. In the process the conversion chamber was heated to 19 K to increase pressure inside. Then for a short time the exit valve is opened allowing gas to flow into the evacuated test tube. The pressures rapidly equilibrate and valves are shut both on the test tube and para generator. Since the heating element is on the other side as the heat sensing element and no time was spent on waiting for the temperature to settle, local hot spots inside the conversion chamber could have been created thus converting some of the para H_2 back. Since such high temperatures (~19 K) were never used during actual experiments it is possible that although the measurements of para enrichment indicate only 87% para content, the actual experiments were performed with $^{e}H_2$ with higher enrichment than that.

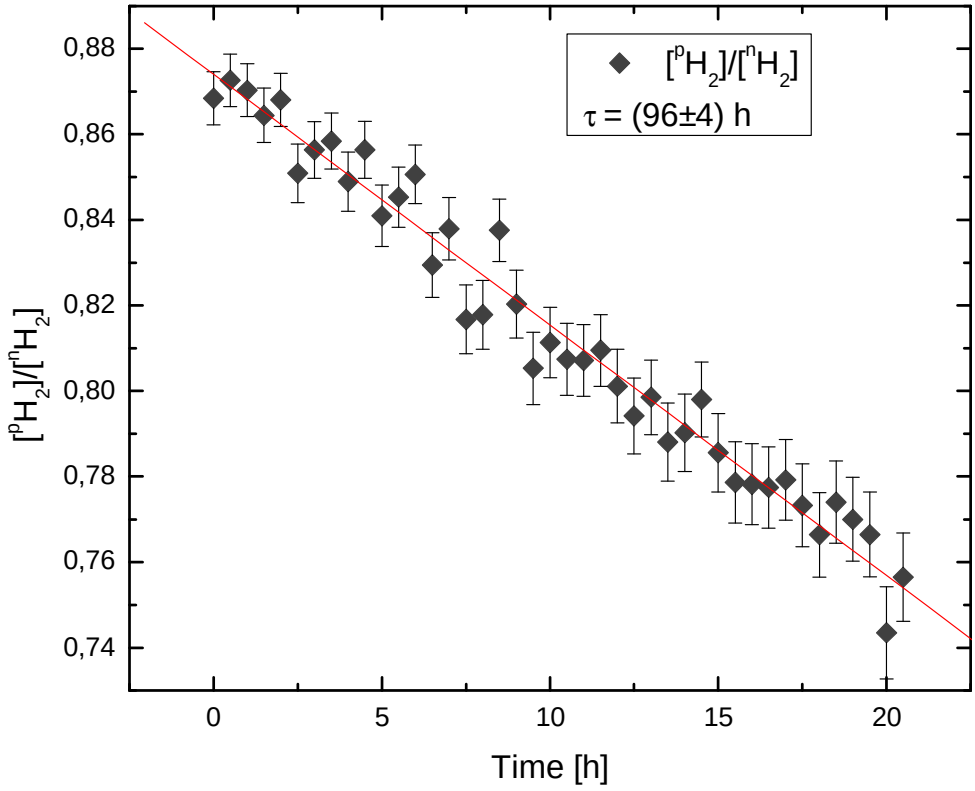

Figure 4.15 The time evolution of the para/ortho H_2 ratio probed using the NMR technique of a sample produced with the described *para generator*.

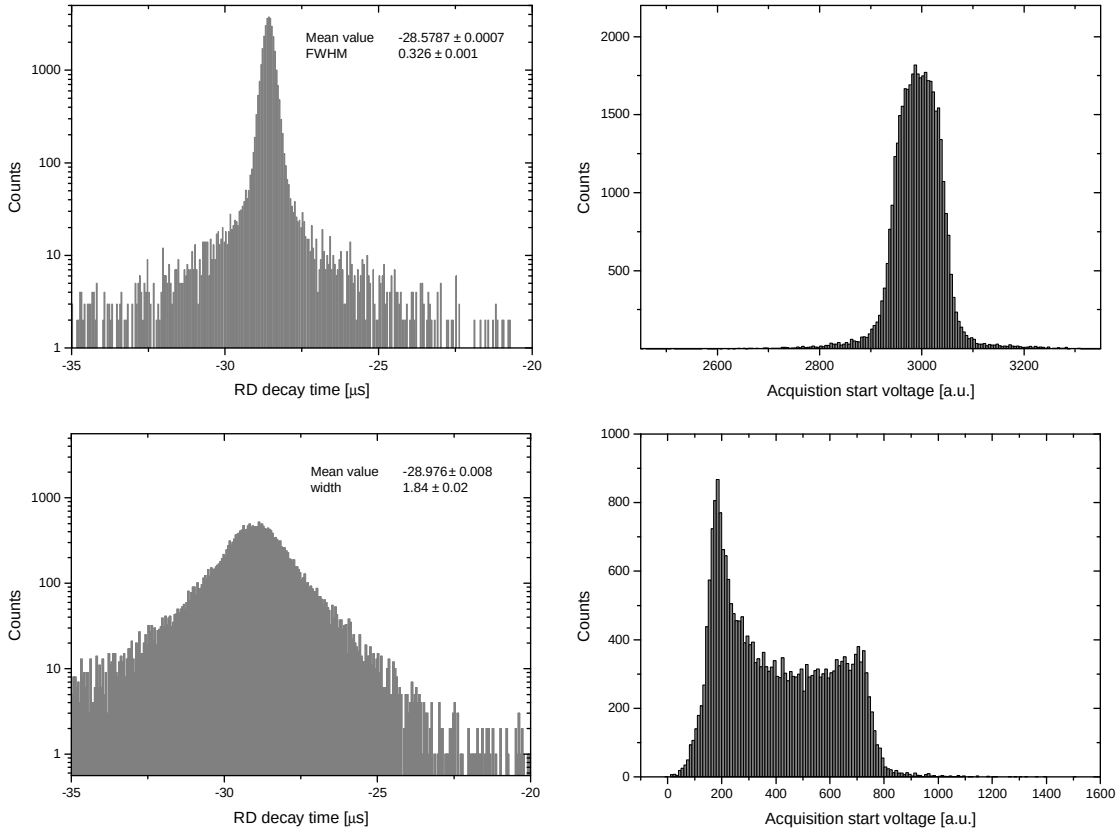

Figure 4.16 Distrubutions of observed RD times for two different aqusition start „schemes“, demonstrating the importance of proper switching. *Upper panels:* normal operation. *Lower panels:* distributions recorded during a malfunction of the control electronics. The start aqusition varied wildly (distribution on the right) cousing an significant increase of the observed RD times spread.

4.6 Apparatus summary

The author during his studies performed various changes and upgrades to the experimental apparatus used for the previous works of our group. For comparison see Attached publication V. The changes include:

- Due to the exchange of the data acquisition card the control software underwent significant changes although the main working principle remained the same as before.
- The cooling equipment was designed and built the together with the corresponding changes in the discharge tube arrangement.
- Minor improvements of the optical beam manipulation setup.
- Construction tests and operation of the para generator.

5 Experimental Results

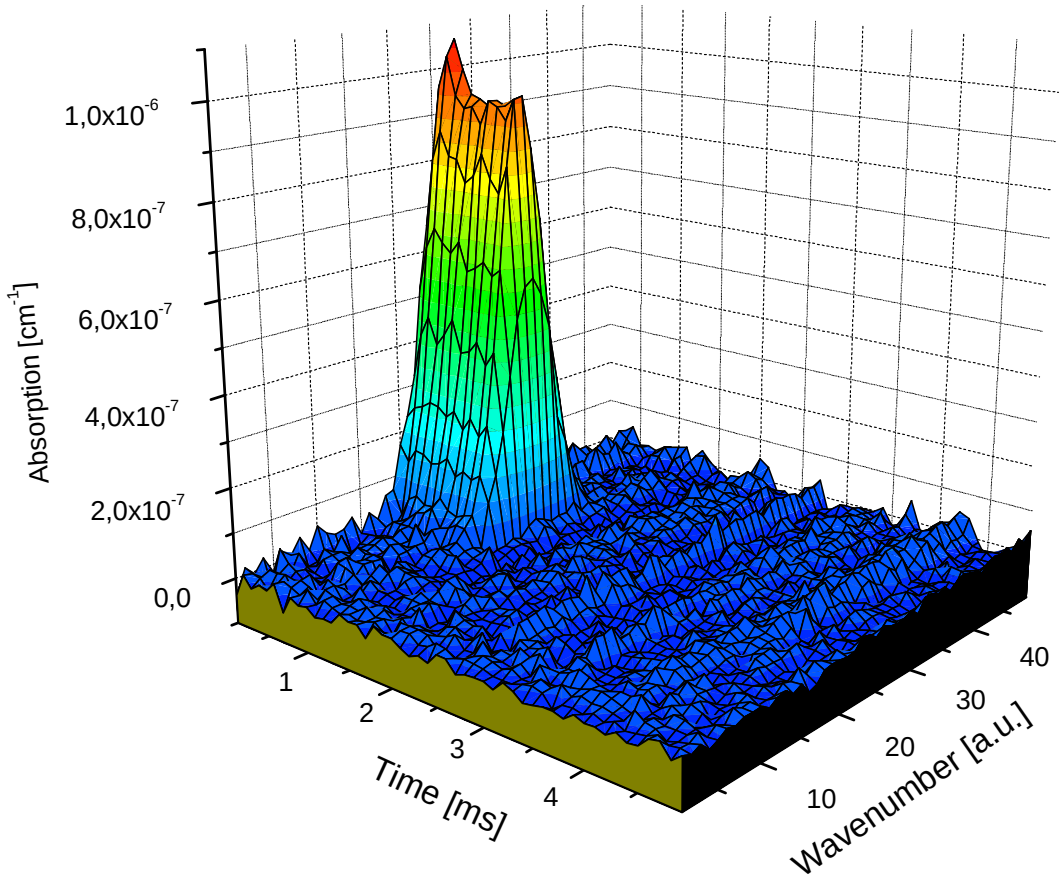

Figure 5.1 Example of measured data. Time resolved CRDS spectroscopy allows observation of time evolution of all parameters observable by spectroscopic measurements.

In this chapter the results of the experiments performed in order to study the state sensitive recombination of H_3^+ are summarized. The experiments were performed on the apparatus described in chapter 4 of this work. The unique features of the used apparatus allowed observing of the time evolution of a range of plasma parameters (for example of measured data see **Figure 5.1**).

The most important data concerning the recombination of H_3^+ are divided in two parts, the results obtained in experiments with $^nH_2$ and results obtained with

$^{e}H_2$ used as precursor. Enriched H_2 used as a reactant significantly increases the fraction of H_3^+ ions in the para nuclear spin states compared to using normal-H_2. Using these two sets of experimental data we extrapolated the recombination rate coefficients for afterglow plasmas composed of pure para-H_3^+ and pure ortho-H_3^+. Experimental data sets were obtained at a wide range of experimental conditions.

All spectroscopic measurements were performed using second overtone transitions from the ground vibrational level of H_3^+. Two lowest rotational levels of the vibrational ground state were observed predominantly. Each of these two levels has a different spin symmetry so both the lowest para-H_3^+ and ortho-H_3^+ energy levels were observed. At several occasions a higher lying ortho-H_3^+ level (3,3) was also probed. The transitions used in this work are summarized in **Table 5.1**. The particular transitions were selected because their frequency proximity that allowed to use only one DFB laser to measure them both. This facilitated measurements of both spin states in rapid succession during the experiments.

Wavenumber [cm^{-1}]	Spin	Low lvl. [cm^{-1}]	Up. lvl. [cm^{-1}]	Transition
7234,957	o	315,349	7550,316	$3\nu_2^1(4,3) \leftarrow 0\nu_2^0(3,3)$
7237,285	p	64,1234	7301,4084	$3\nu_2^1(2,0) \leftarrow 0\nu_2^0(1,0)$
7241,245	o	86,9591	7328,2041	$3\nu_2^1(2,1) \leftarrow 0\nu_2^0(1,1)$

Table 5.1 Parameters of transitions used in the presented study.

5.1 Formation of H_3^+

First step in recombination studies was the creation of H_3^+ dominated plasma, particularly H_3^+ dominated afterglow. This matter has been extensively studied in our laboratory in the past [118][119][120]. Selection of experimental conditions used for the present work was based on them. For the studies of H_3^+ formation, numerical models were used as a first approximation with later verification using mass spectrometry in the mentioned experimental work.

In the present study H_3^+ dominated plasma was created in a microwave discharge in a mixture of He/Ar/H_2/$^{e}H_2$ with varying ratios as in previous studies of our group. Only a short overview of the formation of H_3^+ in discharge and stationary afterglow conditions, like the ones applying TDT, will be presented here. For details the reader is advised to look in references [47][78] and the references therein where detailed numerical models with experimental verification have been performed. The main reactions involved in the process of creating H_3^+ dominated plasma are shown in **Table 5.2.** During the discharge He and Ar atoms are ionized by roughly the same amount although [Ar] is typically only < 1% of [He]. He_2^+ and He^m are also formed but undergo a rapid charge transfer or penning ionization with argon to produce Ar^+.

In collisions of Ar^+ with H_2 the ions H_2^+ and ArH^+ are formed that in a subsequent collision with H_2 produce H_3^+.

R. No	Reaktion	Rate coefficient	Reference
1	$He^+ + 2He \rightarrow He_2^+ + He$	1×10^{-31} $cm^6 s^{-1}$	(Ikezoe, 1987)[121]
2	$He^M + He^M \rightarrow He_2^+ + e$	5×10^{-9} $cm^3 s^{-1}$	(Deloche, 1976)[122]
3	$He^M + Ar \rightarrow Ar^+ + He + e$	7×10^{-11} $cm^3 s^{-1}$	(Glosik, 1999)[123]
4	$He_2^+ + Ar \rightarrow Ar^+ + 2He$	2×10^{-10} $cm^3 s^{-1}$	(Ikezoe, 1987)[121]
5	$Ar^+ + H_2 \rightarrow ArH^+ + H$	8×10^{-10} $cm^3 s^{-1}$	(Dotan, 1982)[124]
6	$Ar^+ + H_2 \rightarrow H_2^+ + Ar$	1×10^{-10} $cm^3 s^{-1}$	(Dotan, 1982)[124]
7	$H_2^+ + Ar \rightarrow ArH^+ + H$	$2{,}3\times10^{-9}$ $cm^3 s^{-1}$	(Glosik, 1994a)[125]
8	$H_2^+ + H_2 \rightarrow H_3^+ + H$	$2{,}1\times10^{-9}$ $cm^3 s^{-1}$	(Glosik, 1994a)[125]
9	$ArH^+ + H_2 \rightarrow H_3^+ + Ar$	$1{,}5\times10^{-9}$ $cm^3 s^{-1}$	(Villinger, 1982)[126]
10	$H_3^+ + H_2 + He \rightarrow H_5^+ + He$	$<1\times10^{-29}$ $cm^6 s^{-1}$	(Smirnov, 1984)[127]
11	$H_3^+ + H_2 + H_2 \rightarrow H_5^+ + H_2$	$4{,}6\times10^{-30}$; 210K	(Johnsen, 1976)[128]
12	$H_5^+ + He \rightarrow H_3^+ + H_2 + He$	$<1\times10^{-13}$ $cm^3 s^{-1}$	(Glosík 2003)[67]

Table 5.2 The main reactions participating in the formation of H_3^+ in a discharge in a $He/Ar/H_2$ gas mixture.

5.2 Temperature determination

Next crucial step in the study was the temperature determination of the studied ions to confirm the performance of the cooling. In the range of used buffer gas number densities ($1–20\times10^{17}$ cm^{-3}) the created ions have approximately one collision with He every few ns and several collisions with electrons within a µs. These collision conditions ensure a fast thermallisation of all particles participating in recombination of H_3^+. Most importantly the evolution of temperature during the discharge had to be measured to exclude any heating of H_3^+ ions. Although the cooling via collision with He buffer gas is very effective and fast at used number densities increased temperatures of H_3^+ ions at the end of the discharge are to be avoided. Otherwise the observed decay would be influenced by the elevated temperature for a long time, compared to the recombination time constant, thus making the obtained reaction rate coefficients unreliable. Since the decay due to recombination is a second order process (see paragraph 5.4) it is "faster" at higher concentrations, such as in the beginning of afterglow. Higher temperatures of the ions would require that the fits of the decay curves start much later in the afterglow when the ions cool down. That means to start fitting at significantly lower

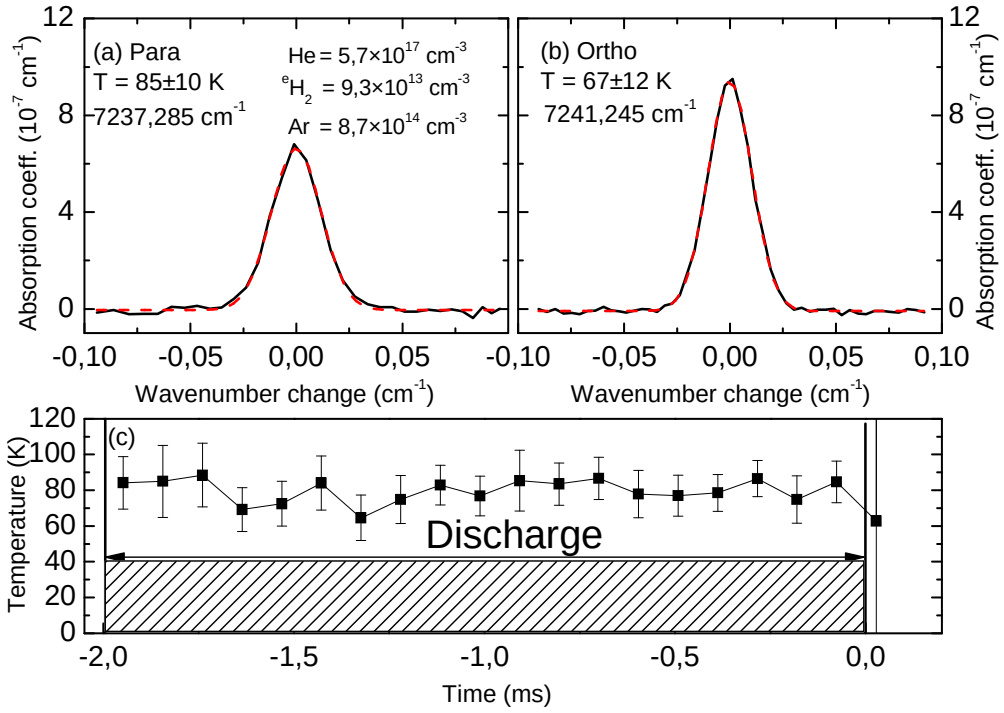

Figure 5.2 (*Upper panel*) Example of measured frequency scans of H_3^+ absorption lines. For each frequency point the mean value of absorption during far afterglow was subtracted from the mean value during the discharge. (*Lower* panel) Evolution of the ion temperature during the discharge. These measurements show the low temperature and absence of heating of the ions during discharge.

concentrations of H_3^+ and thus decrease the signal to noise ratio of the experimental data. Therefore proper cooling was essential to the experiments.

Simple frequency scans of Doppler broadened absorption lines yield information only on the average kinetic temperature during discharge in the width of the observed absorption line (see Equation 3.16). Time-resolved scan measurements were evaluated to obtain the evolution of absorption line width, i.e. ion temperature. Example of the observed absorption lines and temperature evolution during discharge is shown in **Figure 5.2**. From this data we can confidently say that the temperature of the ions is very close to the wall and buffer gas temperature of 77 K. In previous studies of our group [66] the buffer gas temperature at higher temperatures has been measured also by observing absorption lines of H_2O that provided temperature information during the whole discharge cycle. Unfortunately this approach could not be applied here as the temperature used was to low and basically all water (considered as impurity) is frozen out on the walls of the discharge tube.

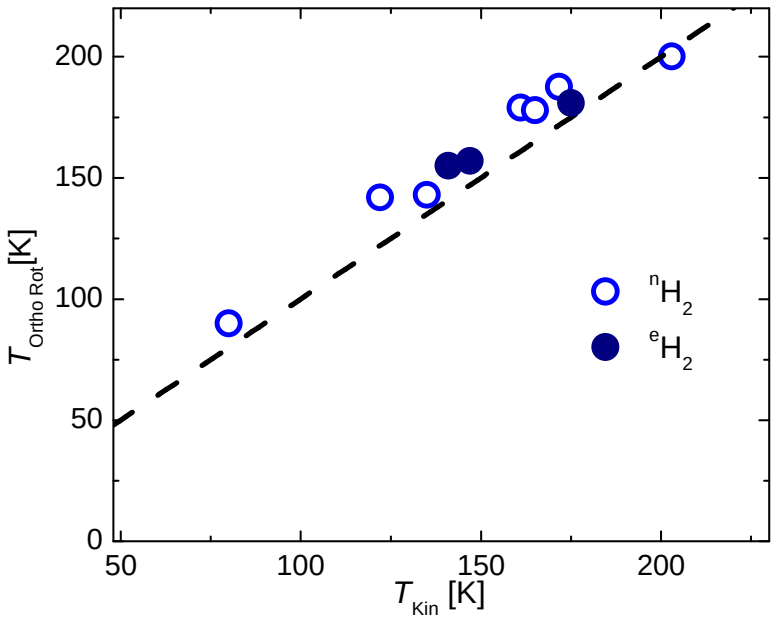

Figure 5.3 Rotatinal temperature of H_3^+ obtained from population ratios of different ortho levels as a function of kinetic temperature obtained from Doppler broadening of the observed absorption lines.

It is worthwhile to note that although using a very similar discharge tube and cooling setup, than in previous studies, the ion temperature is much closer to LN_2 temperature. This was achieved among other changes by using a discharge tube with a smaller inner diameter (1,5 cm vs. 4 cm) that allowed for better heat transfer from the flowing gas. The gas flows for about 10 cm through the already cool discharge tube before the discharge is ignited, compared to less than 5 cm in previous

studies. Also only about half of the microwave power was used (15 W vs. 30 W both with ~50% duty cycle) to ignite the plasma. This experimental information on kinetic temperature also strongly suggests that the internal excitation of the ions is well thermalized. In measurements with LN_2 cooling after initial confirmation of the ion temperature, were temperature measurements made only sporadically. Similar temperature data were observed for measurements at higher temperatures where cooling with cold N_2 vapors was employed. Due to the lower repeatability of the N_2 vapor cooling temperature measurements were made frequently.

As for the internal excitation of formed ions, we assume that all higher vibrational states are sufficiently quenched in collisions with He, Ar atoms and H_2. Rotational excitation is quenched mostly in collisions with electrons [129]. We assume that all H_3^+ ions are in their ground vibrational state with a thermal distribution of rotational states population corresponding to the buffer gas temperature. In the H_3^+formation process described earlier H_3^+ ions in vibrational states up to $v = 5$ can be created but in further collision with Ar all H_3^+ ions with internal energies above 0,57 eV are rapidly destroyed leaving only ions in $v \leq 2$. At temperatures where at least two ortho H_3^+ absorption lines were observable the rotational temperature was calculated. The dependence of the rotational temperature on the kinetic temperature determined from the Doppler broadening of the absorption lines is shown in **Figure 5.3**. Considering the uncertainty of both measurements we can confidently say that studied ions are both kinetically and internally thermalized.

5.3 Expected population of H_3^+

The population of first few H_3^+ energy levels at 80 K and 140 K is shown in **Table 5.3**. The distributions were calculated using **equation 3.8** and energy levels list was obtained from [94]. The partition function was obtained by explicit summation of the available energy levels according to **equation 3.9**. It is evident that by measuring the number densities of the two lowest H_3^+ energy levels at around 80 K one obtains information about 85,65% of all H_3^+ ions present, if thermodynamic equilibrium is assumed.

Spin	J	Energy [cm-1]	occup. at 80K [%]	occup. at 140K [%]
p	1	64,1234	36,82	25,14
o	1	86,9591	48,83	39,76
p	2	169,2961	9,26	14,21
p	2	237,3499	2,72	7,06
o	3	315,3416	1,87	8,87
p	3	428,0087	0,12	1,39
p	3	494,7532	0,04	0,70
p	4	502,0227	0,04	0,84

Table 5.3 The distribution of populations of the first few rotational energy levels of the ground vibrational level of H_3^+ at 80 K and 140 K. Spin symmetries and total angular momentum (J) are also indicated.

Partition functions for separate para and ortho states of H_3^+ were used to derive the equilibrium overall ratio of para/ortho states at different temperatures. The result is shown in **Figure 5.4**. The para-H_3^+/ortho-H_3^+ ratio is ~1 upwards from 50 K. In the evaluation of experimental data we assumed that both spin symmetry manifolds thermalise separately but are not necessarily in thermal equilibrium with each other (depending on used H_2 number density). In other words, ortho-H_3^+ rotational states have a population distribution like in thermal equilibrium but the overall ratio para-H_3^+/ortho-H_3^+ is non-thermal.

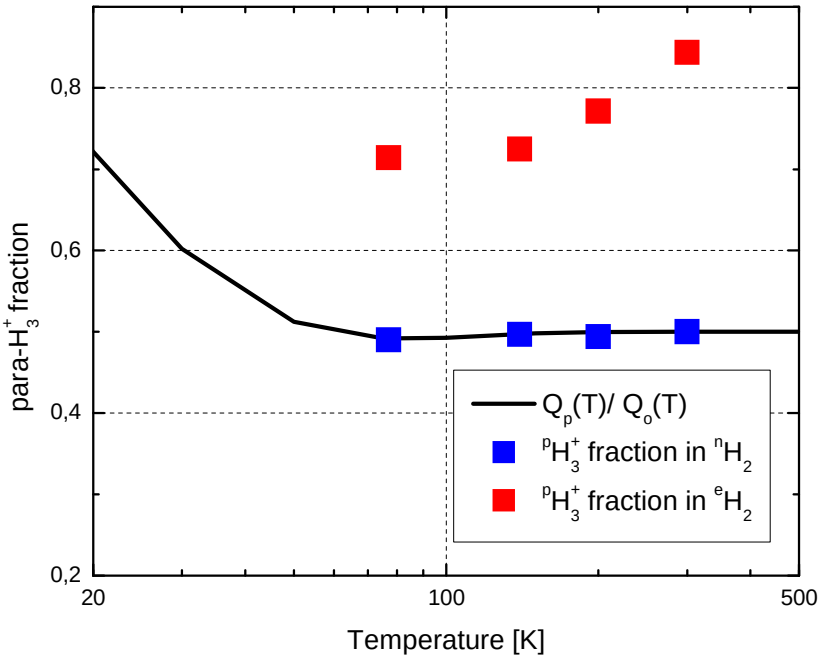

Figure 5.4 Ratio of para/ortho H_3^+ states as a function of temperature calculated using separate partition functions ($Q_p(T)$ and $Q_o(T)$) for different nuclear spin symmetry states of H_3^+. Ratios measured in $^nH_2$ (*blue*) and in $^eH_2$ (*red*) for various temperatures are also shown.

5.4 Volume recombination evaluation

In recombination governed bulk plasma (e.g. afterglow) where majority of recombination events are due to only one ionic species the whole plasma deionization process can be described by one reaction rate constant (neglecting diffusion). For this case the loss of charged particles follows the balance equation (assuming ion and electron concentrations are equal $n_e = n_i = n$)

$$\frac{d[n_e]}{dt} = -\alpha.[n_e]^2 . \qquad (5.1)$$

The reaction rate coefficient α is a function of temperature so its use implicitly assumes a plasma in thermal equilibrium. For environments where temperature in the sense of particle distribution parameter can not be straightforwardly applied, such as beam experiments, the recombination cross-section σ(E) is usually used. Cross section is a function of collision energy but is often presented as a function of temperature by applying the equipartition theorem. The thermal recombination rate coefficient can be obtained from the cross-sections energy dependence as:

$$\alpha(T) = \langle \sigma v \rangle = \int_0^\infty \sigma(v) v f(T, v) dv \,, \tag{5.2}$$

where *f(T,v)* is the velocity distribution of participating particles at temperature *T*. Solution of equation (5.1) has the following form:

$$\frac{1}{n} = \frac{1}{n_0} + \alpha.t \,. \tag{5.3}$$

In plasma (afterglow) environments recombination is not the only loss process. Ambipolar diffusion with recombination on the walls of the apparatus and ion molecule reactions with other present species are also contributing to the overall deionization. Assuming cylindrical shape of the experimental apparatus the balance equation (5.1) can be rewritten for the general case to the following form:

$$\frac{dn}{dt} = -\alpha.n^2 - kn[\mathrm{B}] - \frac{D_a}{\Lambda^2} n \,, \tag{5.4}$$

where *k* is the rate coefficient of the ion molecule reaction with species *B*, D_a is the rate coefficient of ambipollar diffusion, Λ is the characteristic diffusion length that depends solely on the geometry and dimension of the apparatus in our case the discharge tube. Assuming that the number density of species B is much higher than the concentration of charged particles, then the ion molecule reaction channel is a first order process and can be treated together with the ambipolar diffusion

$$\frac{dn}{dt} = -\alpha.n^2 - \frac{n}{\tau} \,, \tag{5.5}$$

where

$$\frac{1}{\tau} = k[B] + \frac{D_a}{\Lambda^2} \,. \tag{5.6}$$

The solution of (5.5) has the following form

$$n(t) = \frac{1}{\alpha\tau(\exp t/\tau - 1) + \frac{1}{n_0}\exp t/\tau}. \tag{5.7}$$

For the curve fitting of experimental data the Levenberg–Marquardt algorithm (LMA) was used with the Equation (5.7) as the fit function. Since LMA finds only the local not global minima and depends on the starting parameters all measured decay curves were evaluated individually.

For the evaluation of H_3^+ recombination we have to consider that according to theoretical predictions the two recombining H_3^+ species (para and ortho) have at low temperatures significantly different recombination rate coefficients. If we assume that the imbalance in the para and ortho H_3^+ populations caused by different recombination rates is rapidly balanced by collision with H_2 then for the observed overall effective recombination rate coefficient we can write:

$$\alpha_{eff} = \left({}^{p}\alpha_{eff}\ {}^{p}f + {}^{o}\alpha_{eff}\ {}^{o}f\right), \tag{5.8}$$

where ${}^{p}\alpha_{eff}$ and ${}^{o}\alpha_{eff}$ are the effective recombination rate coefficients of para-H_3^+ and ortho-H_3^+ respectively at particular experimental conditions, ${}^{p}f$ and ${}^{o}f$ are the fractions of para-H_3^+ and ortho-H_3^+ states in the present H_3^+ population (${}^{p}f + {}^{o}f = 1$). From this it is clearly evident that if one would be able to obtain measurements of the effective recombination rate coefficient at two different fractions, at otherwise identical conditions, it would be possible to calculate the effective recombination rate coefficients of pure para-H_3^+ and ortho-H_3^+. As was already mentioned in chapter 2.6 the needed change of ${}^{p}f$ and ${}^{o}f$ can be achieved by using “para enriched H_2”.

In the actual experiments the evolution of absorption at the center of the absorption peak during the discharge cycle was observed. Since the temperature of ions and its evolution during discharge have been measured at the same or similar experimental conditions it was possible to recalculate the peak absorption evolution into number density evolution using **Equation 3.29** and coefficients summarized in **Table 3.2.**

In (5.8) effective recombination rate coefficients are used since both spin modifications are also subject to the ternary helium assisted recombination channel. To extract values of the binary recombination rate coefficient, that is measured in storage ring experiments and predicted in calculations, the dependence of the observed effective recombination rate coefficient on buffer gas density has to be measured. From this linear dependence the lower limit ([He] = 0) is the sought binary recombination rate coefficient.

In previous CRDS measurements of our group the initial part of the afterglow was included in the process of fitting. The rapid changes of concentration required an iterative approach to determine the evolution of RD transients in this region [65]. In this work more than 100 µs of afterglow were excluded form evaluation of the rate coefficient thus omitting the region with rapid number density changes. Comparing fits of several experimental datasets processed iteratively (method described in [65][66]) and in the standard way only a small difference was observed on the order

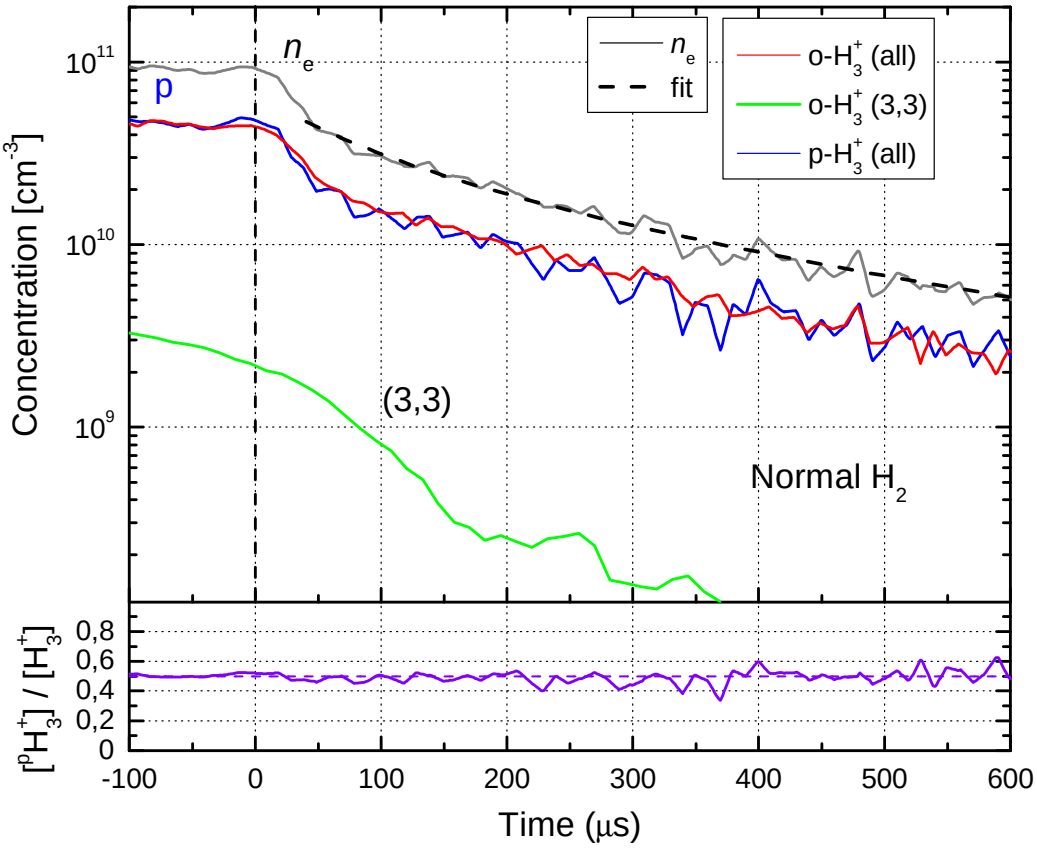

Figure 5.5 Example of measured decay curves in He/Ar/normal-H_2 discharge. Time zero is the end of discharge. Measurements were made at 77 K with [He] = cm^{-3}, [Ar] = cm^{-3}, [H_2] = cm^{-3}. Notice the constant fraction [$^pH_3^+$]/ [H_3^+].

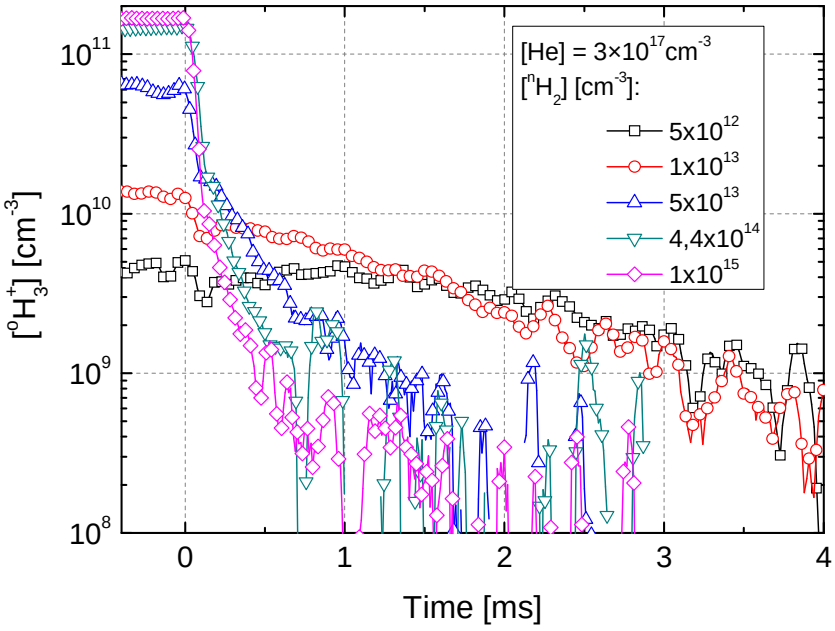

Figure 5.6 Examples of [$^{o}H_3^+$] decay curves measured at different [$^{n}H_2$] number densities and at fixed [He] = 2.7×10^{17} cm^{-3}. Buffer gas flow rates were in the range 700 – 1300 sccm

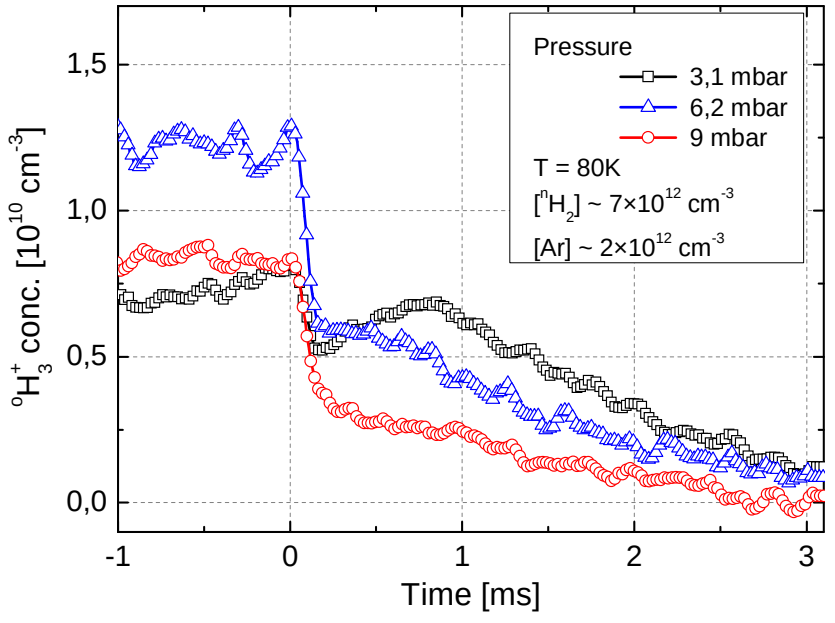

Figure 5.7. An example of [$^{o}H_3^+$] decay curves measured at different [He], and very low hydrogen density [$^{n}H_2$] = 7×10^{12} cm^{-3} and [Ar] = 2×10^{12} cm^{-3}.

of the confidence interval of the fit parameters. Considering the huge amount of raw data obtained, the time requirements of the iterative processing and the reasons mentioned above it was decided not to use iterative processing on the experimental data present in this work.

5.5 Measurements with normal H_2

As mentioned in the previous chapter both measurements using normal H_2 and para enriched H_2 are necessary for obtaining the spin specific recombination rate coefficients of para-H_3^+ and ortho-H_3^+. First the experiments using H_2 with normal (room temperature) distribution of spin states was used. This was a preferable start as it allowed to directly compare the results to previous experiments and because the used ortho-H_3^+ transition is roughly 3 times stronger so higher number densities of ortho-H_3^+ were desirable for a stronger signal. Before the actual measurements of state sensitive recombination of H_3^+ characterization of the produced plasma and afterglow was performed.

The observed absorption evolutions of both para-H_3^+ and ortho-H_3^+ have been calculated using spin specific coefficients from **Table 3.2**, yielding the number density evolutions of all para-H_3^+ and all ortho-H_3^+ states separately. The effective recombination rate coefficients for specific experimental conditions have been obtained by fitting the summed number density evolutions of para-H_3^+ and ortho-H_3^+. We assume that H_3^+ is the dominant ion and that this sum is equal to the electron density n_e. By summing the para and ortho H_3^+ evolutions the contributions to the decays from mutual para to ortho conversion in reaction with H_2 cancel each other out. At each set of experimental conditions both lowest rotational states have been probed in two succeeding measurements to minimize the influence of long term instabilities of the experimental apparatus that could not be controlled (i.e. laboratory temperature etc.). Example of number density evolution observed in discharge with normal H_2 is shown in **Figure 5.5**. This also provided the in situ para-H_3^+ /ortho-H_3^+ ratio for each set of experimental conditions (lower panel of **Figure 5.5**).

One of the goals was also to try to shed some light on H_3^+ ions present in the plasma and afterglow at low H_2 conditions (< 10^{13} cm^{-3}). Decay curves measured at various [$^nH_2$] are shown in **Figure 5.6**. One can see that with decreasing H_2 number density the number density of created H_3^+ ions is also decreasing. More importantly, at lower hydrogen concentrations the H_3^+ formation process still continues for a significant time into the afterglow. This formation process of H_3^+ in the afterglow at low H_2 conditions completely obscures the ongoing recombination in the time frame observable with the used apparatus. It is necessary to mention here that these findings do not contradict the measurements carried out at low H_2 concentrations in the FALP and AISA apparatus. In those experiments sufficiently long intervals (up to 60 ms for AISA and around 10 ms for FALP) of afterglow were left out of the evaluation in order to account for the slow formation of H_3^+.

One of the things one can do to speed up the formation of H_3^+ is increasing the number density of Ar. Unfortunately when concentration of Ar in the discharge was much higher then concentration of H_2, the discharge cell together with the high reflectivity mirrors of the CRD spectrometer exhibited a lasing behavior. The discharge produced a population inversion of a yet unspecified species of Ar that is usually quenched in collisions with H_2. The light produced by this process completely obscures the RD events and thus makes measurements impossible. Another option for H_3^+ formation speed up is to increase the buffer gas number density. As can be seen **Figure 5.7** increasing the number density of He has accelerated the H_3^+ formation. Nevertheless this was not enough to produce H_3^+ decays that could be reasonable fitted to Equation (5.7) to obtain the recombination rate coefficients. The upper limit for the buffer gas number density was given by the inability to produce stable microwave discharge conditions at elevated pressures. On the other hand at higher H_2 concentrations the decay curves do not exhibit any visible deviations from the expected curves produced by recombination coupled with diffusion of charged particles. The dependence of the number density of created ortho-H_3^+ ions in the discharge on the H_2 concentration is shown in **Figure 5.8**. The decreasing trend with lower H_2 number density suggests that H_3^+ is not the dominant ion in the discharge at low H_2 concentrations due to slow formation mentioned beforehand. Therefore valid recombination rate coefficient measurements can be obtained in the presented experiment only at sufficiently high H_2 number densities.

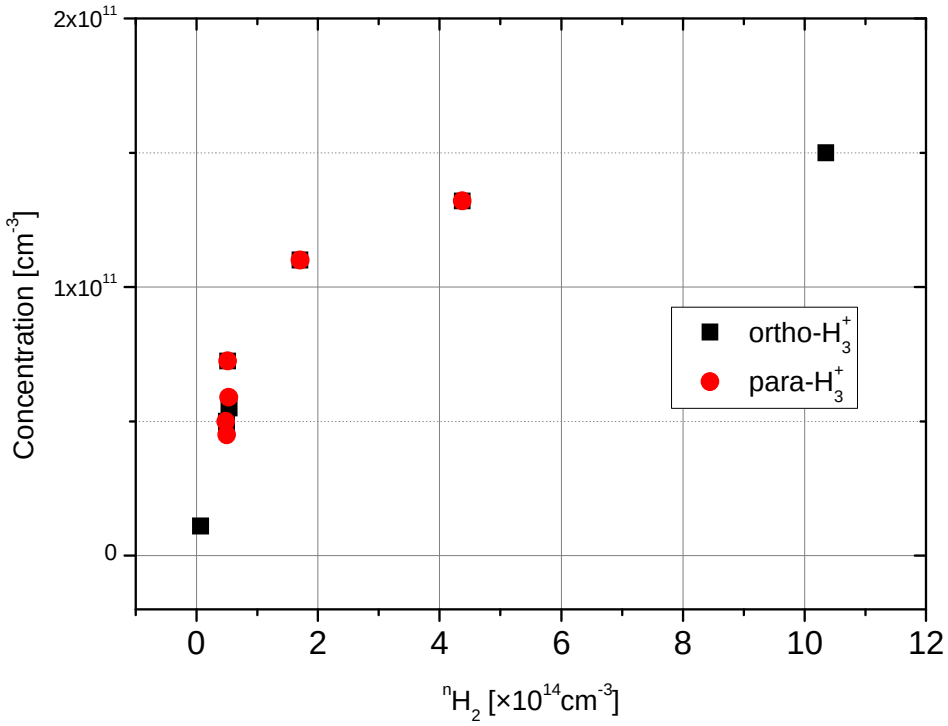

Figure 5.8 Concentrations of ortho and para H_3^+ as a function of normal-H_2 density.

At high H_2 concentrations ($>10^{15}$ cm^{-3}) the observed effective recombination rate coefficient increased which is in line with previous observations and it is attributed to the formation of the fast recombining H_5^+ ion. Therefore for the measurements of the dependence effective recombination rate coefficient on buffer gas density the H_2 concentrations were kept in the range $1\times10^{14} - 1\times10^{15}$ cm^{-3}.

The measurements in normal H_2 show among other things that the used number density of hydrogen in the conducted experiments is sufficient to keep the ratio of para to ortho H_3^+ states constant during afterglow. In other words the difference in recombination rate constant for different spin states is not big enough to bring the recombining plasma out of balance at the used conditions. The ratio of $^pH_3^+$ /$^oH_3^+$ during afterglow is given predominantly by the ratio of ortho and para states of the hydrogen reactant. It is worth noting that the discharge produces ortho H_2 and thus in the long term the ratio p/oH_3^+ moves to the thermal equilibrium value. This is countered by the short discharge time (~2ms) and a flowing gas mixture. Each subsequent breakdown of the discharge occurs in a "fresh" gas mixture with the same starting composition.

Measured effective recombination rate coefficients and their dependence on He number density are depicted in the upper panels of **Figure 5.14** and **Figure 5.15**, for 77 K and 140 K respectively. The results from measurements with normal H_2 have been fitted with a linear dependence to obtain the binary and ternary recombination rate coefficient of H_3^+ with thermal para and Ortho population distribution (^pf~0,5). The resulting recombination rate coefficients are $\alpha_{bin}(77\ K)= (1\pm0,2)\times10^{-7}$ cm^3s^{-1} for the binary channel and $K_{He}(77\ K) = (1,5\pm0,4)\times10^{-25}$ cm^6s^{-1} for the ternary both at 77 K. For 140 K the following values have been obtained, $\alpha_{bin}(140\ K) = (0,76\pm0,2)\times10^{-7}$ cm^3s^{-1} and $K_{He}(140\ K) = (2,2\pm0,4)\times10^{-25}$ cm^6s^{-1} for the binary and ternary recombination channel respectively. These values are depicted together with theoretical predictions, values from storage ring experiments and binary channel values obtained from Langmuire probe utilizing afterglow experiments in **Figure 5.16.** It is appropriate to point out here the outstanding agreement of the measured binary recombination rate coefficient of various afterglow experiments between each other. This agreement is achieved despite different geometry, diagnostic tools and time frames of afterglow observation of the various experimental apparatuses used (FALP, AISA, MDT-CRDS). This is a very strong argument suggesting that no systematic errors are present and supports the validity of the obtained results. The slight disagreement with values obtained in CRYRING storage ring experiments is still an open question. One of the possible explanations for this discrepancy could be the high rotational excitation (>400 K) reported for the experiments on the TSR apparatus [55][130]. The authors suggest that same conditions apply for the CRYRING facility also.

5.6 Measurements with para enriched H_2

As the next step in the effort to obtain spin state specific recombination rate coefficients using (5.8 experiments using hydrogen with an enriched population of para spin symmetry states (compared to normal-H_2). Para enriched H_2 was created using the so-called "*para generator*" described in chapter 4.5. It uses a closed cycle helium cryostat to cool a suitable catalyst in a conversion chamber to 10 K. When hydrogen passes through the conversion chamber the low temperature and present catalyst allows almost all molecules to settle in the lowest available rotational state. This state has para spin symmetry. After leaving the conversion chamber higher rotational states are repopulated but without the presence of the catalyst the molecules are unable to change their nuclear spin.

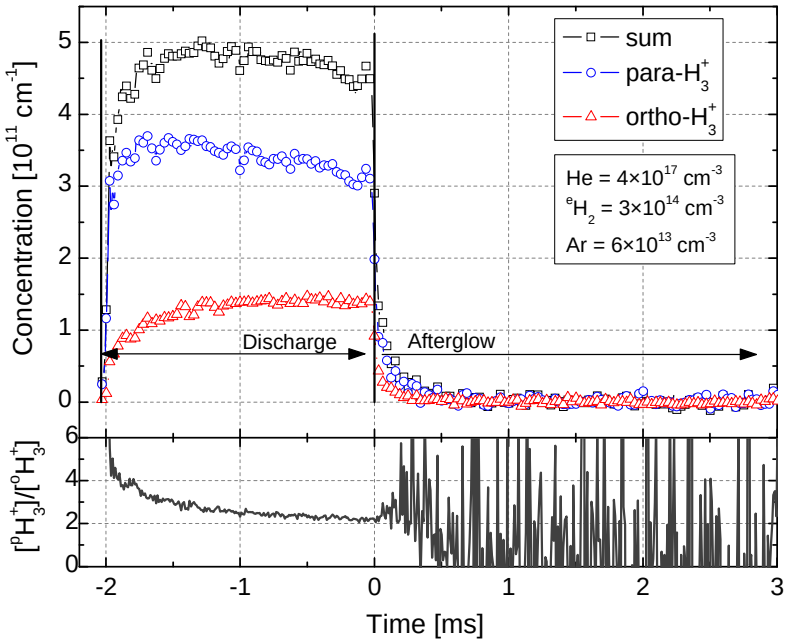

Figure 5.9 Example of observed number density evolution during the discharge cycle when para enriched H_2 was used as precursor. Significant enrichment of paraH_3^+ is clearly visible.

For the H_3^+ formation at various conditions the same discussion as for measurements in normal H_2 applies. Conditions at which reliable decay curves for recombination measurements were obtained are the same is with normal H_2. Also, due to experimental constraints (i.e. design of para generator) the lowest usable concentration of enriched H_2 in the discharge tube was 3×10^{13} cm^{-3}.

As in experiments with normal H_2 the observed temperature of H_3^+ ions was close to the buffer gas and wall temperature of 77 K when cooled with LN_2. Therefore we assumed the same thermo-dynamical conditions as beforehand, i.e. thermal rotational distribution for each spin manifold but a non-thermal overall ratio

of populated para and ortho H_3^+ nuclear spin states. For 140 K measurements the temperature was determined solely from the Doppler broadening of the observed absorption lines.

Example of observed number density evolution during the discharge cycle is depicted in **Figure 5.9**. Significant enrichment of para H_3^+ states was observed when para enriched hydrogen was used as precursor. The para to ortho H_3^+ ratio slowly evolves during the afterglow but after roughly ~1,5 ms into the discharge reaches equilibrium. During the afterglow the slow ratio change can not keep up with the fast number density drop due to recombination and the para/ortho ratio can be considered constant. A detailed look at the afterglow part of the decay curves confirms this assumption, see **Figure 5.10**. Therefore for further calculations a single number was used to represent the p/oH_3^+ ratio at specific conditions.

The observed equilibrium ratio of para/ortho H_3^+ states at the end of the discharge is a function of experimental parameters. In **Figure 5.11** the dependence of this ratio as a function of $^pH_2$ number density is depicted. The observed dependence can be roughly explained the following way. From $^pH_2$ predominantly $^pH_3^+$ is created that is in subsequent collisions with H_2 converted to $^oH_3^+$. At lower H_2 concentrations this conversion is less effective therefore higher fractions of $^pH_3^+$ are observed. Detailed numerical studies of these processes are under way.

Adding normal H_2 to the discharge tube during the experiment with enriched H_2 it is possible to produce reactant hydrogen gas with an almost arbitrary ratio of para to ortho states. The range of attainable para H_2 fractions is from 0,25 for normal H_2 to 0,87 (given by the para generator efficacy) for enriched H_2. Dependences of the equilibrium p/o H_3^+ ratio on the para/ortho composition of reactant H_2 at different experimental conditions are shown in **Figure 5.12**. For these measurements normal H_2 was added to the discharge with a constant flow of enriched H_2. The first measurement point was taken with only enriched H_2. Then normal H_2 was added in increasing flows. For the last measuring step the enriched H_2 inlet was shut off and only normal H_2 was present.

Just by comparing decay curves obtained at identical conditions with $^nH_2$ and $^eH_2$ it is evident that recombination is faster when $^eH_2$ is used as a reactant. In **Figure 5.13** the evolution of inverse number density of the decay curves is plotted together with the fits of the decay curves that demonstrate the recombination rate increase.

The measured effective recombination rate coefficients with enriched H_2 as a dependence on buffer gas number density are show in the upper panels of **Figure 5.14** and **Figure 5.15** for 77 K and 140 K respectively. Recombination rate coefficients measured with normal H_2 are also shown. For each of the measurements

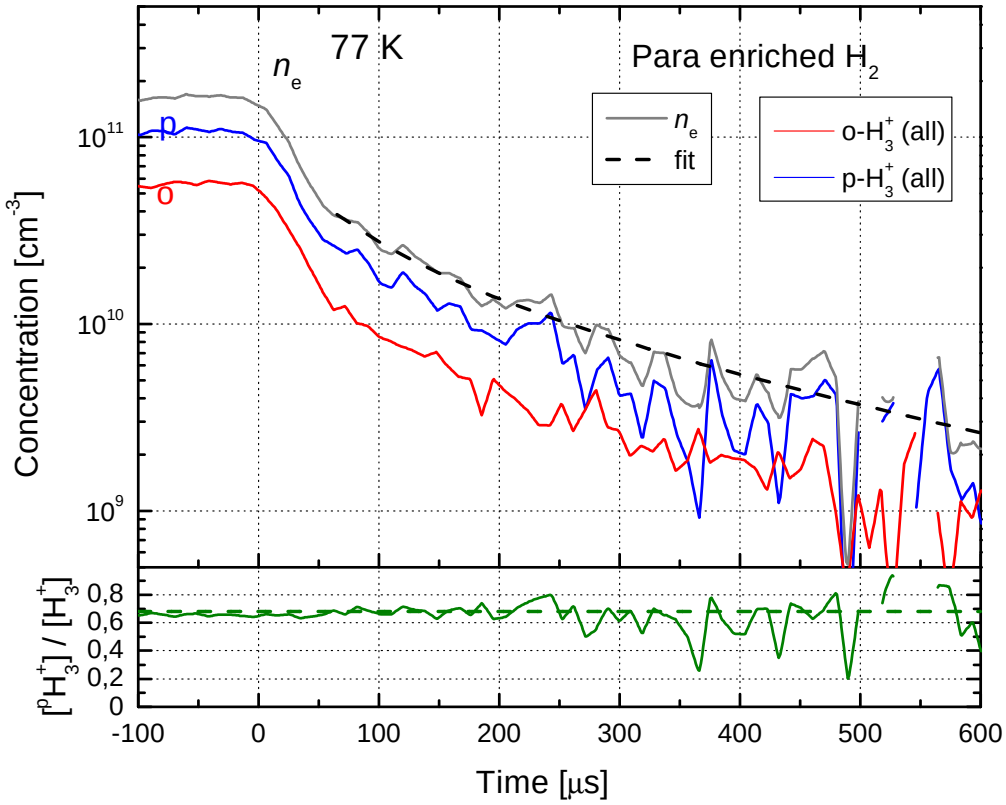

Figure 5.10 Example of observed decay curves during afterglow. Significant para H_3^+ enrichment and a stable para / ortho H_3^+ ratio were observed (for comparison see **Figure 5.5**)

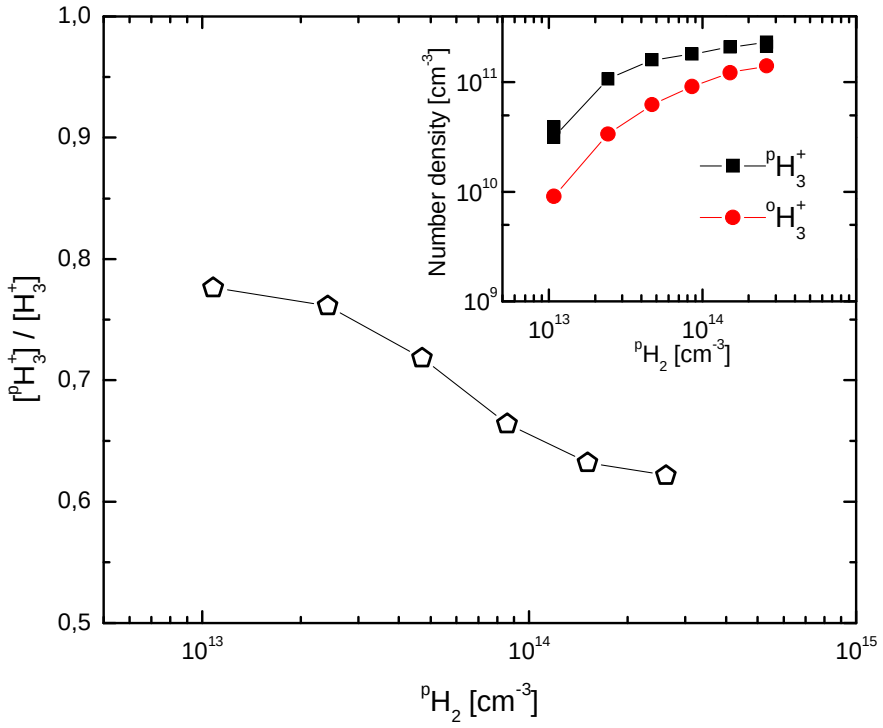

Figure 5.11 Dependence of the $[^pH_3^+]/[H_3^+]$ fraction on $^eH_2$ number density. Buffer gas density ~2×10^{17}cm^{-3}, He flow 1030 sccm, [Ar] ~ $[^eH_2]$

For the calculation of effective recombination rate coefficients of pure para and ortho H_3^+ instead of the experimental data obtained with normal H_2 the analytical formulas for the ternary dependence of effective recombination rate coefficient on He with above mentioned coefficients were used. From effective recombination rate coefficients measured with enriched H_2 the effective recombination rate coefficients of pure para-H_3^+ and ortho-H_3^+ has have been calculated. This was done by taking the effective recombination rate coefficient values from the analytical expression of measurements with normal H_2, observed para-H_3^+ fractions (^pf) for measurements with normal H_2 and enriched H_2 and the measured effective recombination rate coefficient measured with enriched H_2. The resulting rate coefficients are summarized in **Table 5.4** and are depicted in **Figure 5.16**. The results show a remarkable agreement with theoretical predictions and confirm the qualitative results obtained in storage ring experiments [53][54][55]. But unlike storage ring experiments here is the internal excitation and nuclear spin composition as well as temperature of the recombining ions monitored in situ with a much better control giving the results a higher relevance. The major down side is that the performed experiments do not allow for the extraction of the dependences of recombination cross section on energy that could be used in advance studies for environments where a single thermodynamic temperature can not be easily applied. The results obtained at 77 K were already published, see attached publication II

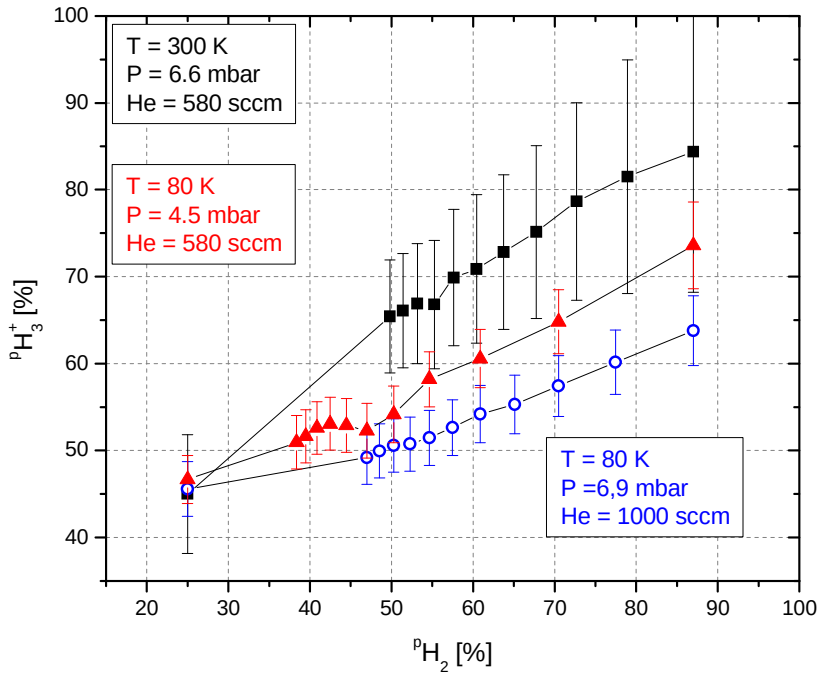

Figure 5.12 Dependence of the [$^{p}H_3^+$] fraction on para enrichment of H_2 at various conditions.

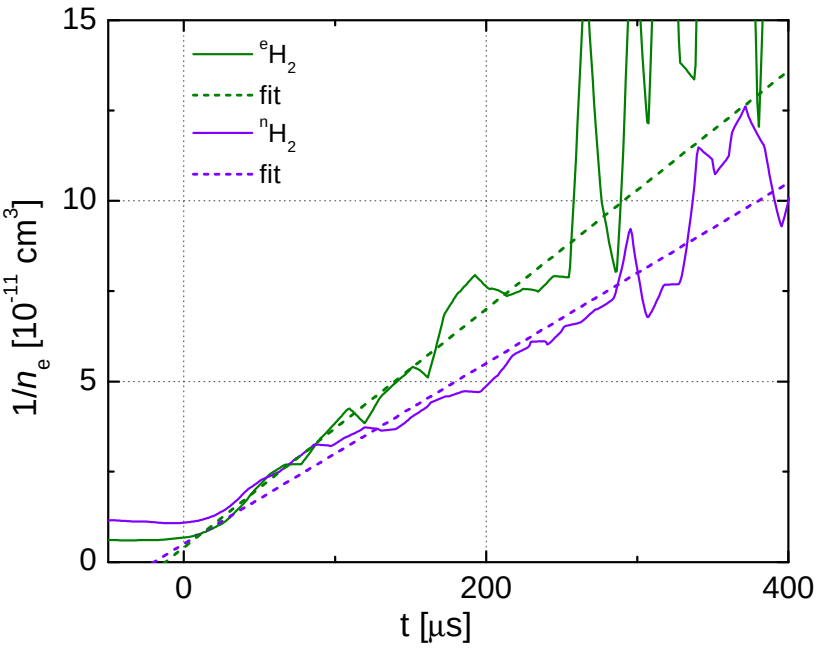

Figure 5.13 Evolution of the reciprocal number density ($1/n_e$) during afterglow when using normal H_2 and enriched H_2 at otherwise identical conditions.

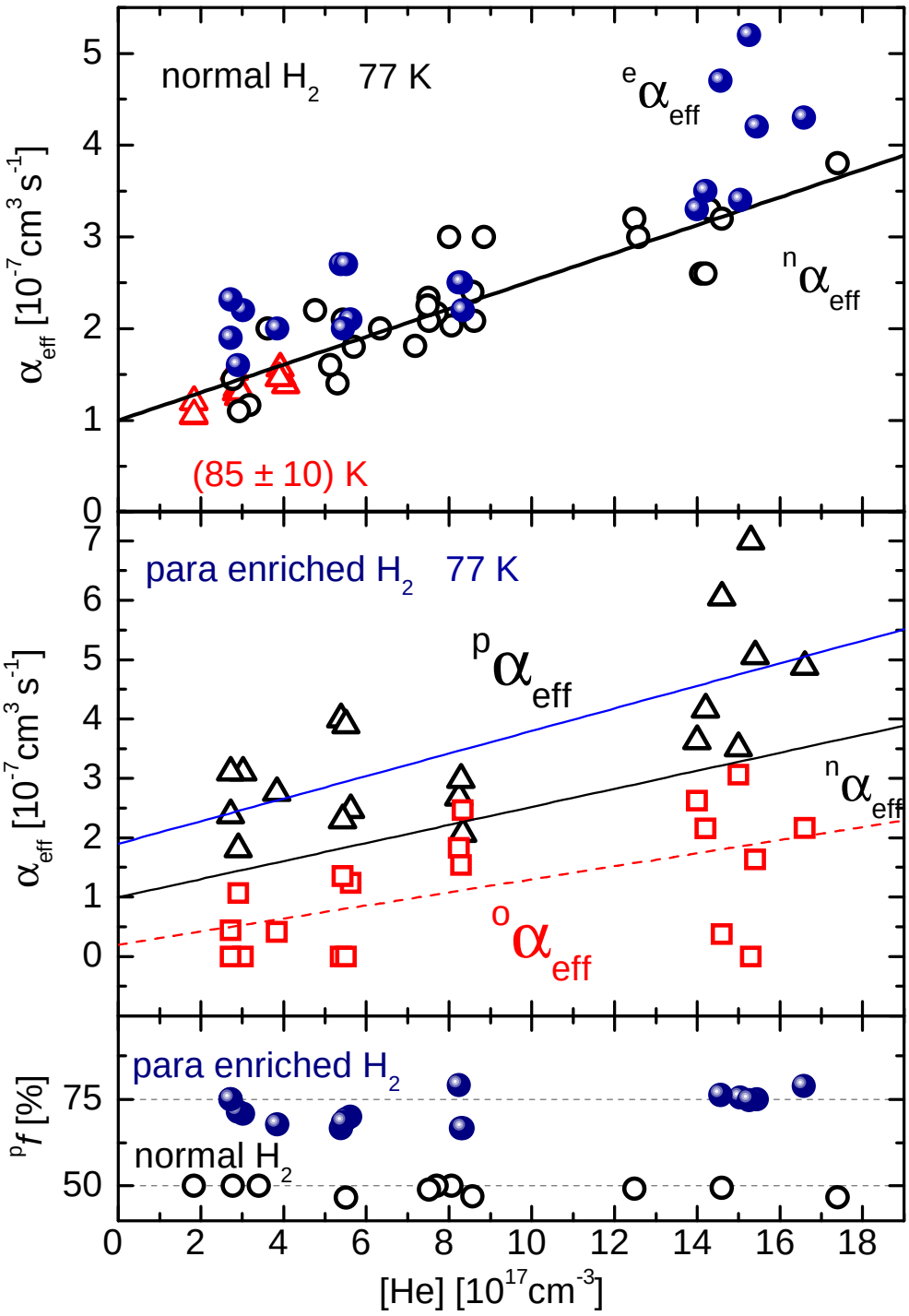

Figure 5.14 Obtained effective recombination coefficients and their dependence on He density at 77 K. Upper panel displays the values obtained using n-H_2 as precursor (empty circles) together with values obtained with FALP at 77 K(red triangles) and values obtained using $^{e}H_2$ (blue circles). Middle panel shows the extrapolated values for pure para-H_3^+ and ortho-H_3^+. Lower panel shows the ^{p}f fraction of para-H_3^+ for the measurements shown in upper panels.

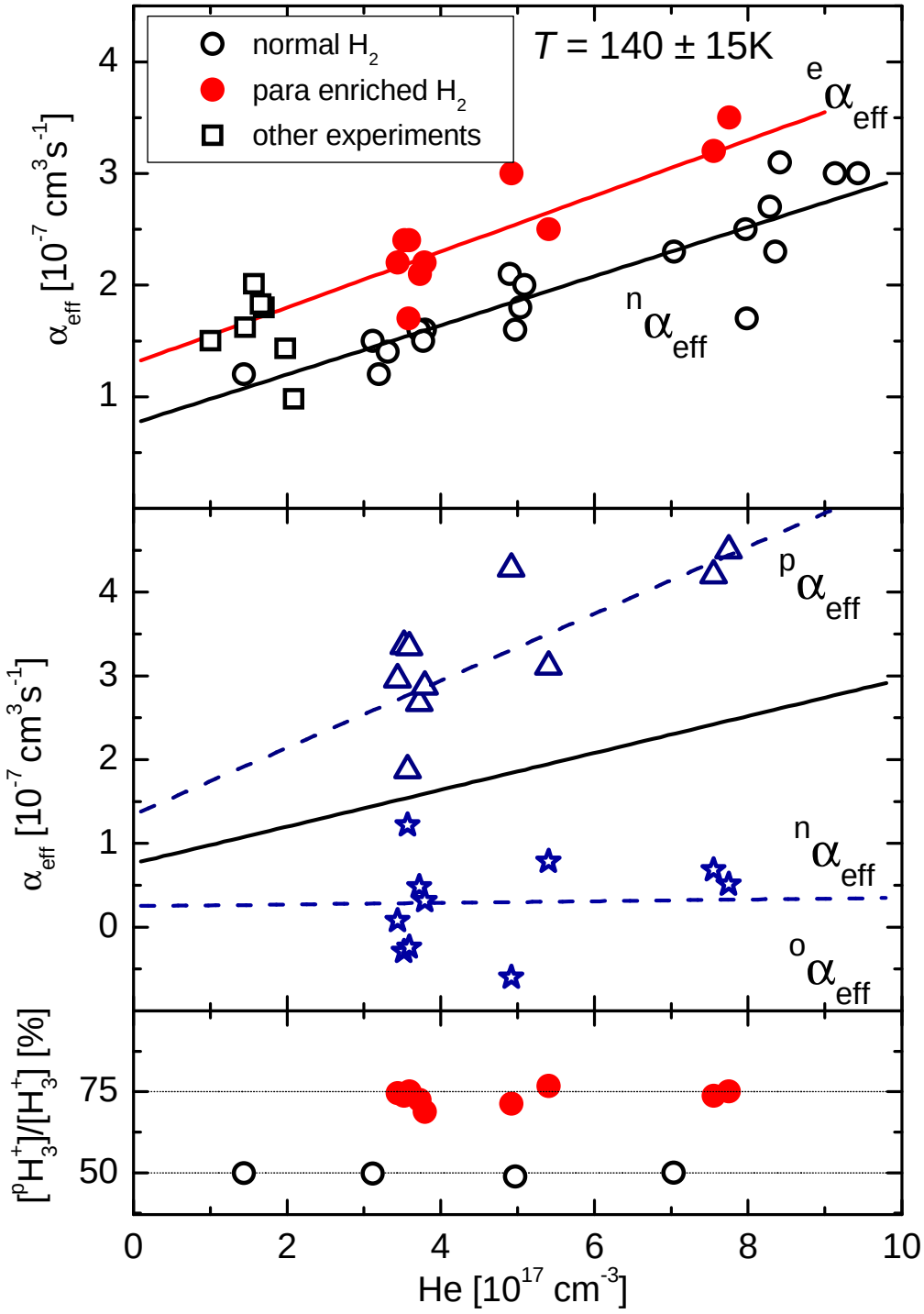

Figure 5.15 Obtained effective recombination coefficients and their dependence on He density at 140 K. Upper panel displays the values obtained using n-H_2 as precursor (empty circles) together with values obtained using $^{e}H_2$ (red circles). Middle panel shows the extrapolated values for pure para-H_3^+ and ortho-H_3^+. Lower panel shows the ^{p}f fraction of para-H_3^+ for the measurements shown in upper panels.

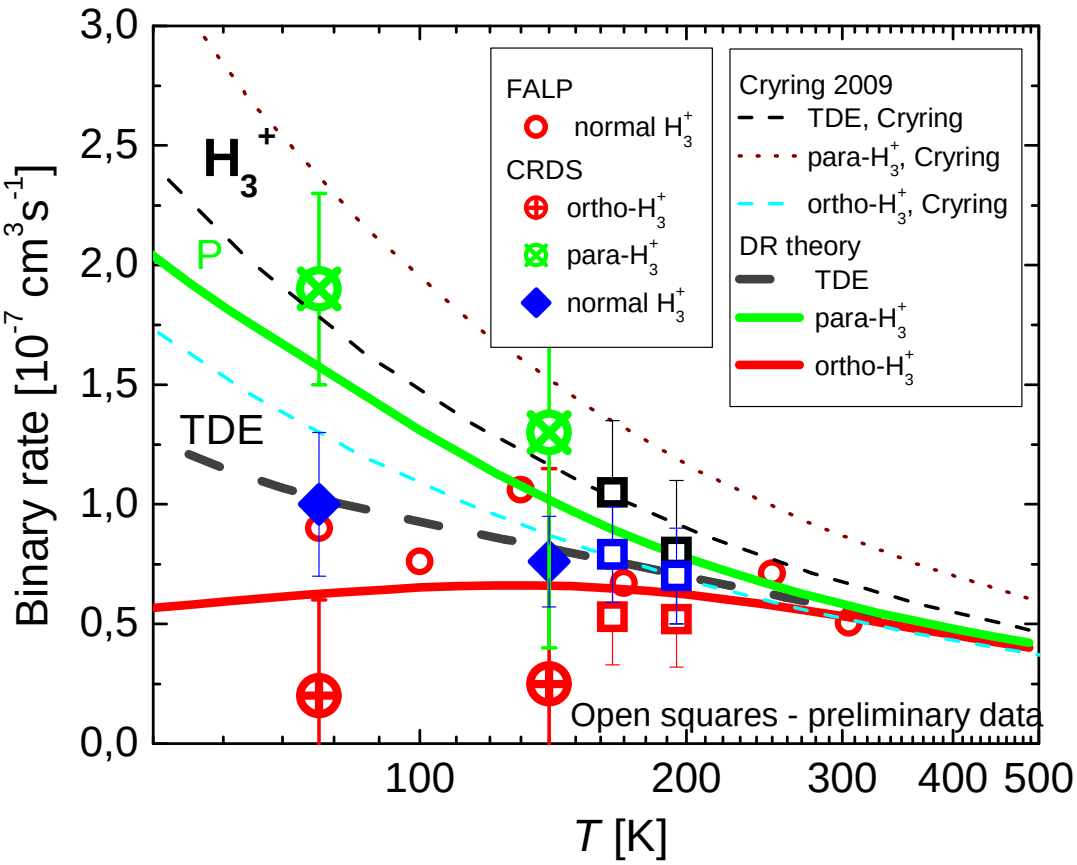

Figure 5.16 Summary of measured and calculated binary recombination rate coefficients in comparison with other experimental results and theoretical predictions. Also included are preliminary data from ongoing work at other temperatures [131]

spin (temperature)	α_{bin}[cm^3s^{-1}]	α_{bin} error [cm^3s^{-1}]	K_{He}[cm^6s^{-1}]	K_{He} error [cm^6s^{-1}]
para(77 K)	$1{,}9\times10^{-7}$	$0{,}4\times10^{-7}$	$1{,}9\times10^{-25}$	$0{,}44\times10^{-25}$
orho(77 K)	$0{,}2\times10^{-7}$	$0{,}4\times10^{-7}$	$1{,}1\times10^{-25}$	$0{,}4\times10^{-25}$
para (140 K)	$1{,}3\times10^{-7}$	$0{,}9\times10^{-7}$	4×10^{-25}	1×10^{-25}
ortho (140 K)	$0{,}25\times10^{-7}$	$0{,}9\times10^{-7}$	$0{,}1\times10^{-25}$	1×10^{-25}

Table 5.4 Extrapolated values of the recombination rate coefficients for pure para-H_3^+ and ortho-H_3^+ for the binary channel (α_{bin}) and ternary channel (K_{He}).

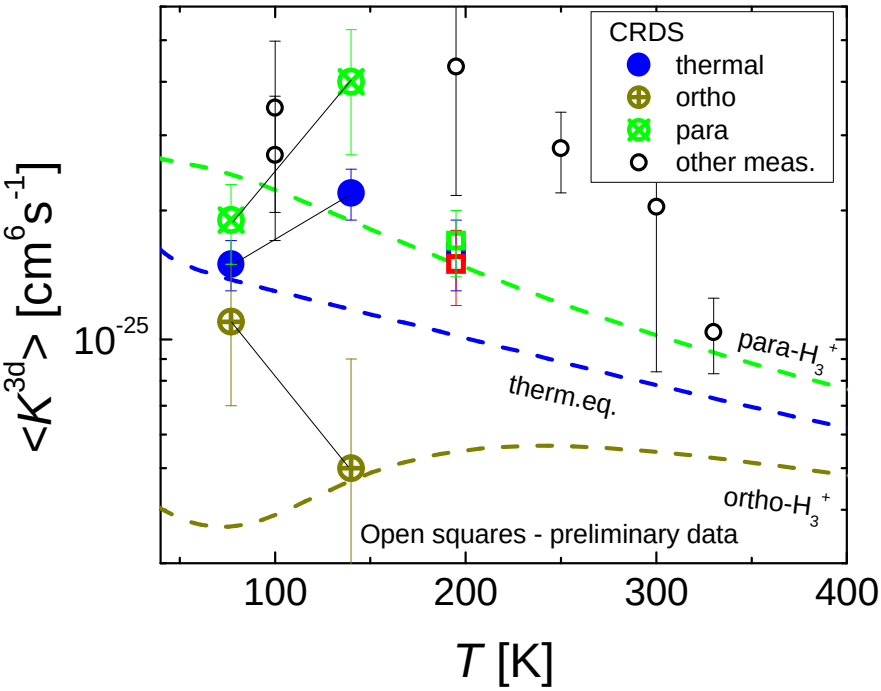

Figure 5.17 Summary of measured and calculated ternary recombination rate coefficients in comparison with other experimental results and theoretical predictions. Included are preliminary data from ongoing work [131]

6 Summary

This thesis summarizes some of the experimental work the author performed during his doctoral studies. The main topic is the determination of spin state specific recombination rate coefficient of the para and ortho nuclear spin symmetry modifications of the ion H_3^+.

Time resolved near infrared continuous wave Cavity ring down spectroscopy was used as the diagnostic tool to observe time evolutions of absorption lines of H_3^+ ions produced in a He/Ar/H_2 gas mixture discharge.

Measurements using normal H_2 as a reactant extended the range of conditions at which measurements using CRDS were performed in previous studies (see e.g. [Attached publication V]). The modified discharge tube and cooling design allowed reaching lower temperatures of studied ions than in previous CRDS studies. The effort to observe recombination of H_3^+ at low H_2 concentrations (~10^{12} cm^{-3}) was not successful due to slow formation of the H_3^+. At these conditions H_3^+ becomes the dominant ion only after several ms. By this time the number density of charged particles decayed below the limit observable with the used apparatus. So the question of internal excitation of H_3^+ ions at these conditions remains still open. At proper conditions ([He]~ 1 - 15×$10^{17}$$cm^{-3}$; [Ar] ~1×$10^{15}$$cm^{-3}$; [$H_2$]~2 - 8×$10^{14}$$cm^{-3}$) the observed effective recombination rate coefficients are in agreement with previous works. The recently discovered Helium assisted ternary recombination [Attached publication II, III and IV] has been observed at all temperatures. From the dependence of the effective recombination rate coefficient on buffer gas number density the following recombination rate coefficient values have been obtained $\alpha_{bin}(77\ K)= (1\pm0,2)\times10^{-7}\ cm^3s^{-1}$ for the binary channel and $K_{He}(77\ K) = (1,5\pm0,4)\times10^{-25}\ cm^6s^{-1}$ for the ternary channel both at 77 K. For 140 K the following values have been obtained, $\alpha_{bin}(140\ K) = (0,76\pm0,2)\times10^{-7}\ cm^3s^{-1}$ and $K_{He}(140\ K) = (2,2\pm0,4)\times10^{-25}\ cm^6s^{-1}$ for the binary and ternary recombination channel respectively.

As is summarized in Chapter 2.6 in order to achieve a change of the para/ortho H_3^+ states ratio H_2 with an enriched population of para states has been used. The creation of enriched H_2 was facilitated by the so called “para generator”. This device has been designed and built in our laboratory. It utilizes a closes circle helium cryostat to cool a conversion chamber containing a suitable paramagnetic catalyst to 10 K. At this low temperature majority of H_2 molecules should be in the lowest ro-vibrational state that has para nuclear spin symmetry. But without the presence of the catalyst the molecules are unable to change their nuclear spin state and retain their room temperature para/ortho states ratio. After exposing the

molecules to the catalyst at low temperatures they are again heated up without the catalyst so the low temperature para/ortho ratio is retained. This gas is then used as precursor for creation of H_3^+ ions.

Using para enriched H_2 as a precursor for creating H_3^+ resulted in the creation of H_3^+ with significantly non-thermal ratio of populated rotational states with para and ortho nuclear spin symmetry. Effective recombination rate coefficients were measured in the same range of experimental conditions as in experiments with normal H_2. Using measurements with $^nH_2$ as a reference effective recombination rate coefficients of pure para-H_3^+ and ortho-H_3^+ were obtained. Dependences of the obtained effective recombination rate coefficients on buffer gas number density were used to extract values of the binary and ternary recombination rate coefficient for both nuclear spin states. The results are summarized in the **Table 5.4** (reprinted below) and depicted in **Figure 5.16** and **Figure 5.17**. The full potential of the apparatus has not been exhausted. At many temperatures only basic measurements were performed. Thorough measurements of the recombination rate constant at more temperatures besides the two presented here can and will be performed in future studies. Measurements at 77 K have been already published [Attached publication I]. Measurements and data processing for other temperatures is underway.[131]

spin (temperature)	$\alpha_{bin}[cm^3s^{-1}]$	α_{bin} error $[cm^3s^{-1}]$	$K_{He}[cm^6s^{-1}]$	K_{He} error $[cm^6s^{-1}]$
para(77 K)	$1{,}9\times10^{-7}$	$0{,}4\times10^{-7}$	$1{,}9\times10^{-25}$	$0{,}4\times10^{-25}$
orho(77 K)	$0{,}2\times10^{-7}$	$0{,}4\times10^{-7}$	$1{,}1\times10^{-25}$	$0{,}4\times10^{-25}$
para (140 K)	$1{,}3\times10^{-7}$	$0{,}5\times10^{-7}$	4×10^{-25}	$1{,}3\times10^{-25}$
ortho (140 K)	$0{,}25\times10^{-7}$	$0{,}5\times10^{-7}$	$0{,}5\times10^{-25}$	$0{,}4\times10^{-25}$

Table 5.4 Extrapolated values of the recombination rate coefficients for pure para-H_3^+ and ortho-H_3^+ for the binary channel (α_{bin}) and ternary channel (K_{He}).

The results show a remarkable agreement with theoretical predictions and confirm the qualitative results obtained in storage ring experiments. But unlike storage ring experiments here the internal excitation and nuclear spin composition as well as temperature of the recombining ions is monitored in situ with a much better control, giving the results a much higher relevance. The major down side is that the performed experiments do not allow for the extraction of the recombination cross section energy dependences that could be used in advanced studies for environments where a single thermodynamic temperature can not be easily applied.

Appendix A

Optical setup procedure and tuning

Although the act of physically setting up the components of a CRDS spectrometer is an easy task for an experienced user it can be a daunting almost impossible task for an inexperienced student. The purpose of this chapter is to give a helping hand to inexperienced user by pointing out some important practical details that are usually left out in other written publications.

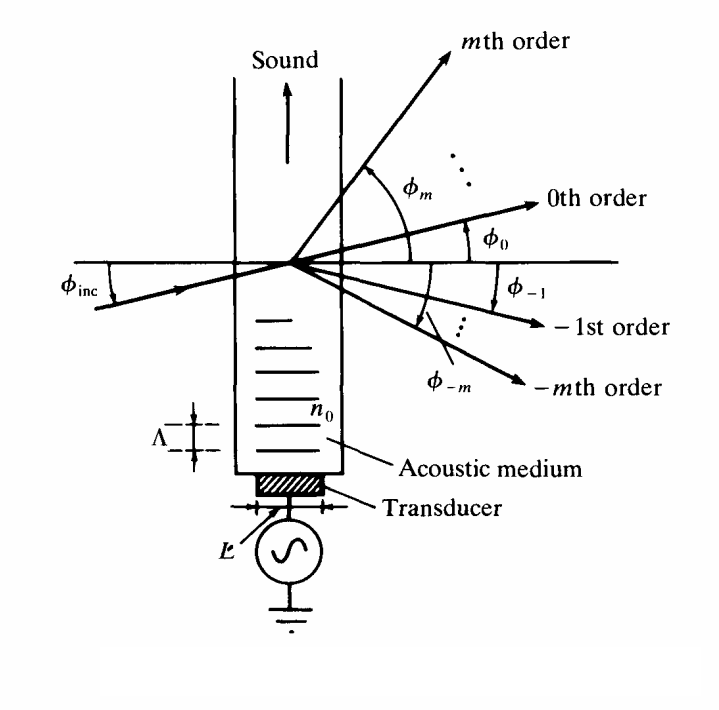

Figure A.1 AOM principle reprinted from [132]

First the laser collimator is placed on the breadboard. It is advisable to make sure that the collimated beam is parallel with the breadboard.

Next step is the optical isolator. Placing it in an appropriate holder assures that its optical axis is parallel with the breadboard. Tuning the optical isolator consists of two steps. First the isolator is places in the reverse direction. The whole isolator is the turned to the position where the reverse transmitted power is maximal. Then the isolator is adjusted via the tuning slot to minimize the reverse transmission. Then the isolator is placed in the forward direction and turned so that maximum

intensity transmission is achieved. This way, back-reflection attenuations of a factor ~2000 are commonly achieved.

Next step in the build up is the Acousto-optical modulator (AOM). First it is crucial to check hove big is the active region of the AOM. Larger beam diameter results in inefficient diffraction, thus effectively loss of intensity, and beam deformation that result in further intensity loss on the spatial filtering optics. When the laser beam is larger a beam shrinking telescope is required to achieve optimum performance of the AOM. When placing the AOM in the laser beam path (with an appropriate waist size) one needs to remember that unlike with optical gratings, the diffraction of the laser light on the standing acoustic wave inside the AOM occurs ONLY if the laser hits the AOM under an specific incidence angle. The precise value of this angle is different for particular devices, depending on the construction and wavelength, and is usually stated in the datasheet. By coarse turning of the AOM in ON state in the laser beam path by hand, a position in which the diffraction occurs has to be found. Then by fine-tuning the orientation of the AOM the intensity of the 1^{st} order of diffraction is maximized. Depending on the particular model of AOM up tu 87% of light intensity can be allocated to the 1^{st} diffraction order.

The spatial filtering components placement follows the AOM. The first lens can be placed at an arbitrary distance (down the beam path). But one has to remember that at some wavelengths, especially in the near infrared region, absorption from water vapor in air can lead to a significant loss of intensity thus long distances between components are better avoided. The pinhole is mounted on an XYZ mount. The pinhole is initially placed closer to the lens then the focus so the laser cone is significantly larger then the pinhole so a small part of the intensity is transmitted. This small signal is maximized in the XY plane (perpendicular to the beam) then the pinhole is moved closer to the focal point in the Z plane and the process is repeated. This iterative procedure is a reliable way of finding the optimal placement of the pinhole. The second lens is the one shaping the beam into the required form. Its position is determined by the resonator parameters, its focal length and distance of the pinhole from the optical cavity. For the calculation of the proper placement see the calculation in [1]

After the spatial filtering and mode matching at least two more adjust mirrors are necessary to facilitate proper beam steering into the optical cavity. Because experiments are performed with infrared lasers a red He-Ne laser is used for coarse adjusting. A mirror on a flip mount in the path of the IR laser is used to place the He-Ne laser on the same optical path as the IR laser. To laser beams are on the same path if they share two separate points in space along their path with no mirrors in between. First the IR laser is deflected on a sufficiently long path where the beam

[1] Morville J. Doctoral thesis: *Injection des cavités de haute finesse par laser a diode - Application a la CW-CRDS et a la détection de traces atmospheriques,* Grenoble 2001

overlap will be controlled. The longer the path the better the overlap can be controlled. A small aperture (iris blend) is placed in the IR laser path as the first point. Further along the IR lasers path as far away as practically possible from the first one the impact point of the IR laser is recorded. Through these two points in space (iris blend and the impact point) the He-Ne laser has to be directed by adjusting the mirror on the flip mount and at least one another steering mirror.

Next steps are performed with the HeNe laser. First step is to make sure that the HeNe laser passes the center of both high reflectivity mirrors of the optical cavity and at the same time falls completely on the detector focusing lens on the rear side of the optical cavity. This is very crucial because if only a part of the laser is hitting the detector lens the RD intensity will suffer thus decreasing the SNR. Next step is to locate the back reflections of the He-Ne laser from the detector side mirror. To observe the back reflections a white paper with an appropriate aperture is best used. The aperture should be just big enough to let the laser beam pass undisturbed but not any bigger as this would lower the precision of the adjustment. The paper is placed in the beam path after the mode-matching lens. When searching for the rear mirror back reflections it is advisable to tilt the first cavity mirror so that the reflections from it do not fall on the paper. This way, when the detector side cavity mirror is tilted the observed reflections on the paper are only due to the movement of this mirror. The coarse adjustment of the detector side cavity mirror is finished when the back reflection from that mirror falls right on the papers aperture. Then the first cavity mirror is tilted so that the reflection from it also falls on the aperture. After this procedure both mirrors are very close to the optimal position. When the flip mounted mirror is moved so that the IR laser can shine on the optical cavity the cavity ring-down events should be observable right away if the cavity length is already swept.

The following fine tuning of the optical cavity is then performed with an oscilloscope. The goal of this fine tuning is to obtain single mode excitation of the optical cavity. After a strong enough RD signal is attained the cavity has to be aligned for best performance. This is accompanied by tilting of the cavity mirrors that effectively changes the Finesse of the cavity and thus the decay time of the observed RD events. Proper aligment of the cavity mirrors is for achieved by maximizing the observed RD decay time. Since moving of the cavity mirrors effectively changes the position of the whole cavity in space, further alignment of laser beam is necessary to again achieve selective single mode excitation of the cavity. These two steps have to be performed in several iterations to achieve optimal performance.

When performing this step one has to pay attention to the direction of the laser exciting the optical cavity. Observed mode structure and ring down times depend only on the laser and cavity alignment. Since the resonator mirrors are spherical the iterative tuning can lead to the situation where the laser diverges from

the apparatus axis and no longer falls on the detector collecting lens, or falls on it only partially. This is signalized by decreasing maximum observable intensity of the RD transients after each tuning iteration. Therefore, the detector position has to be adjusted and maximum RD intensity checked during each step.

References

[1] Thomson J.J., Rays of positive electricity, *Phil. Mag.* **21**, 1911, 225–249.

[2] Thomson J.J., Further experiments on positive rays, *Phil. Mag.* **24**, 1912, 209–253.

[3] Dempster A. J., *Phil. Mag.*, **31**, 1916, 438,.

[4] Hogness T. R. & E. G. Lunn: *Phys. Rev.* **26**, 44, 1925.

[5] Oka T.: The H^+ ion. In Molecular ions: spectroscopy, structure and chemistry, edited by T. A.Miller & V. E. Bondybey, Amsterdam: North Holland, **73**, 1983.

[6] Bowers, M. T., Elleman, D. D., Jr,. Analysis of the Ion-Molecule Reactions in Gaseous H_2, D_2, and HD by Ion Cyclotron Resonance Techniques. *The Journal of Chemical Physics* **50** (11), 1969, 4787-4804.

[7] Coulson, C. A.: Proc. Camb. *Phil. Soc.*, **31**, 244, 1935.

[8] Christoffersen, R. E., Hagstrom, S., Prosser, F., H_3^+ Molecule Ion. Its Structure and Energy. *The Journal of Chemical Physics* **40** (1), 1964, 236-237.

[9] Gaillard M. J., D. S. Gemmel, G. Goldring, I. Levine and B. J. Zabransky: *Phys. Rev. A*, **17**, 1797, 1978.

[10] Martin D. W., E. W. McDaniel, & M. L. Medka: *Astrophys. J.*, **134**, 1012, 1961.

[11] Herbst E. & W. Klemperer*: Astrophys. J.*, **185**, 505, 1973.

[12] Watson W. D.: Astrophys. J., 183, L17, 1973.

[13] McCall, B. J., Dissociative recombination of cold and its interstellar implications. *Physical and Engineering Sciences* **364** (1848), 2006, 2953-2963.

[14] Herbst, E., The astrochemistry of H_3^+. Mathematical, *Physical and Engineering Sciences* **358** (1774), 2000, 2523-2534.

[15] Geballe, T. R., H_3^+ between the stars. Mathematical, *Physical and Engineering Science*s **358** (1774), 2000, 2503-2513

[16] Oka, T.,. Observation of the infrared spectrum of H_3^+. *Phys. Rev. Lett.* **45**, (1980) 531-534.

[17] Trafton L.M., D.F. Lester, and K.L. Thompson: *Astrophys. J.*, **343**, L73, 1989.

[18] Trafton L. M., T. R. Geballe,. S. Miller, J. Tennyson, G. E. Ballester: *Astrophys J*, **405**, 761, 1993.

[19] Geballe T. R., M.F. Jagod, , T. Oka: *Astrophys J.*, **408**, L109, 1993.

[20] Miller S., T. Stallard, C. Smith, G. Millward, H. Melin, M. Lystrup, & Aylward: *Phil. Trans. R Soc A.*, **364**, 3121, 2006.

[21] Geballe, T. R., Oka, T., Detection of H_3^+ in interstellar space. *Nature* **384** (6607), 1996, 334-335.

[22] McCall, B. J., Geballe, T. R., Hinkle, K. H., Oka, T., Detection of H3+ in the Diffuse Interstellar Medium Toward Cygnus OB2 No. 12. *Science*, **279** (5358), 1998, 1910-1913.

[23] Leu M. T., Biondi M. A. and Johnsen R., *Phys.Rev. A*, **8,** 413, 1973

[24] Peart B., Doder K., *J. Phys. B.*, **7**, 1948, 1974

[25] Auerbach D., R. Cacak, R. Caudano, T. D. Gaily, C. J.Keyser, J. Mc Gowan, J. B. A. Mitchell and S.F.J. Wilk: *J. Phys. B.*,**10**, 3797, 1977

[26] Mathur D., Khan S. U. and Haste J. B., *J. Phys. B*, **11**, 3615, 1978.

[27] McGowan J.W., Mul P., D`Angelo V.S., Mitchell J.B.A., Defrance P. and Froelich H., *Phys. Rev. Letters*, **42**, 373, 1978.

[28] Adams N.G., Smith D. and Alge E., *J. Chem. Phys*., **81**, 1778, 1984.

[29] Mac Donald J.A., Biondi M.A. and Johnsen R., *Planet Space Sci.*, **32**, 651, 1984.

[30] Hus H., Youssif F., Sen A.and Mitchell J.B.A., *Phys. Rev. A*, **38**, 658, 1988.

[31] Adams N. and Smith D., Dissociative recombination: Theory, Experiment and Application, Singapore: World Scientist **29**,1989

[32] Amano T., *J. Chem. Phys.*, **92**, 6492, 1990.

[33] Canosa A., Rowe B. R., Mitchell J.B.A., Gomet J.C. and Rebrion C., *Astron. Astrophys.*, **248**, L19, 1991.

[34] Smith D. and Španěl P., *Chem. Phys. Letters*, **211**, 454, 1993.

[35] Smith D. and Špatněl P., *Int. J. Mass Spectrom. Ion Process*, **129**, 163, 1993.

[36] Sundström G., Mowat J.R., Danared H., Datz S., Broström L., Filevich A., Källberg A., Mannervik S., Rensfeld K.G., Sigray P., Ugglas M. and Larsson M., *Science*, **263**, 785, 1994

[37] Larsson M., *Int. J. Mass Spectrom. Ion Process*, **149/150**, 403, 1995.

[38] Fehér M., Rohrbacher A. and Maier J., *Chem. Phys*. **185** 357, 1994.

[39] Yousif F. F., Rogelstadt M. & Mitchell J. B. A.,In Atomic and molecular physics: 4th US/Mexico Symp., World Scientific, Singapure, **343**, 1995.

[40] Gougousi T., Johnsen R. and Golde M., *Int. J. Mass Spectrom. Ion Process*, **149/150**, 131, 1995.

[41] Laube S., Le Padellec A., Sidko O., Rebrion-Rowe C., Mitchell J. B. A. and Rowe B. R., *J. Phys. B: At. Molec. Opt. Phys.*, **31**, 2111, 1998

[42] Tanabe T., Chida K., Watanabe T., Arakaki Y., Takagi H., Katayama I., Haruyama Y., Saito M., Nomura I., Honma T., Noda K., Hodin K., Dissociative Recombination: Theory, Experiment and Applications IV, World Scientific: Singapure, 1999.

[43] Schneider T. I. F., Larson M., Orel A. E. and Suzor-Weiner A., Dissociative recombination, Theory, Experiment and Applications IV, **131**, 1999.

[44] Kudrna P., Plasil R., Glosik J., Tichy M., Poteriya V., Rusz J., *Czech. J. Physics*, **50/S3**, 329, 2000.

[45] Glosik J., Plasil R., Poterya V., Kudrna P., Tichy M., *Chem. Phys. Lett.*, **331**, 209, 2000.

[46] Jehnsen M. J., Pederson B. H., Safvan C. P., Seiersen K., Urbain X., Andersen L. H.: *Phys. Rev. A*, **6305**, 2701, 2001.

[47] Plasil R., Glosik J., Poterya V., Kudrna P., Rusz J., Tichy M. and A. Pysanenko: *Int. J. Mass. Spectrom.*, **218**, 105, 2002.

[48] McCall B. J., Huneycutt A. J., Saykally R. J., Geballe T. R., Djuric N., Dunn G. H., Semaniak J., Novotny O., Al-Khalili A., Ehlerding A., Hellberg F., Kalhori S., Neau A., Thomas R., Osterdahl F., Larsson M., *Nature*, **422**, 6931, 500, 2003.

[49] Macko P., Bano G., Hlavenka P., Plasil R., Poterya V., Pysanenko A., Votava O., Johnsen R. and Glosk J., *Int. J. Mass Spectrom.*, **233**, 299, 2004.

[50] Glosik J., Plasil R., Pysanenko A., Novotny O., Hlavenka P., Macko P. and Bano G.: *Journal of Physics: Conference Series 4*, IOP Publishing, Mosbach, Germany, **104**, 2005.

[51] Kreckel H., Motsch M., Mikosch J., Glosik J., Plasil R., Altevogt S., Andrianarijaona V., Buhr H., Hoffmann J., Lammich L., Lestinsky M., Nevo I., Novotny S., Orlov D. A., Pedersen H. B., Sprenger F., Terekhov A. S., Toker J., Wester R., Gerlich D., Schwalm D., Wolf A. and D. Zajfman, *Phys. Rev. Lett.* **95**, 263201, 2005.

[52] Glosik J., Korolov I., Plasil R., Novotny O., Kotrik T., Hlavenka P., Varju J., Mikhaylov I. A., Kokoouline V. and Greene C. H., Recombination of H_3^+ ions in the afterglow of a He–Ar–H_2 plasma, *J. Phys. B: At. Mol. Opt. Phys*. **41,** 2008, 191001

[53] Petrignani, A., Kreckel, H., Berg, M. H., Altevogt, S., Bing, D., Buhr, H., Froese, M., Grieser, M., Hoffmann, J., Jordon-Thaden, B., Krantz, C., Mendes, M. B., Novotny, O., Novotny, S., Orlov, D. A., Reinhardt, S., Wolf, A., Spectroscopy and dissociative recombination of the lowest rotational states of H_3^+. *J. Phys.: Conf. Ser.* **192** (1), 2009, 012022+.

[54] Tom, B. A., Zhaunerchyk, V., Wiczer, M. B., Mills, A. A., Crabtree, K. N., Kaminska, M., Geppert, W. D., Hamberg, M., Ugglas, M. A., Vigren, E., van der Zande, W. J., Larsson, M., Thomas, R. D., McCall, B. J.,. Dissociative recombination of highly enriched para-H_3^+. *J. Chem. Phys.*, **130** (3), 2009, 031101+.

[55] Kreckel, H., Novotný, O., Crabtree, K. N., Buhr, H., Petrignani, A., Tom, B. A., Thomas, R. D., Berg, M. H., Bing, D., Grieser, M., Krantz, C., Lestinsky, M., Mendes, M. B., Nordhorn, C., Repnow, R., Stützel, J., Wolf, A., McCall, B. J., High-resolution storage-ring measurements of the dissociative recombination of H_3^+ using a supersonic expansion ion source. *Phys. Rev. A* **82** (4), 2010, 042715.

[56]Varju J., Hejduk M., Dohnal P., Jílek M., Kotrík T., Plašil R., Gerlich D., Glosík J., Nuclear Spin Effect on Recombination of H_3^+ Ions with Electrons at 77 K. *Phys. Rev. Lett.* **106**, 203201, 2011.

[57] Indriolo, N., Geballe, T. R., Oka, T., McCall, B. J., H_3^+ in Diffuse Interstellar Clouds: A Tracer for the Cosmic-Ray Ionization Rate. *The Astrophysical Journal*, **1736**, 2007.

[58] Larson M. and Orel E. A., *Dissociative Recombination of Molecular Ions*, Cambridge University Press, Cambridge, 2008.

[59] Johnsen R., A critical review of H_3^+ recombination studies, *J. Phys.: Conf. Ser*. **4**, 83, 2005.

[60] Michels, H. H.; Hobbs, R. H., Low-temperature dissociative recombination of E + H_3^+, *Astrophysical Journal, Part 2 - Letters to the Editor* (ISSN 0004-637X), **286**, 1984, p. L27-L29.

[61] Plašil R., Rekombinace molekulárních iontů v dohasínajícím plazmatu, *Ph.D. thesis*, Charles University in Prague, 2003.

[62] Plašil R., Glosík J., Poterya V., Kudrna P., Rusz J., Tichy M. & Pysanenko A., *Int. J. Mass Spectrom*., **218** (2002)(2) 105–130.

[63] Poterya V., Glosik J., Plasil R., Tichy M., Kudrna P. and Pysanenko A., *Phys. Rev. Lett.*, **88**, 4, AR 044802, 2002.

[64] Macko P., Plasil R., Kudrna P., Hlavenka P., Poterya V., Pysanenko A., Bano G. and Glosik J., *Czech. J. Phys. Suppl. D*, **52**, 695, 2002.

[65] Macko P., Bano G., Hlavenka P., Plasil R., Poterya V., Pysanenko A., Votava O., Johnsen R. and Glosk J., *Int. J. Mass Spectrom*., **233**, 299, 2004.

[66] Hlavenka P., The spectroscopic study of cold ions in plasma and ion trap, *Ph.D. thesis*, Charles University in Prague, 2007.

[67] Glosík J., Novotny O., Pysanenko A., Zakouril P., Plasil R., Kudrna P. and Poterya V., *Plasma Sources Sci. Technol.*, **12**, S117, 2003.

[68] Bates D.R., *J. Phys. B: At. Mol. Opt. Phys.* **24**, 1991.

[69] Bates D. R.: *Phys Rev*, **78**, 492, 1950.

[70]Bardsley J. N., *J. Phys. B (Proc. Phys. Soc.)* **1**, 365, 1968.

[71]Bates D. R., *J. Phys. B: At. Mol. Opt. Phys.*, **25** , 5479, 1992.

[72]Schneider I. F., Orel A. E. and Suzor-Weiner A., *Phys. Rev. Lett.* **85**, 3785-3788, 2000.

[73]Kokoouline V., Greene C. H. and Esry B. D., *Nature*, **412**, 891-894, 2001.

[74]Kokoouline V., Greene C. H., *Phys. Rev. A*, **68**, 1, 012703, 2003.

[75] dos Santos S., Kokoouline V. and Greene C. H., *J. Chem. Phys.* **127,** 124309, 2007.

[76] Pagani L., Vastel C., Hugo E., Kokoouline V., Greene C. H., Bacmann A., Bayet E., Ceccarelli C., Peng R. and Schlemmer S., *Astron. Astrophys*. **494** 623, 2009.

[77]Bates D. R. and Khare S., *Proc. Phys. Soc.* **85**, 231, 1965.

[78] Pysanenko A., Studium elektron-intové rekombinace v dohasínajícím vodíkovém plazmatu. *Ph.D. thesis*, Charles University in Prague, 2004.

[79] Neale, L., Miller, S., Tennyson, J., Spectroscopic Properties of the H_3^+ Molecule: A New Calculated Line List., *Astrophys. J.* **464**, 516+, 1996.

[80] Watson, J. K. G.,. Higher-order vibration-rotation energies of the x_3 molecule, *Journal of Molecular Spectroscopy* **103**, 350-363, 1984.

[81] I. R. McNab, *Adv. Chem. Phys.* **89**, 1–87, 1995.

[82] Ramanlal J., The Spectroscopy of H_3^+ : Low Energy to Dissociation, *Ph.D. thesis* , University College London, 2005.

[83] Lindsay, C. M., Mccall, B. J., Comprehensive Evaluation and Compilation of H_3+ Spectroscopy., *Journal of Molecular Spectroscopy* **210**, 60-83. 2001.

[84] Mccall, B. J.,. Laboratory spectroscopy of H_3^+, Astronomy, physics and chemistry of H_3^+. *Phil. Trans. R. Soc. Lond. A* **358**, 2385, 2000.

[85] Herzberg G., Molecular Spectra and Molecular Structure, vol. 1–3, Krieger Pub. Co. Malabar, Florida (1989–1991).

[86] Oka T., *Adv. At. Mol. Phys*. **9,** 127–206, 1973.

[87] Quack M., Detailed symmetry selection rules for reactive collisions, *Mol. Phys.*, **34**, 477, 1977.

[88] Uy D., Cordonnier M. and Oka T., Observation of ortho-para H_3^+ selection rules in plasma chemistry, *Phys. Rev. Lett*. **78**, 3844–3847, 1997.

[89] Cordonnier M., Uy D., Dickson R., Kerr K., Zhang Y. and Oka T., *J. Chem. Phys.* **113**, 3181, 2000.

[90] Oka T., Nuclear spin selection rules in chemical reactions by angular momentum algebra, *J. Mol. Spectrosc.* **228**, 635-639, 2004.

[91] Park K. and Light J. C., *J. Chem. Phys.* **126**, 044305, 2007.

[92] Hugo E., Asvany O., Schlemmer S., *J. Chem. Phys.* **130**, 164302 (2009).

[93] Gerlich D., *J. Chem. Phys*. **92**, 2377, 1990.

[94] Tennyson's homepage (2011), Molecular Physics and Astrophysics Group Homepage, WWW page. http://www.tampa.phys.ucl.ac.uk/ftp/astrodata/h3+/

[95] Rothman L.S., Rinsland C.P., Goldman A., Massie S.T., Edwards D.P., Flaud J.M., Perrin A., Camy-Peyret C., Dana V., Mandin J.Y., Schroeder J., Mccann A., Gamache R.R., Wattson R.B., Yoshino K., Chance K., Jucks K., Brown L.R., Nemtchinov V. & Varanasi P., *Journal of Quantitative Spectroscopy and Radiative Transfer*, **60,** 665–710, 1998.

[96] Anderson, D. Z., Frisch, J. C., Masser, C. S., Mirror reflectometer based on optical cavity decay time., *Appl. Opt.* **23** (8), 1238-1245, 1984.

[97] O'Keefe A., Deacon D. A. G.,. Cavity ring-down optical spectrometer for absorption measurements using pulsed laser sources., *Review of Scientific Instruments* **59** (12), 2544-2551, 1988.

[98] Ye J., Ma L. S., Hall J. L., Ultrasensitive detections in atomic and molecular physics: demonstration in molecular overtone spectroscopy, *J. Opt. Soc. Am B* **15**, 6, 1998.

[99] Thorpe, M. J., Moll, K. D., Jones, R. J., Safdi, B., Ye, J., Broadband Cavity Ringdown Spectroscopy for Sensitive and Rapid Molecular Detection, *Science* **311** (5767), 1595-1599, 2006.

[100] Romanini, D., Kachanov, A. A., Sadeghi, N., Stoeckel, F., CW cavity ring down spectroscopy. *Chemical Physics Letters* **264** (3-4), 316-322, 1997.

[101] Lehmann K.K. & Romanini D., The superposition principle and cavity ring-down spectroscopy, *J. Chem. Phys.* **105** (23) 10263–10277, 1996.

[102] Morville J., Injection des cavités de haute finesse par laser a diode - Application a la CW-CRDS et a la détection de traces atmospheriques,*Ph.D thesis*, L'UNIVERSIT JOSEPH FOURIER, Grenoble 2001

[103] Yariv A., Quantum Electronics, 3rd ed., John Wiley & Sons, New York. 1989.

[104] Jae Won Hahn, Yong Shim Yoo, Jae Yong Lee, Jae Wan Kim, and Hai-Woong Lee, Cavity ringdown spectroscopy with a continuous-wave laser: calculation of coupling efficiency and a new spectrometer design, *Applied optics*, **38**, 9, 1999.

[105] Xu S., Sha G., Xie J., Cavity ring-down spectroscopy in the liquid phase, *Rev. Sci. Instrum.* 73, 255-258, 2002.

[106] DEMTRÖDER, W. . Laser Spectroscopy : Basic Concepts and Instrumentation. 2nd. London : Springer-Verlag, 1996. 924 s. ISBN 978-0387571713.

[107] Morville J., Romanini D., Kachanov A. A., Chevenier, M., Two chemes for trace detection using cavity ringdown spectroscopy, *Appl. Phys. B*, **78**, 465. 2004.

[108] Romanini D., Kachanov A.A. and Stoeckel F., Cavity ringdown spectroscopy: broad band absolute absoprtion measurements, *Chem. Phys. Letters* **270,** 538, 1997.

[109] Hlavenka P., Studium rekombinace iontu H_3^+ při kryogennich podminkach, Diploma thesis,Charles University in Prage 2003.

[110] Fox, P. J., Scholten, R. E., Walkiewicz, M. R., Drullinger, R. E., A reliable, compact, and low-cost Michelson wavemeter for laser wavelength measurement. *American Journal of Physics* **67** (7), 624-630, 1999.

[111] Novotny O., Experimental study of electron-ion recombination using storage ring and afterglow techniques, Ph.D. thesis, Charles University in Prague, 2006

[112] Korolov I., Recombination and reactions of ions at thermal energies, Ph.D. thesis, Charles University in Prague, 2008

[113]Bonhoeffer K. F. and Harteck P., *Z. Phys. Chem. B4*,**113** 1929.

[114]Tam S. and Fajardo M., *Rev. Sci. Instrum.* **70**, 1926 ,1999.

[115] Van Itterbeek A., Verbeke O., Theewes F., Staes K., De Boelpaep J., The difference in vapour pressure between normal and equilibrium hydrogen. Vapour pressure of normal hydrogen between 20 K and 32 K, *Physica*, **30**, 6, 1238-1244.s, 1964.

[116] Tom B. A., Nuclear spin dependence in reactions of H_3^+ in the laboratory and interstellar medium, *Ph.D. thesis*, University of Illinois at Urbana-Champaign, 2009.

[117] Bing D., Kontrollierte Parawasserstofferzeugung zur Untersuchung der Spinsymmetrie bei gespeicherten Wasserstoffmolekulionen, *Diploma thesis*, Ruprecht-Karls-Universitat in Heidelberg, 2006.

[118] Plasil R., Rekombinace molekulárních iontu v dohasinajicim plazmatu, *Ph.D. thesis*, Charles University in Prague 2003

[119] Pysanenko A., Novotny O., Zakouril P., Plasil R., Poterya V. and Glosik J., *Czech. J. Phys D* ., **52**, 681, 2002.

[120] Pysanenko A., Studium rekombinace v dohasinajicim plazmatu, Ph.D. thesis, Charles University in Prague 2004.

[121]Ikezoe Y., Matsuoka S., Takebe M. and Viggiano A., Gas Phase Ion-Molecule Reaction Rate Constants, *The Mass Spectroscopy Society of Japan*, Tokyo (1987)

[122] Deloche R., Monchicourt P., Cheret M. and Lambert F., *Phys. Rev. A.*,**13**, 1140, 1976.

[123] Glosík, J., Bano G., Plasil R., Luca A., Zakouril P., *Int. J. Mass Spectrom*., **189**, 103, 1999.

[124] Dotan I., Lindinger W., *J. Chem. Phys*., **76**, 4972, 1982.

[125] J. Glosík, *International J. of Mass Spectr. and Ion Processes* **139,** 15, 1994.

[126] Villinger H., Futrell J.H., Howorka F., Duric N. and Lindinger W., *J. Chem. Phys*. **76**, 3529, 1982.

[127]Smirnov B. M.: Complex ions. Nauka, Moscow, 1984.

[128] Johnsen R., Huang C.M., Biondi M.A., *J. Chem. Phys.*, **65**, 1539, 1976.

[129]Kokoouline V., Faure A., Tennyson J. and Greene C. H., Calculation of rate constants for vibrational and rotational excitation of the H_3^+ ion by electron impact, *Mon. Not. R. Astron. Soc.* **405**, 1195, 2010.

[130] Petrignani, Annemieke; Altevogt, Simon; Berg, Max H.; Bing, Dennis; Grieser, Manfred; Hoffmann, Jens; Jordon-Thaden, Brandon; Krantz, Claude; Mendes, Mario B.; Novotný, Oldřich; Novotny, Steffen; Orlov, Dmitry A.; Repnow, Roland; Sorg, Tobias; Stützel, Julia; Wolf, Andreas; Buhr, Henrik; Kreckel, Holger; Kokoouline, Viatcheslav; Greene, Chris H. Resonant structure of low-energy H_3^+ dissociative recombination, *Phys. Rev. A* **83**, 032711, 2011.

[131] Dohnal P., Hejduk M., Varju J., Rubovic P., Kotrik T., Plasil R., Glosik J., Recombination of para- and ortho-H_3^+ with electrons at 77-200 K; state selective study, Sent for publication.in *Phys. Rev. A*

[132] Banerjee P. P. and Ting-Chung Poon, *Principles of Applied Optics* , 1991, ISBN 0-256-08860-8